

IMAGING IRREGULARLY SAMPLED 3D PRESTACK DATA

A DISSERTATION
SUBMITTED TO THE DEPARTMENT OF GEOPHYSICS
AND THE COMMITTEE ON GRADUATE STUDIES
OF STANFORD UNIVERSITY
IN PARTIAL FULFILLMENT OF THE REQUIREMENTS
FOR THE DEGREE OF
DOCTOR OF PHILOSOPHY

Nizar Chemingui

June 2001

© Copyright 2001 by Nizar Chemingui
All Rights Reserved

printed as Stanford Exploration Project No. 101
by permission of the author

Copying for all internal purposes of the sponsors
of the Stanford Exploration Project is permitted

I certify that I have read this dissertation and that in my opinion it is fully adequate, in scope and quality, as a dissertation for the degree of Doctor of Philosophy.

Jon F. Claerbout
(Principal Adviser)

I certify that I have read this dissertation and that in my opinion it is fully adequate, in scope and quality, as a dissertation for the degree of Doctor of Philosophy.

Biondo Biondi

I certify that I have read this dissertation and that in my opinion it is fully adequate, in scope and quality, as a dissertation for the degree of Doctor of Philosophy.

Gary Mavko

Approved for the University Committee on Graduate Studies:

*To a legendary father,
Daoud Chemingui*

Abstract

Imaging multichannel seismic data for amplitude inversion is a challenging task. The process seeks an inverse for a matrix of very high order that relates the data to a reflectivity model. Due to the irregular coverage of 3D surveys, the matrix is ill-conditioned and its coefficients are badly scaled. In this dissertation, I present a new approach for imaging irregularly sampled 3D data. The strategy is to reduce the size of the full matrix by reducing the size of 3D prestack data before imaging, and to balance the coefficients of the matrix by regularizing the coverage of 3D surveys. I tackle the case of Kirchhoff imaging operators because of their I/O flexibility and computational efficiency. However, after regularization, full-wave extrapolation techniques may become attractive and practical to implement on the regularly sampled prestack volume.

For adequately sampled 3D data with varying surface coverage, I use an asymptotic approximate inverse to obtain a good image. I apply a new partial prestack operator named azimuth moveout (AMO) to reduce the size of the prestack data and regularize its coverage by partial stacking. The effects of irregular coverage and varying illumination at depth are reduced by applying a diagonal transformation to the Kirchhoff operator.

Problems arise in 3D reflection seismology where fine sampling is not possible and the sparse geometry of 3D surveys results in spatial aliasing. I develop a new dealiasing technique which I refer to as inversion to common offset (ICO). Posing partial stacking as an optimization process, the inversion improves the stack when the data are spatially aliased. I present two formulations for ICO, namely data-space and model-space inversion and design an efficient

implementation of the algorithm in the Log-stretch Fourier domain. To accelerate the convergence of the iterative solution I present a new technique for preconditioning the inversion based on row and column scaling.

Results from field marine and land surveys are presented to demonstrate the application of AMO and ICO for regularizing the coverage of 3D surveys and reducing the costs of 3D prestack imaging. The images obtained by prestack migration after regularization are superior to those obtained by migrating the irregularly sampled data. Furthermore, ICO provides a promising approach for reducing the costs of 3D acquisition.

Preface

All of the figures in this thesis are marked with one of the three labels: [ER], [CR], and [NR]. These labels define to what degree the figure is reproducible from the data directory, source code and parameter files provided on the web version of this thesis ¹.

ER denotes Easily Reproducible. The author claims that you can reproduce such a figure from the programs, parameters, and data included in the electronic document. We assume you have a UNIX workstation with Fortran77, Fortran90, C, X-Window system, and the software on the SEP freely distributed software at your disposal. Before the publication of the electronic document, someone other than the author tests the author's claim by destroying and rebuilding all ER figures.

CR denotes Conditional Reproducibility. The author certifies that the commands are in place to reproduce the figure if certain resources are available. To find out what the required resources are, you can inspect a corresponding warning file in the document's result directory. For example, you might need a large or proprietary data set. You may also need a super computer, or you might simply need a large amount of time (30 minutes or more) on a workstation.

NR denotes Non-Reproducible. This class of figure is considered non-reproducible. Figures in this class are scans and artists' drawings. Output of interactive processing are labeled NR.

¹<http://sepwww.stanford.edu/public/docs/sep101>

Figures marked as [CR] in Chapter 2 can not be reproduced easily because of the proprietary dataset provided by Elf-Aquitaine and used for the simulations. Those figures also require many hours of computing time on a parallel super-computer.

Conditionally reproducible figures from Chapter 3 are solely limited by the necessary computer time.

All [CR] figures in Chapters 4 and 5 are limited in their reproducibility by the required computer time. I have included the original 3D subsets in the data directory, so the figures are can be reproduced if you are willing to wait several hours or days.

Acknowledgements

It is a great pleasure for me to express my sincere gratitude to the faculty, students and sponsors of the Stanford Exploration Project. I am immensely privileged to have had the supervision of Jon Claerbout and direct guidance of Biondo Biondi. Jon Claerbout provided an outstanding research environment where academic freedom and efficient organization are uniquely combined. Biondo Biondi got me started on AMO at my early stage at SEP and guided my research throughout my stay at Stanford. My fellow students offered their camaraderie and daily consultations on practical and theoretical problems. Diane Lau was a special friend who is always available to help beyond the call of duty. James Rickett and Per Avseth were the best company for the study breaks. A special thanks goes to Diane, James and Per for handling the manuscript of my dissertation after I left Stanford.

I am very privileged to have learned geophysics at three outstanding institutions; The Colorado school of Mines, Rice, and Stanford universities. Many professors contributed to make my learning a unique and pleasant experience. The ones that had influenced my journey the most are Alexander Kaufman, Norm Bleistein, Jack Cohen, John DeSanto, Ken Lerner, Tom Boyd, Alan Levander, Gerry Gardner and Bill Symes. A special thank you goes to Norm Bleistein who first introduced me to the topic of inverse problems and got me interested in its geophysical applications.

I like to thank Elf-Aquitaine and in particular Henry Calandra for providing the North Sea dataset, also PanCanadian and in particular Bill Goodway for offering the Shorncliff dataset.

I am very grateful to my wife Ferial for her love and support that gave me the strength to complete this work. She never gave up and stood by my side to the very end. Ferial, I love

you and thank you for all the long nights and weekends you spent alone while I had to be in the office.

Finally, I like to express my sincere gratitude to my parents for their endless love and encouragement. I dedicate this work to the soul of my father. Without his guidance and wisdom I would not be where I am today. Dad, all those great advises you gave me paid off, I love you very much, you are the greatest.

Contents

Abstract	vii
Preface	ix
Acknowledgements	xi
1 Introduction	1
2 The Azimuth Moveout Operator (AMO)	9
3 Amplitude-preserving AMO	27
4 True-amplitude Kirchhoff imaging	39
5 Inversion to common offset	61
A Derivation of integral AMO	83
Bibliography	92

List of Figures

2.1	The full AMO impulse response ($V_{min} \simeq 0$) when $t_1 = 1$ s, $h_1 = 2$ km, $h_2 = 1.8$ km, $\theta_1 = 0^\circ$, $\theta_2 = 30^\circ$	11
2.2	The maximum spatial support of the AMO operator (shaded parallelogram) in the midpoint plane $(\Delta m_x, \Delta m_y)$, as a function of the input offset \mathbf{h}_1 , and the output offset \mathbf{h}_2	13
2.3	The effective AMO impulse response when $V_{min} = 2$ km/s, and $t_1 = 1$ s, $h_1 = 2$ km, $h_2 = 1.8$ km, $\theta_1 = 0^\circ$, $\theta_2 = 30^\circ$, as in Figure 1.	13
2.4	The geometric relationship between the unit vectors ξ_1 and ξ_2 of the transformed midpoint-coordinate axes, and the input offset \mathbf{h}_1 and the output offset \mathbf{h}_2	15
2.5	Depth velocity model of the survey area.	18
2.6	Geological in-line section and corresponding velocities of layers.	18
2.7	NMO-Stack of North Sea data set used for testing AMO.	21
2.8	Offset-azimuth distribution of the 1,000-1,400 m offset range.	22
2.9	In-line sections (4,150 m) for the 1,000 – 1,400 m offset range, obtained by a) NMO-stacking, b) NMO-AMO-stacking, c) subtracting a) from b).	23
2.10	Window on the In-line sections (4,150 m) obtained by a) NMO-stacking, b) NMO-AMO-stacking, c) subtracting a) from b).	24

2.11	Time slices (1.36 s) for the 1000 – 1,400 m offset range, obtained by a) NMO-stacking, b) NMO-AMO-stacking, c) subtracting a) from b).	25
2.12	Window on the time slices (1.36 s) obtained by a) NMO-stacking, b) NMO-AMO-stacking, c) subtracting a) from b).	26
3.1	From left to right: input data, cascade of several DMO operators with their inverse.	33
3.2	Peak amplitudes along a dipping event from the cascade of several DMO operators and their inverse. The solid curve is the result of the adjoint inverse. The results of the asymptotic inverse for Hale, Zhang, and Bleistein operators coincide with original input amplitudes	34
3.3	Peak amplitudes along a dipping event from a zero-offset section obtained by different DMO operators. The continuous curve is the the predicted result, the dashed curve is Hale’s result, the dotted curve is Black/Zhang’s output and the large dashed curve (top curve) is Bleistein’s output	35
3.4	Amplitude preservation by AMO: the dashed curve are the peak amplitudes from the AMO result. The solid curve represents the predicted amplitudes by Kirchhoff modeling. (a) azimuth rotation by 45 degrees; (b) offset continuation by 800 meters; (c) azimuth rotation and offset continuation.	38
4.1	Processing flow chart proposed for amplitude-preserving processing of wide-azimuth surveys	44
4.2	NMO-stack of the full over-sampled full survey.	46
4.3	Azimuth and offset distribution of the cross-spread survey.	48
4.4	Cross-spread acquisition geometry with grid spacing of 210 m. The stars and circles indicate the source and receiver locations respectively.	48
4.5	Fold diagram for the 3-D subset from the decimated survey.	49

4.6	Fold diagram for the 3-D subset from the over-sampled survey	49
4.7	AMO fold at 0.71 seconds	51
4.8	Migration fold at 920 m depth	51
4.9	AMO impulse response at different time levels for 150m offset continuation and 25 degrees rotation.	52
4.10	Migration impulse response at depth levels corresponding to the time levels on the figure above.	52
4.11	Normalizing by the AMO fold: a) un-normalized AMO, b) normalized AMO, c) difference between a) and b)	53
4.12	Normalizing by the AMO fold to a power of 0.5: a) un-normalized AMO, b) normalized AMO, c) difference between a) and b)	54
4.13	In-line section at 1.km; a) unnormalized AMO, b) normalized AMO	55
4.14	Cross-line section at 1.km; a) unnormalized AMO, b) normalized AMO	55
4.15	One-dimensional RMS and interval velocity functions of the survey	58
4.16	Depth slices at 920 m obtained by different imaging flows a) Migration of oversampled subset, b) migration after AMO, c) migration of irregular subset, d) migration after binning	59
4.17	Depth slices at 910 m obtained by different imaging flows a) Migration of oversampled subset, b) migration after AMO, c) migration of irregular subset, d) migration after binning	60
5.1	Convergence of the model-space solution for one frequency inversion using different preconditioners.	71
5.2	Source receiver layout for a decimated survey with cross-spread spacing of 350 m. The stars and circles indicate the source and receiver locations respec- tively.	73

5.3	Fold distribution of the oversampled survey for the 3D subset	73
5.4	Fold distribution for the decimated subset binned at the nominal CMP spacing.	74
5.5	Fold distribution for the decimated subset binned at the model resolution. . .	74
5.6	Time slices (0.71 s) obtained by: a) NMO-Stack of over-sampled subset, b) NMO-Stack of decimated subset, c) Un-normlized AMO-Stack, d) Normalized AMO-Stack, e) ICO partial stack using the data-space inverse, f) ICO partial stack using the model-space inverse.	78
5.7	In-line sections at 1 km obtained by: a) NMO-Stack of over-sampled subset, b) NMO-Stack of decimated subset, c) Un-normlized AMO-Stack, d) Normalized AMO-Stack, e) ICO partial stack using the data-space inverse, f) ICO partial stack using the model-space inverse.	79
5.8	Cross-line sections at 1 km obtained by: a) NMO-Stack of over-sampled subset, b) NMO-Stack of decimated subset, c) Un-normlized AMO-Stack, d) Normalized AMO-Stack, e) ICO partial stack using the data-space inverse, f) ICO partial stack using the model-space inverse.	80
5.9	Depth slices at 920 m obtained by different imaging flows a) Migration of oversampled subset, b) Migration of decimated subset, c) Migration after binning, d) Migration after normalized AMO, e) Migration after ICO using data-space inverse, f) Migration after ICO using model-space inverse	81
5.10	Depth slices at 910 m obtained by different imaging flows a) Migration of oversampled subset, b) Migration of decimated subset, c) Migration after binning, d) Migration after normalized AMO, e) Migration after ICO using data-space inverse, f) Migration after ICO using model-space inverse	82

Chapter 1

Introduction

OVERVIEW

The growing need for detailed reservoir descriptions has led to the careful handling of amplitudes from 3D reflection data. Seismic reflections are characterized by their arrival times and amplitudes. Though both are functions of the medium velocity, they are observed over different spectral windows of good quality reflection data. Amplitudes are interpreted through reflectivities which describe the high frequency part of the “real velocity” in the subsurface. Therefore, the processing of seismic data for amplitude inversion has found many applications in fluid imaging, reservoir monitoring, AVO analysis, anisotropy detection, and other related applications.

However, acquiring, processing and interpreting seismic data for true amplitude is a complex process. The difficulties arise from the definition itself of “true amplitude”, and the sensitivity of the process to acquisition geometry, processing algorithms, and interpretation goals. Over the past decade, “true-amplitude” processing has emerged as a new field of research and re-evaluation of conventional techniques. Most amplitude studies have focused on the development of amplitude-preserving operators such as DMO (Beasley and Mobley, 1988; Black et al., 1993a) and migration (Bleistein, 1987; Sullivan and Cohen, 1987; Schleicher et al., 1993). The algorithms are derived so that amplitude variations as a function of offset are

not distorted by the process. However, focusing solely on algorithmic accuracy ignores an issue often more detrimental to amplitude preservation: the effect of sparse and irregular sampling (Beasley and Klotz, 1992; Canning and Gardner, 1995). Many important and sometimes conflicting issues influence 3D survey design; we need to be concerned about adequate midpoint sampling, sufficient offset distribution and high fold for best quality images. Recently, the issue of azimuth also became an important consideration in the design of 3D surveys and led to the controversial question of whether to collect data with a wide or narrow range of azimuths. Wide-azimuth surveys are often considered challenging; the challenge is not the azimuth range itself, but the way in which wide azimuth surveys are acquired. Most often each azimuth is not sufficiently sampled in offsets and midpoints. In reality, there is no unique answer to the question of azimuth; at best, there are only factors that need to be considered and balanced against others during the design of each survey for optimum balance of cost and quality. With current recording geometries, it is difficult to sample the five-dimensional wavefield completely. In addition, during the acquisition stage, obstructions, cable feathering, environmental objectives, economic constraints and many other factors cause seismic data to be sampled in sparse and irregular fashion. The irregularities are observed in the form of variations in the fold coverage, which can manifest itself as an acquisition footprint on prestack data or even the stacked image. If not accounted for, irregular sampling can affect data analysis, and introduce noise, amplitude distortions and even structural distortions in the final image. (Black and Schleicher, 1989; Gardner and Canning, 1994; Beasley, 1994).

Many techniques with varying cost and accuracy have been proposed for processing irregularly-sampled data; among them equalized DMO (Beasley and Klotz, 1992), geometrically calibrated DMO (Ronen et al., 1995) and spatial dealiasing (Ronen and Liner, 1987). The goal is to avoid aliasing by interpolating missing data and to equalize the imaging process for the effects of fold variations. In this context, the term fold refers to the variation of coverage at the recording surface. In areas of complex structure, velocity variations significantly distort seismic wave propagation and result in variation of coverage at target zones. The depth varying coverage is referred to as illumination. Generally, it is expected that depth migration in complex structures produces an optimally stacked image positioned at the correct depth. Given the size of modern 3D surveys, the process is computationally challenging. It also fails quite often because of the difficulty of determining the velocity field, the irregular sampling of seismic

data, and, in many cases, the lack of illumination of target zones beneath complex structures.

Therefore, assessing the quality of survey designs, reducing the size of the prestack data volume, and regularizing its coverage are essential requirements for practical and efficient prestack imaging of 3D data.

In the dissertation, I present a new approach for imaging irregularly sampled 3D prestack data that uniquely addresses the issues of economic efficiency, accuracy of algorithms, and proper handling of irregular geometry. The strategy is to regularize the coverage of 3D surveys and reduce the size of 3D prestack data by partial stacking. Both objectives make use of a new partial prestack imaging operator, azimuth-moveout (AMO), first introduced by Biondi and Chemingui (1994). For adequately sampled 3D data, I propose a new imaging sequence that applies AMO to regularize the data into common-azimuth common offset cubes before imaging. For spatially aliased data, I pose partial stacking as an optimization process to improve the quality of partial stacks and regularize the geometry of the data before imaging.

The second Chapter of the dissertation introduces the AMO operator and discusses its application for partial stacking to reduce the cost of 3D imaging. It illustrates an example of applying AMO to reduce the size of a real 3D marine survey from the North Sea. In the third Chapter, I show how we can derive an amplitude-preserving function for AMO so that the offset and azimuth information are preserved by the transformation. The fourth Chapter focuses on Kirchhoff theory and the application of AMO as an integral operator to regularize 3D geometries for common-azimuth processing. In the last Chapter of the dissertation, I introduce a new wave-equation inversion technique that is suitable for data with irregular geometry and takes advantage of the abundance of seismic data in multichannel recording to interpolate beyond aliasing. I demonstrate the application of the inversion to regularize the coverage of 3D surveys and reduce the cost of 3D acquisition in general.

WHAT IS AMO?

The AMO operator introduced in this dissertation is a new partial prestack imaging operator that can be efficiently applied to 3-D prestack data to transform their effective offset and azimuth. By including AMO in the processing flow, we can reduce the computational costs of 3D imaging and, in many applications, improve the quality of the final image. I demonstrate in Chapter 2 how the size of 3D prestack dataset can be largely reduced by coherent partial stacking using AMO, which preserves the high-frequency, steeply-dipping energy. AMO is also a modeling operator that maps seismic data into equivalent data with different offset and azimuth. Therefore, it can be effectively employed for data regularization and for wave-equation interpolation to overcome spatial aliasing. These two applications are fully explored in Chapters 3 and 4.

Biondi and Chemingui (1994) defined AMO as the cascade of a 3D prestack imaging operator with its corresponding modeling operator. To derive analytical expressions for the AMO impulse response, we used both constant velocity DMO and its inverse, as well as constant-velocity migration and modeling. The two derivations yield to an equivalent, velocity-independent definition for the kinematics of AMO. Similar to DMO processing (Deregowski and Rocca, 1981; Hale, 1984), the first order effects of velocity variation are removed by applying a normal moveout correction (NMO) to the data prior to AMO. Given the irregular spatial sampling of 3D data, AMO is implemented as an integral operator. Its impulse response is a skewed saddle in the time-midpoint space. The shape of the saddle depends on the amount of azimuth rotation and offset continuation applied to the data. For small azimuthal rotations and offset continuation, the AMO impulse response is compact and its application as an integral operator is inexpensive compared to 3D prestack migration.

In the context of amplitude preserving processing, I developed a true amplitude function for AMO so that amplitude variations as a function of offset and azimuth are not distorted by the transformation. I restricted the definition of “true-amplitude” to be consistent with the definition of most interpreters for preserving peak amplitudes of reflection events. The derivation is based on chaining a “true-amplitude” DMO with its amplitude preserving “true”-inverse. I use a general formulation for inverting integral solutions, (Beylkin, 1985; Cohen

and Hagin, 1985) to derive an integral inverse DMO that is asymptotically valid. Detailed derivation of AMO amplitudes are provided in Chapter 3 which illustrates an example of a “true-amplitude” algorithm.

AMPLITUDE PRESERVING IMAGING

Correct analysis of amplitude information requires prestack imaging to determine the location and extent of reflectivity anomalies. Kirchhoff techniques have been widely used for imaging 3D data because of their I/O flexibility and computational efficiency. They evade the question of total cost by being target oriented. The mathematical derivations of integral operators assume continuous wavefields. In generating the seismic model, each trace is modeled as a weighted sum of image sources on a reflector. Therefore, Kirchhoff imaging of seismic data involves a weighted sum of filtered surface-recorded traces where the weights are deduced from the theory of asymptotic inversion. In practice, the resulting imaging algorithms are applied to discretely sampled seismic data and their implementation reduces to a matrix-vector multiplication. Due to irregular coverage, the matrix is often ill-conditioned, and the linear system that need to be solved is badly scaled.

In Chapter 4, I present a new processing sequence for irregularly sampled 3D prestack data. The method focuses on both algorithmic accuracy and proper handling of irregular geometry. Therefore it allows for reliable AVO analysis on migrated data. It employs the AMO operator to organize the data into regularly gridded common-azimuth (CA) and common-offset (CO) subsets. The regular CA/CO cubes are then ready for imaging by efficient migration algorithms.

To correct for the irregular surface coverage and the varying subsurface illumination, I propose two new developments for Kirchhoff operators: a data-space formulation based on row scaling of pull (sum) operators, and a model-space normalization based on column scaling of push (spray) operators. In both approaches, the final image is normalized by a reference model that is the operator’s response to an input vector with all components equal to one. A more general approach is to properly scale both row and columns of the operator. As will be shown in Chapter 5, this weighting is suitable for the preconditioning of Kirchhoff matrices

for iterative linear solvers.

Results from applying the new processing flow to a 3D land survey showed that using AMO to regularize the coverage of the data by partial stacking improves the quality of the final image. The normalization technique has proved to equalize the AMO operator for the effects of the varying illumination. The advantage of applying the AMO transformation before migration is threefold: (1) reduction of the size of prestack data subsets (2) interpolation to a regular grid before imaging (3) common-azimuth common-offset processing of 3D surveys.

INVERSION TO COMMON OFFSET

The offset dimension adds important aspects to reflection seismology. Mainly, it provides robust analysis of the velocity of seismic waves and enables enhancement of signal-to-noise ratio by stacking. During conventional NMO-stacking, traces obtained from independent measurements are treated as redundant and therefore summed together to reduce random noise by destructive interference. In Chapter 5 of the dissertation, I use the offset dimension to formulate an inversion technique that is suitable for data with irregular geometry and takes advantage of the abundance of seismic traces in multichannel recording to interpolate beyond aliasing. Posing partial stacking as an optimization process, the inversion improves the stack when the data are spatially aliased. Furthermore, the solution provides an opportunity for potentially reducing the cost of 3D surveys by acquiring data with sparse offset sampling. Since the modeling operator that relates the data to the reflectivity model is AMO, the inversion is not restricted to zero-offset models or to a particular azimuth. The model, in general, simulates a regular common-offset experiment.

The inversion of multichannel seismic data is generally perceived as an overdetermined problem. In reality, the problem is often locally underdetermined due to inadequate sampling of 3D subsets and gaps in seismic coverage that result into missing data. Moreover an ill-conditioned system of equations behaves numerically as underdetermined. Therefore, based on the least-squares solutions for overdetermined and underdetermined systems, I discuss two formulations for the inversion which I refer to as data-space and model-space inverses. The data-space solution represents a two-step reflectivity inversion where the data is equalized in a

first stage with an inverse AMO filter and an imaging operator is then applied to the equalized data to invert for a model. The model-space solution poses the inverse of AMO stacking as a modeling process and iteratively solves for a regularly sampled partial stack from the irregularly sampled data.

The application of a time-variant operator as an optimization process is not practical for 3D data because of its computing costs. I present a cost-effective implementation of the inversion based on a log-stretch transformation (Bolondi et al., 1982; Ronen, 1987), after which AMO becomes time invariant and the inversion can be split into independent frequencies. To accelerate the convergence of the iterative solution, I propose a new technique for preconditioning based on proper scaling of both rows and columns of the operator. Finally, to regularize the inversion, one needs to limit the variability of the model and guide the iterative optimization to the desired solution. The trick is to augment the problem with a model penalty operator that adds constraints about the model smoothness.

Results of applying the inversion technique to a 3D land survey showed that we can decimate the prestack data to simulate sparse acquisition geometries while still able to reconstruct the high frequency features of the reflectivity function (i.e., buried channels). The cost of the iterative solution is reasonable because of the limited aperture of the modeling operator (AMO), the practical Log-stretch Fourier domain implementation, and the suitable preconditioning of the linear system. The costs incurred by the iterative solution are quite negligible in comparison to potential savings in acquisition costs.

Chapter 2

The Azimuth Moveout Operator (AMO)

OVERVIEW

In this chapter I present the azimuth moveout operator, (AMO), first introduced by Biondi and Chemingui (1994). AMO is a new partial prestack imaging operator that rotates the azimuth and modifies the offset of 3-D prestack data. AMO has a wide range of applications in 3D prestack imaging. Two promising applications discussed in this chapter are the reduction of the size of prestack data by partial stacking and the transformation of marine surveys to effective common azimuth geometry. Common-azimuth data can then be efficiently depth migrated by new 3D prestack migration methods (Canning and Gardner, 1996; Biondi and Palacharla, 1996).

The first section of this chapter discusses the derivation of the AMO operator and analyzes the characteristics of its impulse response. The second section addresses the theoretical and practical issues for an efficient implementation of AMO as an integral operator. Finally, the third section of the chapter illustrates the application of AMO for partial stacking of a real 3D survey from the North Sea. Appendix A presents detailed derivations of the main analytical results shown in this chapter.

DERIVATION OF AMO

AMO is derived by chaining a 3D prestack imaging operator with its corresponding 3D prestack modeling operator. In principle, any 3D prestack imaging operator can be used for the definition of AMO. However, the characteristics of the resulting AMO operator, mainly computational efficiency and degree of required knowledge of the velocity model, depend on the 3D prestack operator used for its definition. An accurate AMO operator can be derived from 3D prestack migration; however, that would require a detailed knowledge of the velocity function, and it would be very difficult to derive its analytical representation, which could lead to a potentially expensive implementation. Recently, Goldin (1994) and Hubral et al. (1996) presented a general methodology for cascading 3D imaging operators. The implementation of their theory, however, requires expensive numerical evaluation of the cascaded operator.

Originally, we defined AMO from the cascade of dip moveout (DMO) and inverse DMO (Biondi and Chemingui, 1994). To derive an accurate expression for the spatial aperture of AMO, we used full 3D prestack constant velocity migration (Biondi et al., 1998). The two derivations yield to an equivalent, velocity-independent, definition for the kinematics of AMO. Similar to DMO processing (Deregowski and Rocca, 1981; Hale, 1984), the first-order effects of velocity variation are removed by applying a normal moveout correction (NMO) to the data prior to AMO.

As a partial imaging operator, AMO moves events across midpoints according to their dip. It therefore preserves all the dips in the data during partial stacking. The transformation is thoroughly defined in the midpoint-offset domain by the kinematics, the amplitude weights and the spatial extent (aperture) of the AMO impulse response.

AMO impulse response

The impulse response of AMO is described by a saddle in the output midpoint domain. The shape of the saddle depends on the offset vector of the input data $\mathbf{h}_1 = h_1 \cos \theta_1 \mathbf{x} + h_1 \sin \theta_1 \mathbf{y} = h_1(\cos \theta_1, \sin \theta_1)$ and on the output offset vector $\mathbf{h}_2 = h_2(\cos \theta_2, \sin \theta_2)$, where the unit vectors \mathbf{x} and \mathbf{y} point respectively in the in-line direction and the cross-line direction. The analytical

expression of the AMO saddle, as given in Appendix A, is,

$$t_2(\Delta \mathbf{m}, \mathbf{h}_1, \mathbf{h}_2, t_1) = t_1 \frac{h_2}{h_1} \sqrt{\frac{h_1^2 \sin^2(\theta_1 - \theta_2) - \Delta m^2 \sin^2(\theta_2 - \Delta \varphi)}{h_2^2 \sin^2(\theta_1 - \theta_2) - \Delta m^2 \sin^2(\theta_1 - \Delta \varphi)}}. \quad (2.1)$$

The traveltimes t_1 and t_2 are the traveltime of the input data after normal moveout correction and the traveltime of the results before inverse NMO. The midpoint vector $\Delta \mathbf{m} = \Delta m(\cos \Delta \varphi, \sin \Delta \varphi)$ is the difference between the input and output midpoint location vectors.

The surface represented by equation (2.1) is a skewed saddle; its shape is controlled by the values of the absolute offsets h_1 and h_2 , and by the azimuth rotation $\Delta \theta = \theta_1 - \theta_2$. The spatial extent of the operator has a maximum for rotation of 90 degrees and vanishes when offsets and azimuth rotation tend to zero. Figure 2.1 shows the surface of the AMO impulse response when t_1 is equal to 1 s, h_1 is equal to 2 km, h_2 is equal to 1.8 km, θ_1 is equal to zero degrees, and θ_2 is equal to 30 degrees.

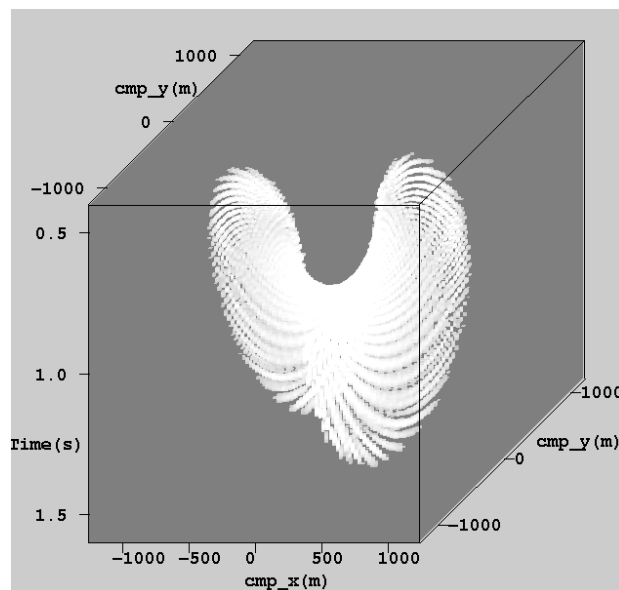


Figure 2.1: The full AMO impulse response ($V_{min} \simeq 0$) when $t_1 = 1$ s, $h_1 = 2$ km, $h_2 = 1.8$ km, $\theta_1 = 0^\circ$, $\theta_2 = 30^\circ$. `amo-impulse-big` [NR]

AMO aperture

Although the expression for the kinematics of AMO is velocity independent, the aperture of the operator depends strongly on velocity. The domain of influence of the AMO operator is defined by the region of validity of expression (2.1), which becomes singular when either of the following conditions is fulfilled:

$$\begin{aligned} \frac{|\Delta \mathbf{m} \times \mathbf{h}_1|}{|\mathbf{h}_1 \times \mathbf{h}_2|} &= 1 \\ \frac{|\Delta \mathbf{m} \times \mathbf{h}_2|}{|\mathbf{h}_1 \times \mathbf{h}_2|} &= 1. \end{aligned} \quad (2.2)$$

Geometrically, this means that the support of the AMO operator at the recording surface is limited to the region within the parallelogram with s main diagonal $(\mathbf{h}_1 + \mathbf{h}_2)$ and minor diagonal $(\mathbf{h}_1 - \mathbf{h}_2)$. The shaded area in Figure 2.2 shows a sample parallelogram that represents the maximum possible spatial extent of the AMO operator. More stringent bounds for the AMO aperture were presented by Biondi et. al. (1998). For given \mathbf{h}_1 and \mathbf{h}_2 , these bounds are a function of the input traveltime and the minimum velocity V_{min} . The parallelogram in Figure 2.2 therefore represents the extreme case where either the velocity or the input traveltime is equal to zero. Figure 2.3 shows the effective AMO impulse response for a limited aperture corresponding to a realistic minimum velocity of 2 km/s. Figure 2.3 is significantly narrower than the whole impulse response shown in Figure 2.1. This velocity-dependent aperture limitation is important for an efficient use of AMO and makes the cost of applying AMO to the data negligible compared to the cost of full 3-D prestack migration.

The effective aperture becomes tiny when the azimuth rotation $\Delta\theta$ is small. At the limit, the expression in equation (2.1) is singular when the azimuth rotation vanishes and the AMO surface reduces to a 2-D line. This operator, corresponding to the case of *offset continuation* (Bolondi et al., 1984), has been derived independently by Biondi and Chemingui (1994), Stovas and Fomel (1996), and (in a different form) Bagaini et al. (1994). Its expression is given by the following quadric equation,

$$t_2(\Delta m, h_1, h_2, t_1) =$$

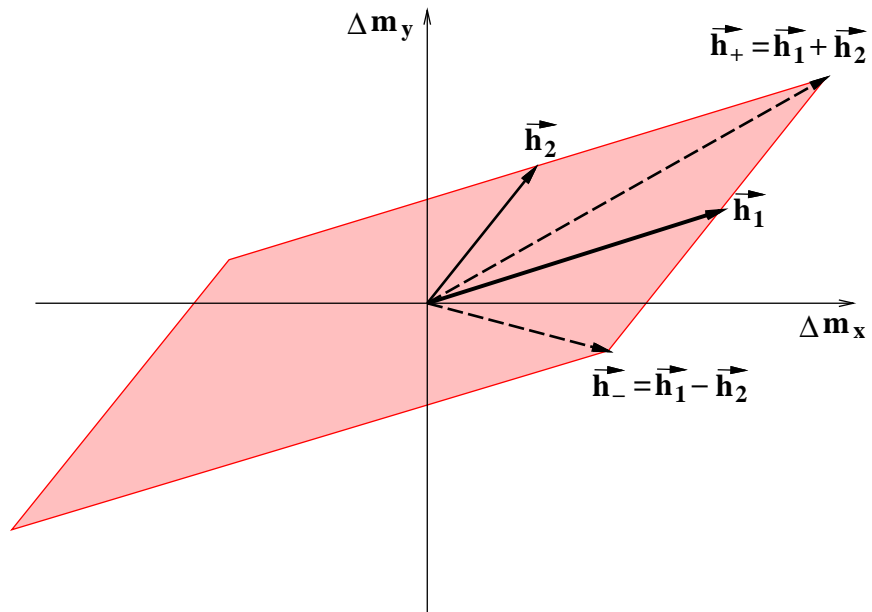


Figure 2.2: The maximum spatial support of the AMO operator (shaded parallelogram) in the midpoint plane $(\Delta m_x, \Delta m_y)$, as a function of the input offset \mathbf{h}_1 , and the output offset \mathbf{h}_2 . `amo-amoapert` [NR]

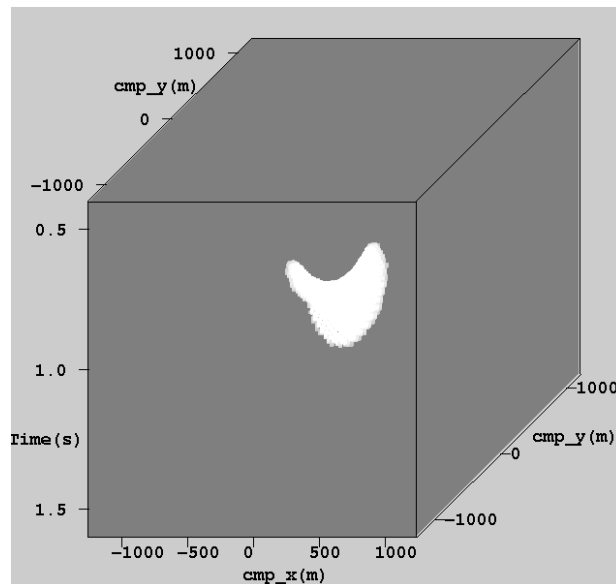


Figure 2.3: The effective AMO impulse response when $V_{min} = 2$ km/s, and $t_1 = 1$ s, $h_1 = 2$ km, $h_2 = 1.8$ km, $\theta_1 = 0^\circ$, $\theta_2 = 30^\circ$, as in Figure 1. `amo-impulse-small` [NR]

$$\begin{aligned}
t_1 \frac{\sqrt{2}h_1}{\sqrt{(h_1^2+h_2^2)-\Delta m^2+\sqrt{[(h_1-h_2)^2-\Delta m^2][(h_1+h_2)^2-\Delta m^2]}}} & \quad h_2 \geq h_1 \\
t_1 \frac{\sqrt{(h_1^2+h_2^2)-\Delta m^2+\sqrt{[(h_1-h_2)^2-\Delta m^2][(h_1+h_2)^2-\Delta m^2]}}}{\sqrt{2}h_2} & \quad h_2 \leq h_1.
\end{aligned} \tag{2.3}$$

Taking into account the effective aperture of the AMO operator, it can be shown (Fomel and Biondi, 1995a) that the 3-D operator monotonously shrinks to a line, and the limit of the kinematics of the 3-D operator [equation (2.1)] approaches the 2-D operator [equation (2.3)].

AMO amplitudes

While the kinematics of AMO are independent of its derivation, the amplitude term varies according to the derivation. In the next chapter I present detailed derivations for a true-amplitude function for the AMO operator. In short, the weights are based on the cascade of an amplitude preserving DMO with its asymptotic “true-inverse” (Chemingui and Biondi, 1995). The choice of Zhang-Black’s Jacobian yields the following expression for the amplitude term:

$$\begin{aligned}
A(\Delta \mathbf{m}, \mathbf{h}_1, \mathbf{h}_2, t_2) \approx & \\
\frac{|\omega_2| t_2}{2\pi h_1 h_2 \sin \Delta\theta} \frac{1 + \frac{\Delta m^2 \sin^2(\theta_2 - \Delta\varphi)}{h_1^2 \sin^2 \Delta\theta}}{\left(1 - \frac{\Delta m^2 \sin^2(\theta_2 - \Delta\varphi)}{h_1^2 \sin^2 \Delta\theta}\right) \left(1 - \frac{\Delta m^2 \sin^2(\theta_1 - \Delta\varphi)}{h_2^2 \sin^2 \Delta\theta}\right)}. & \tag{2.4}
\end{aligned}$$

The frequency term $|\omega_2|$ enters as multiplicative factor in the expression for AMO amplitudes. This term can be applied to the output data in the time domain by cascading a causal half-differentiator with an anti-causal half-differentiator.

INTEGRAL IMPLEMENTATION OF AMO

This section discusses practical issues for a cost-effective implementation of AMO as an integral operator in the time-space domain. The main challenge is to take advantage of the limited aperture for the integration to save computational costs while avoiding operator aliasing. For small azimuthal rotations, the saddle describing the AMO impulse response has a

strong curvature that requires special handling of operator antialiasing. The trick is to perform the spatial integration in a transformed coordinate system where the AMO surface becomes invariant with respect to the amount of azimuth rotation and offset continuation. The appropriate midpoint-coordinate transformation is described by the following chain of transformations (Fomel and Biondi, 1995b):

$$\begin{bmatrix} \xi_1 \\ \xi_2 \end{bmatrix} = \begin{bmatrix} \frac{1}{h_2 \sin \Delta\theta} & 0 \\ 0 & \frac{1}{h_1 \sin \Delta\theta} \end{bmatrix} \begin{bmatrix} -\sin\theta_1 & \cos\theta_1 \\ -\sin\theta_2 & \cos\theta_2 \end{bmatrix} \begin{bmatrix} \Delta m_x \\ \Delta m_y \end{bmatrix}, \quad (2.5)$$

where ξ_1 , and ξ_2 are the transformed midpoint coordinates. Figure 2.4 shows a schematic of the relationship between the input and output offset vectors \mathbf{h}_1 and \mathbf{h}_2 , and the transformed midpoint-coordinate unit vectors ξ_1 and ξ_2 . The right matrix represents a space-invariant rotational squeezing of the coordinate, while the left matrix is a simple rescaling of the axes by a factor dependent on the azimuth rotation $\Delta\theta$ and the length of the offset vectors.

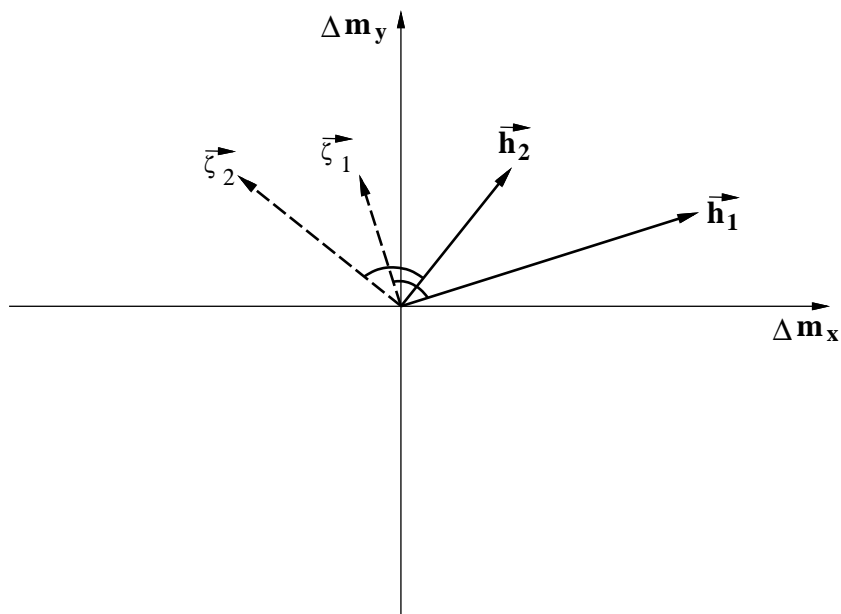


Figure 2.4: The geometric relationship between the unit vectors ξ_1 and ξ_2 of the transformed midpoint-coordinate axes, and the input offset \mathbf{h}_1 and the output offset \mathbf{h}_2 . amo-amonewcoord [NR]

In this new coordinate system, the kinematics of AMO are described by the following

simple relationship between the input time t_1 and the output time t_2

$$t_2(\xi_1, \xi_2) = t_1 \sqrt{\frac{1 - \xi_2^2}{1 - \xi_1^2}}, \quad (2.6)$$

and the amplitudes (based on Zhang-Black amplitudes for DMO) are described by the following equation

$$A(\xi_1, \xi_2) = \frac{t_2 |\omega_2|}{2\pi} \frac{(1 + \xi_1^2)}{(1 - \xi_1^2)(1 - \xi_2^2)}. \quad (2.7)$$

which takes into account the Jacobian factor introduced by the coordinate transformation.

To avoid operator aliasing, one should apply a low-pass filter whose bandwidth varies spatially along the operator and is a function of the local time dips of the operator. The time dips can be computed analytically according to the following equations:

$$\frac{\partial t_2}{\partial \xi_1} = t_2 \frac{\xi_1}{1 - \xi_1^2}, \quad (2.8)$$

$$\frac{\partial t_2}{\partial \xi_2} = -t_2 \frac{\xi_2}{1 - \xi_2^2}. \quad (2.9)$$

Finally, and taking into account the dependency of the AMO aperture on velocity, the maximum output time can be evaluated for a given minimum propagation velocity V_{min} as

$$t_2 \leq \frac{2}{V_{min} \sqrt{(\gamma_1^2 + \gamma_2^2 - 2\gamma_1\gamma_2 \cos \Delta\theta)(1 - \xi_1^2)}}. \quad (2.10)$$

where γ_1 and γ_2 are given by

$$\gamma_1 = \frac{\frac{\partial t_2}{\partial \xi_1}}{h_2 t_2 \sin \Delta\theta}, \quad (2.11)$$

$$\gamma_2 = \frac{\frac{\partial t_2}{\partial \xi_2}}{h_1 t_2 \sin \Delta\theta}, \quad (2.12)$$

To avoid truncation artifacts, a tapering function should be applied to the edges of the operator aperture.

APPLICATION OF AMO TO A 3D MARINE DATA SET

This section presents the results of applying AMO for partial stacking of a 3D marine data set. The data is courtesy of Elf Aquitaine and represents a 3D survey over a large salt body in the North Sea. Proper imaging of the data requires 3D prestack depth migration. Given the size of the survey (13.5 km x 10.5 km), the cost of depth imaging is considerably high. The goal is to reduce the size of the data by partial stacking before migration since the cost of migration is roughly proportional to the size of input data. The resulting partial stacks can then be migrated separately, and either stacked together to form the final image or individually analyzed for amplitude and velocity variations.

Conventional processing applies NMO before partial stacking in order to increase the coherency across the input traces and reduce noise by destructive interference. However, such trace-to-trace transformation is insufficient in the presence of dipping energy and acts as a dip filter for diffractions and dipping beds. Therefore we need to apply AMO before stacking in order to insure the preservation of all the dips in the data.

Figure 2.5 shows the depth velocity model for the area. The geology is fairly continuous along the cross-line axis and varies rapidly in the in-line direction as shown in Figure 2.6 which displays the respective velocities of the layers. Figure 4.2 shows an NMO-Stack of the middle offsets (between 1,000 and 2,000 m). The edges of the salt dome create a lot of diffractions visible in the middle of the section between 2.0 and 3.5 s. They are the areas where AMO is expected to make most of the difference. The bright reflections at around 1.6 s are generated at the salt-sediments interface. The fairly steep reflections at the right edge of the section between 2.0 and 2.5 s are caused by the flanks of the salt swells. These dipping reflections also require AMO before stacking in order to preserve their high-frequency components.

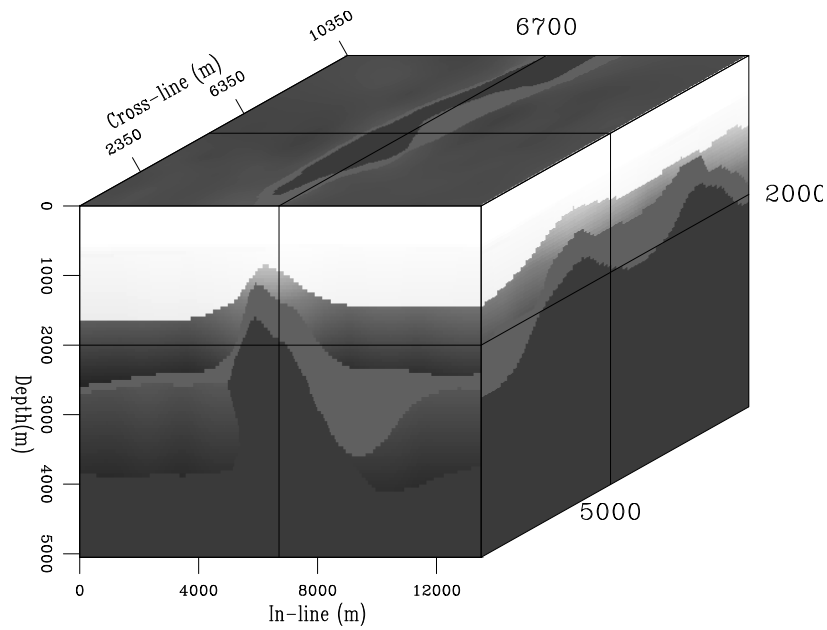


Figure 2.5: Depth velocity model of the survey area. `amo-vel-model` [CR]

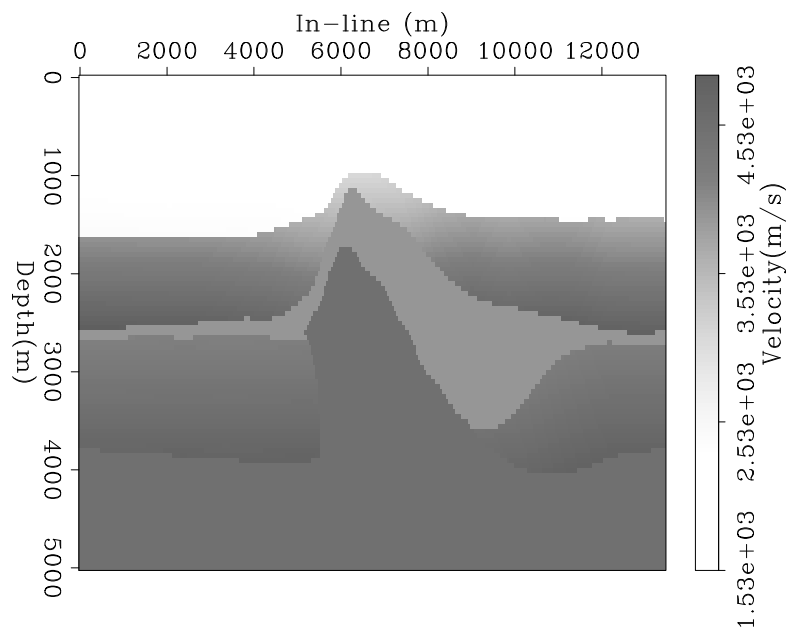


Figure 2.6: Geological in-line section and corresponding velocities of layers. `amo-vel-section` [CR]

The data were acquired using source spacing of 50 meters and receiver spacing of 25 meters for an offset range from 190 m to 3340m. The nominal common-midpoint spacing is 13.33 m in the in-line direction and 25 m in the cross-line direction. To make the data handling and processing quicker, I processed only a subset of the whole data set. I selected a window of 600 time samples that included all major reflections and salt diffractions between 0.6 and 3.0 seconds. I also extracted the central 750 midpoints in the in-line direction, for a total length of 10.0 km, and 120 midpoints in the cross-line, for a total width of 3.0 km. The traces had an offset range from 1000 to 1400 meters and included all recorded azimuths. Figure 2.8 shows the offset-azimuth distribution for the extracted 3D subset.

To test the effects of AMO on the prestack data, I applied two distinct partial stacking methods to the data: NMO followed by partial stacking (NMO-stacking) and NMO followed by AMO and partial stacking (NMO-AMO-stacking). To make the comparison as fair as possible to the conventional methodology of simple NMO-stacking, the traces after NMO were laterally interpolated in the midpoint direction before they were stacked into the output cube. Tests showed that this lateral interpolation preserved the dipping events significantly better than a simple binning procedure. The output model is a regularly sampled cube of 750 by 120 midpoints, with nominal offset of 1,200 meters and effective azimuth of zero degrees. The number of input traces was about 650,000. Therefore, the data-reduction rate achieved by partial stacking is approximately 7.4.

During the preprocessing stage by ELF, a hyperbolic mute with a sharp cut-off was applied to the data to remove the first arrival and the aliased noise at the far offsets. ELF also provided the depth velocity model which needed to be converted to time rms-velocities for NMO processing.

Figure 2.9 compares the results obtained with the two flows described above for the 1,000 – 1,400 m offset range. The figure displays a window of an in-line section, located at 4,150 m along the cross-line axis and centered on the salt body where the data show numerous high-frequency diffractions. Figure 2.9a shows the section obtained by simple NMO-stacking, while Figure 2.9b shows the results of NMO-AMO-stacking. As expected, the addition of AMO to the partial stacking process preserves the diffractions better than simple NMO. Figure 2.9c shows the differences between the two sections; diffractions and other dipping energy

are clearly evident.

Figure 2.11 compares the time slices at 1.36 s, obtained by NMO-stacking (Figure 2.11a), and NMO-AMO-stacking (Figure 2.11b). The difference section (Figure 2.11c) clearly shows that few trends of high-frequency diffractions were not correctly preserved by the conventional process. Some acquisition footprint is also present in the difference section and shows the role of AMO in regularizing the geometry of the subset. Although there are not many gaps in the data, the AMO process interpolated the few missing lines in the survey. For better illustration of the results, Figures 2.10 and 2.12 show the same comparisons on smaller windows from the inline and time-slice sections.

CONCLUSIONS

The AMO operator presented in this chapter is a new partial prestack-migration operator that can be efficiently applied to 3-D prestack seismic data to transform their effective offset and azimuth. AMO is a generalization of the migration-to-zero-offset operators (e.g. DMO) because it can transform data to arbitrary offsets and azimuths. By including AMO in the processing flow we can considerably reduce the computational cost of 3-D prestack depth imaging by reducing the size of the data to be migrated.

Results of applying AMO to a marine dataset from the North Sea showed that AMO improves the accuracy of partial stacking over a range of offsets. In particular, the high-frequency steeply-dipping components of the reflected, or diffracted, energy benefit from the application of AMO. These components are crucial for the correct interpretation of complex fault systems, as well as for high-resolution imaging of complex reservoirs.

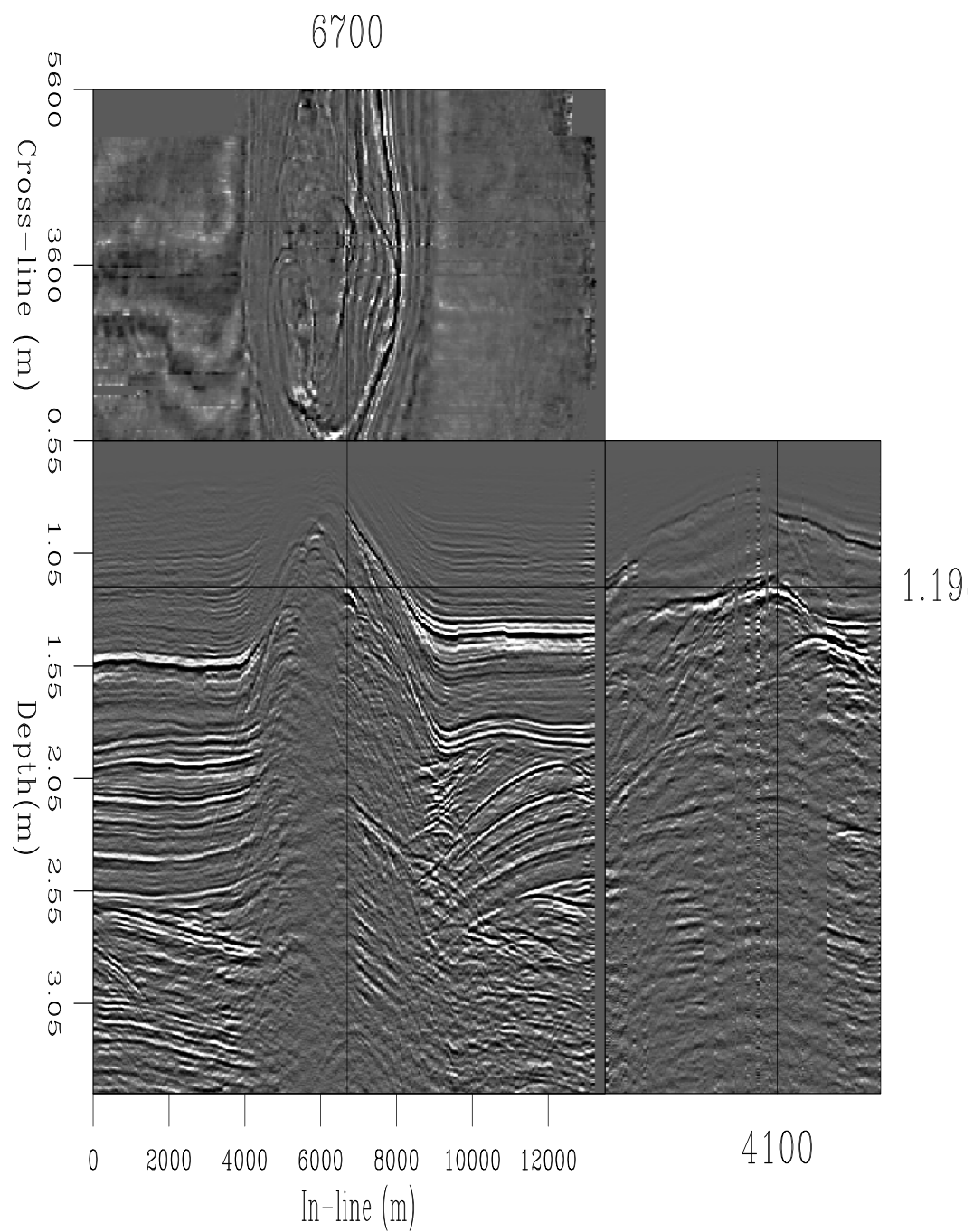


Figure 2.7: NMO-Stack of North Sea data set used for testing AMO. `amo-Mid-stack` [CR]

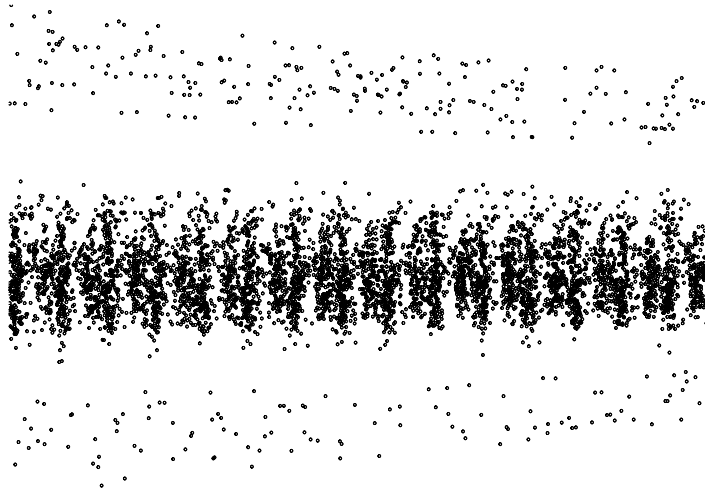


Figure 2.8: Offset-azimuth distribution of the 1,000-1,400 m offset range. amo-off-azim
[CR]

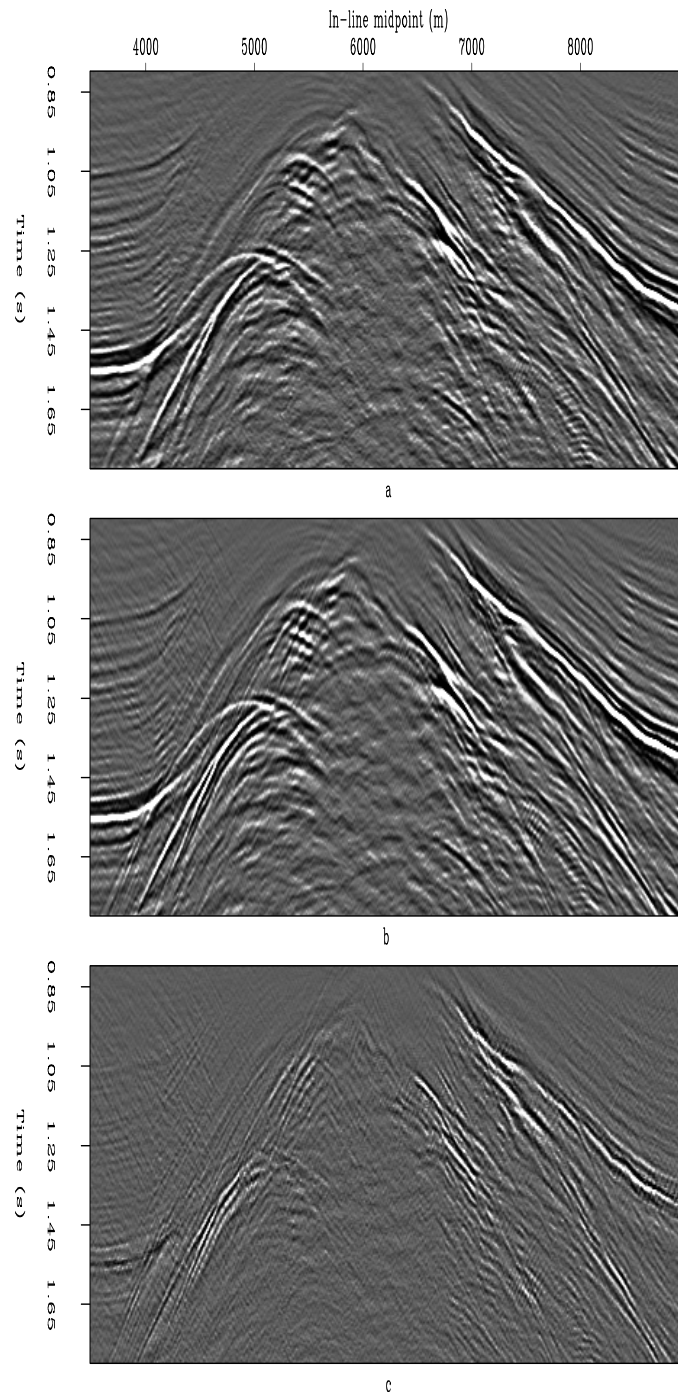


Figure 2.9: In-line sections (4,150 m) for the 1,000 – 1,400 m offset range, obtained by a) NMO-stacking, b) NMO-AMO-stacking, c) subtracting a) from b). `amo-inline` [CR]

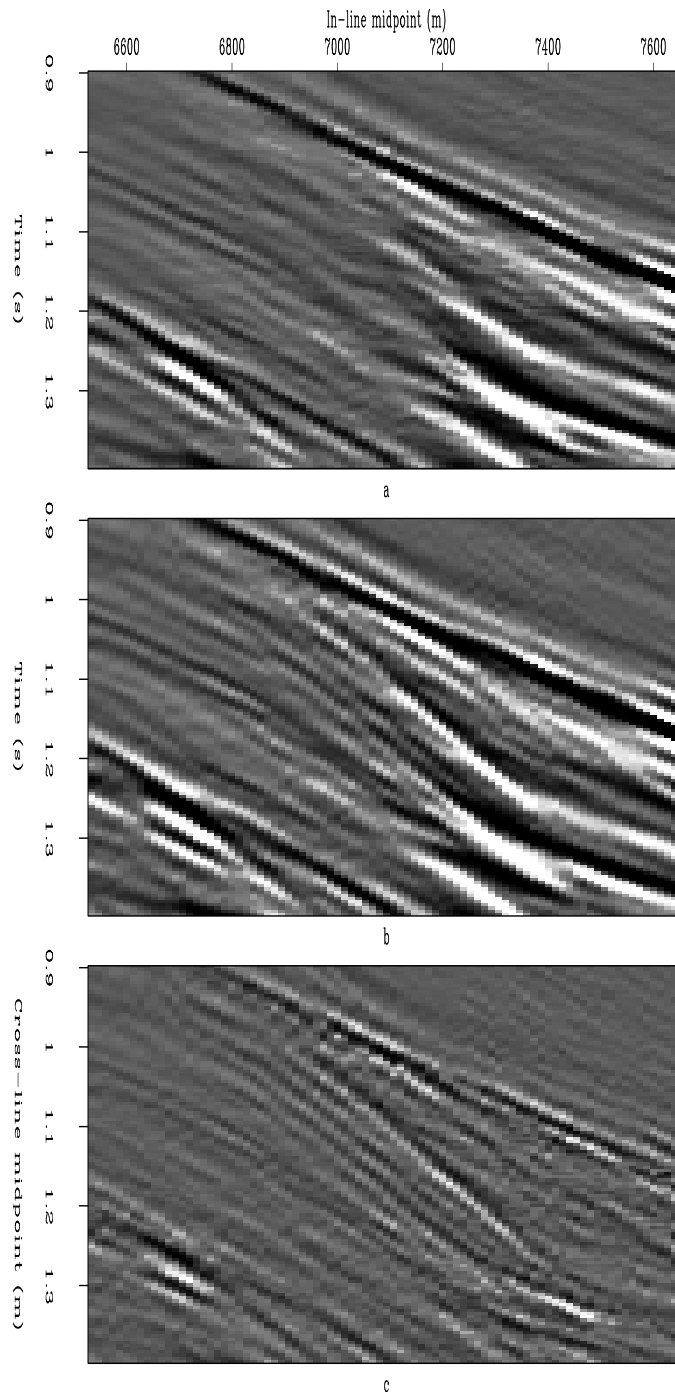


Figure 2.10: Window on the In-line sections (4,150 m) obtained by a) NMO-stacking, b) NMO-AMO-stacking, c) subtracting a) from b). `amo-inline2` [CR]

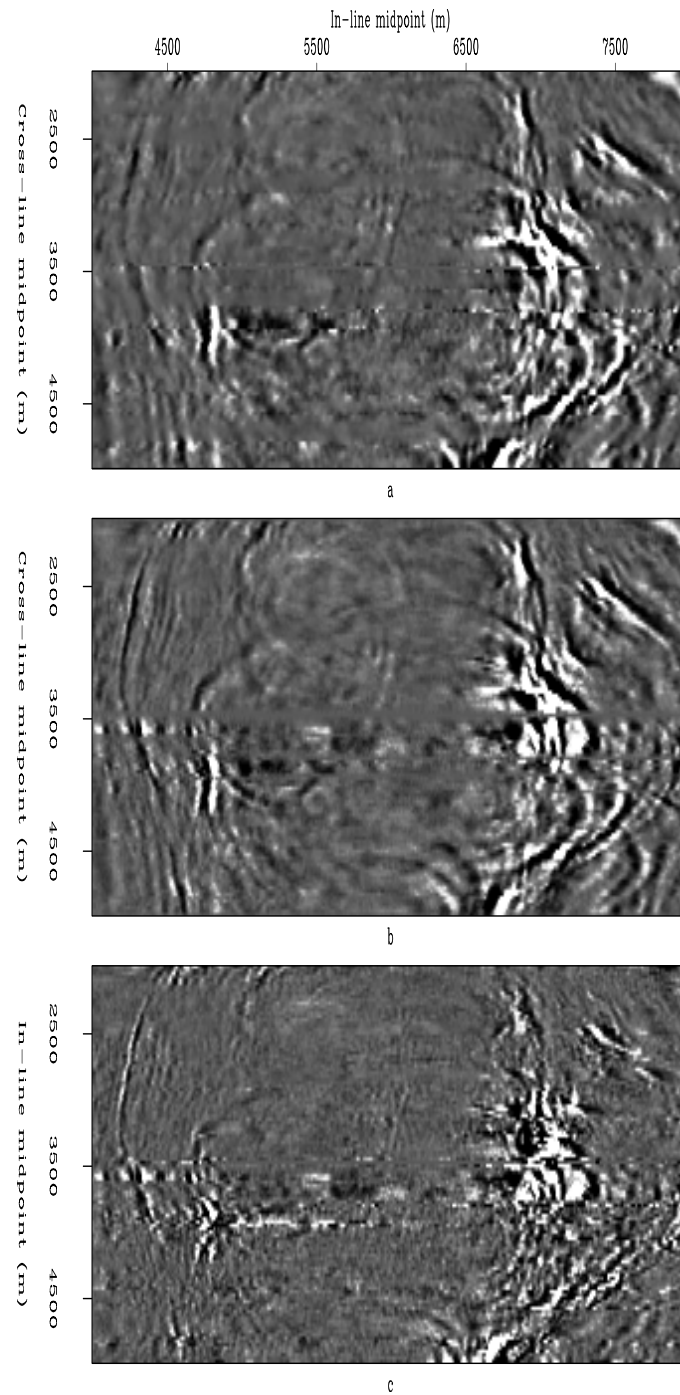


Figure 2.11: Time slices (1.36 s) for the 1000 – 1,400 m offset range, obtained by a) NMO-stacking, b) NMO-AMO-stacking, c) subtracting a) from b). `amo-slice` [CR]

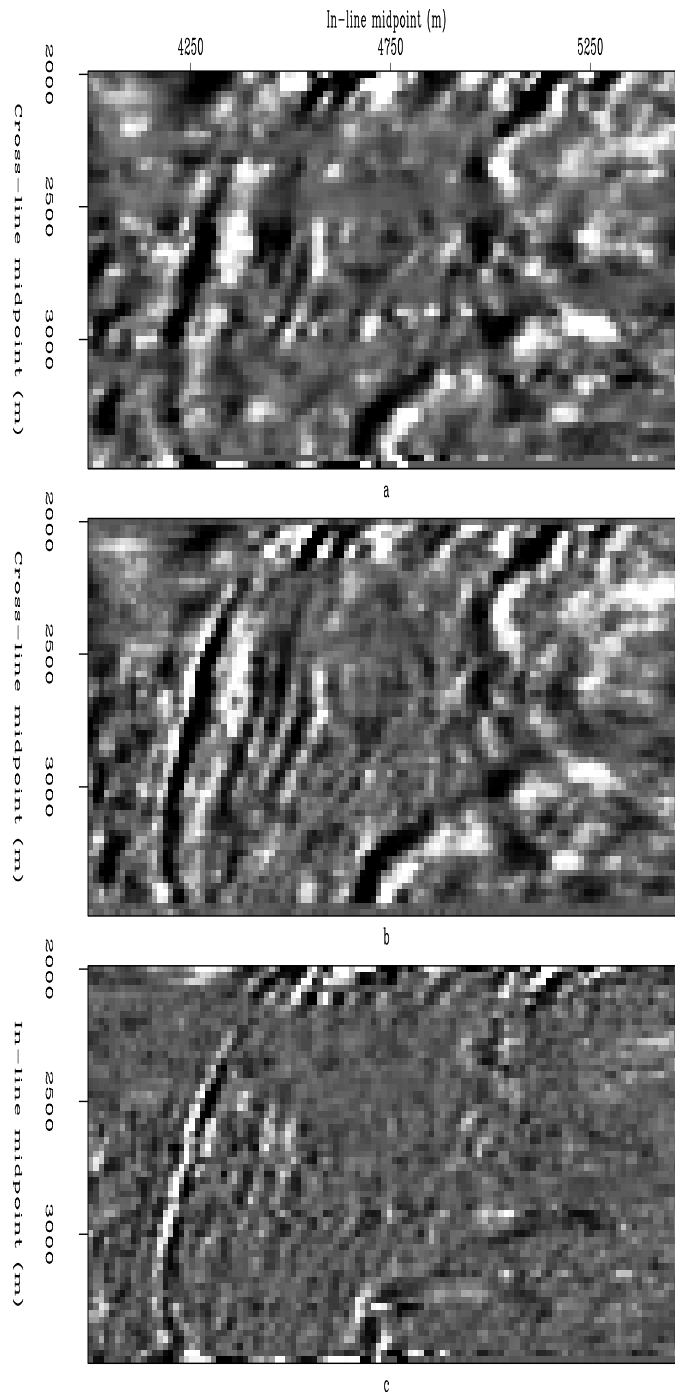


Figure 2.12: Window on the time slices (1.36 s) obtained by a) NMO-stacking, b) NMO-AMO-stacking, c) subtracting a) from b). `amo-slice1` [CR]

Chapter 3

Amplitude-preserving AMO

OVERVIEW

In this chapter, I present my development of a “true-amplitude” function for AMO so that amplitude variations as a function of offset and azimuth are not distorted by the transformation. Beyond the derivation of AMO amplitudes, the Chapter serves as a good example for using asymptotic theory to derive “true amplitude” functions for partial or full prestack imaging operators. The discussions focus on the DMO and AMO operators, however, the same concepts have been used in literature to derive amplitude weights for migration and demigration.

Given that AMO is derived by chaining DMO and inverse DMO, I compare the amplitude behavior of kinematically equivalent DMO operators with various amplitude functions adopted through different definition of “true-amplitude”. I also compare the asymptotic inverse to the adjoint, and derive an amplitude preserving inverse for Zhang’s (1988) DMO and Bleistein’s (1990) Born DMO. Finally, I present a true-amplitude function for AMO and demonstrate the preservation of the reflectivity by the transformation through synthetic examples.

Since the term “true-amplitude” for wave-equation operators is an ill-defined concept, I restrict its definition to be consistent with most interpreters for preserving the peak amplitude of reflection events. The derivations of AMO amplitudes assume continuous wavefields and

the synthetic experiments are conducted on regularly sampled input data.

CHAINING DMO AND INVERSE DMO

The derivation of AMO as the cascade of DMO and DMO^{-1} results into the following expression for the amplitude term,

$$A(\mathbf{x}, \mathbf{h}_1, \mathbf{h}_2, t_1) \approx \frac{2\pi J_1 J_2}{\sqrt{\Delta}}, \quad (3.1)$$

where \mathbf{x} is the output location vector in midpoint coordinates, J_1 and J_2 are the Jacobians in the FK definition of DMO and DMO^{-1} and Δ is the determinant of a Hessian matrix that is independent of the particular DMO of choice. For given input half-offset and time (\mathbf{h}_1, t_1) and output half-offset (\mathbf{h}_2), equation (3.1) describes the weights along the impulse response of AMO in the time-space domain. The Jacobians J_1 and J_2 and the determinant Δ in equation (3.1) are evaluated at the stationary point of the phase function in the integral kernel of AMO.

The amplitude behavior of AMO is thoroughly controlled by the Jacobian terms of DMO and its inverse. Liner and Cohen (1988) argued that the adjoint is a poor representation for an inverse DMO. They showed that the application of Hale's DMO followed by its adjoint inverse results in serious amplitude degradation and therefore they proposed an asymptotic "true-inverse" for Hale's DMO. Similar to their formulation, I derive asymptotic inverses for Zhang's and Bleistein's DMO operators which, as demonstrated later in the text, do preserve the amplitudes better.

INTEGRAL INVERSE DMO

DMO is a method of transformation of finite-offset data to zero-offset data. Let the normal moveout corrected input data be denoted $P_2(t_2, \mathbf{x}_2; \mathbf{h}_2)$ and the zero-offset desired output denoted $P_0(t_0, \mathbf{x}_0; \mathbf{h} = 0)$. Assume known relationships between the coordinates of the general form

$$t_0 = t_0(t_2, \mathbf{x}_2, w_0, \mathbf{k}_0) \quad \text{and} \quad \mathbf{x}_0 = \mathbf{x}_0(\mathbf{x}_2). \quad (3.2)$$

The DMO operator can be defined in the zero-offset frequency ω_0 and midpoint wavenumber \mathbf{k} as (Liner, 1988)

$$P_0(\omega_0, \mathbf{k}_0; \mathbf{h} = 0) = \int d\mathbf{x}_2 \frac{d\mathbf{x}_0}{d\mathbf{x}_2} \int dt_2 \frac{dt_0}{dt_2} e^{+[i\omega_0 t_0(t_2) - \mathbf{k}_0 \cdot \mathbf{x}_0(\mathbf{x}_2)]} P_2(t_2, \mathbf{x}_2; \mathbf{h}_2) \quad (3.3)$$

$$= \int d\mathbf{x}_2 \int dt_2 J_1 e^{+[i\omega_0 t_0(t_2) - \mathbf{k}_0 \cdot \mathbf{x}_0(\mathbf{x}_2)]} P_2(t_2, \mathbf{x}_2; \mathbf{h}_2), \quad (3.4)$$

whereas its inverse can be defined as

$$P_2(t_2, \mathbf{x}_2; \mathbf{h}_2) = \int d\mathbf{k}_0 \int d\omega_0 J_2 e^{-[i\omega_0 t_0(t_2) - \mathbf{k}_0 \cdot \mathbf{x}_0(\mathbf{x}_2)]} P_0(\omega_0, \mathbf{k}_0; \mathbf{h} = 0) \quad (3.5)$$

where

$$J_2 = J_2(t_2, \mathbf{x}_2, \omega_0, \mathbf{k}_0) \quad (3.6)$$

A detailed derivation of J_2 is given by Liner (1988). The method is based on a general formalism (Beylkin, 1985; Cohen and Hagin, 1985) for inverting integral equations such as (A.1). It involves inserting (A.1) into (A.2) and expanding the resulting amplitude and phase as a Taylor series and making a change of variables according to Beylkin (1985). The solution provides an asymptotic inverse for (A.1), where the weights are given by

$$J_2 = \frac{d\omega}{d\omega_0} \frac{d\mathbf{k}}{d\mathbf{k}_0} \left[4\pi^2 \frac{dt_0}{dt_2} \frac{d\mathbf{x}_0}{d\mathbf{x}_2} \right]^{-1}. \quad (3.7)$$

In this expression, $\frac{dt_0}{dt_2} \frac{d\mathbf{x}_0}{d\mathbf{x}_2}$ is the Jacobian of the change of variables in the forward DMO given by

$$J_1 = \frac{\partial(t_0, \mathbf{x}_0)}{\partial(t_2, \mathbf{x}_2)} = \det \begin{bmatrix} \frac{dt_0}{dt_2} & \frac{d\mathbf{x}_0}{d\mathbf{x}_2} \\ \frac{d\mathbf{x}_0}{dt_2} & \frac{d\mathbf{x}_0}{d\mathbf{x}_2} \end{bmatrix} \quad (3.8)$$

which reduces to $J_1 = \frac{dt_0}{dt_2} \frac{d\mathbf{x}_0}{d\mathbf{x}_2}$, assuming the general coordinate relationships (3.2) where \mathbf{x}_0 is independent of t_2 , leading to a zero lower left element in the determinant matrix above.

The quantity $\frac{d\omega}{d\omega_0} \frac{d\mathbf{k}}{d\mathbf{k}_0}$ is the inverse of the Beylkin determinant, H , and is given by

$$H^{-1} = \frac{\partial(\omega, \mathbf{k})}{\partial(\omega_0, \mathbf{k}_0)} = \det \begin{bmatrix} \frac{d\omega}{d\omega_0} & \frac{d\mathbf{k}}{d\mathbf{k}_0} \\ \frac{d\mathbf{k}}{d\omega_0} & \frac{d\mathbf{k}}{d\mathbf{k}_0} \end{bmatrix}. \quad (3.9)$$

If we recognize that \mathbf{k} is independent of ω_0 , then the lower element of H^{-1} is zero and (3.9) reduces to

$$H^{-1} = \frac{d\omega}{d\omega_0} \frac{d\mathbf{k}}{d\mathbf{k}_0}, \quad (3.10)$$

where ω and \mathbf{k} are, respectively,

$$\omega = \omega_o \frac{d}{dt_2} [t_0(t_2)] \quad (3.11)$$

$$\mathbf{k} = \mathbf{k}_0 \frac{d}{d\mathbf{x}_2} [\mathbf{x}_0(\mathbf{x}_2)] . \quad (3.12)$$

Notice that ω and \mathbf{k} depend on the coordinate relationships (3.2). Therefore, the Beylkin determinant, H , varies according to the DMO operator but is constant for kinematically equivalent operators.

Hale DMO and its inverse

Starting from the following coordinate relationships between a finite-offset data and its equivalent zero-offset data

$$t_0 = t_2 \left[1 + \left(\frac{\mathbf{k} \cdot \mathbf{h}_2}{\omega_o t_2} \right)^2 \right]^{1/2} \equiv t_2 A_2 \quad \text{and} \quad \mathbf{x}_0 = \mathbf{x}_2 \quad (3.13)$$

After differentiating (3.13) and taking into account a factor of $1/2\pi$ as scaling for the spatial Fourier transform we can write (3.7) as

$$J_2 = \frac{A_2}{2\pi} \frac{d\omega}{d\omega_o} \frac{d\mathbf{k}}{d\mathbf{k}_0} . \quad (3.14)$$

The remaining task reduces to performing the necessary derivatives, and, with some algebra, one can verify that H reduces to the simple expression (Liner and Cohen, 1988)

$$H = \frac{A_2^3}{2A_2^2 - 1} \quad (3.15)$$

and, therefore, we arrive at the inversion amplitude function

$$J_2 = \frac{1}{2\pi} \left[1 + \frac{\mathbf{k}^2 \mathbf{h}^2}{\omega_0^2 t_2^2 A_2^2} \right]. \quad (3.16)$$

For a detailed derivation, the reader should refer to the original work of Liner (1988).

Black/Zhang DMO and its inverse

Similar to the preceding discussion, I start the derivation for an asymptotic inverse for Black/Zhang's DMO by recognizing the coordinate relationships,

$$t_0 = t_2 A_2^{-1} \quad \text{and} \quad \mathbf{x}_0 = \mathbf{x}_2 - \frac{\mathbf{k} \mathbf{h}^2}{\omega_0 t_2 A_2} \quad (3.17)$$

The Jacobian of the change of variables in the forward DMO is given by

$$J_1 = \frac{\partial(t_0, \mathbf{x}_0)}{\partial(t_2, \mathbf{x}_2)} = \frac{2A_2^2 - 1}{A_2^3}, \quad (3.18)$$

which has the familiar form of Zhang's (1988) and Black's (1993) Jacobian. Zhang based his derivations on kinematic arguments that considered a fixed reflection point rather than a fixed midpoint. This derivation takes into account the reflection-point smear (Deregowski and Rocca, 1981; Black et al., 1993a), which means that the input event at location \mathbf{x}_2 will be positioned by DMO to the correct zero-offset location \mathbf{x}_0 .

To compute the Beylkin determinant for Black/Zhang Jacobian I begin by writing the phase function in the DMO integral kernel as

$$\Phi = \omega t_0 - \mathbf{k} \cdot \mathbf{x}_0 \quad (3.19)$$

$$= \omega A_2 t_2 - \mathbf{k} \cdot \mathbf{x}_2 \quad (3.20)$$

The phase in equation (3.20) is identical to the phase function in Hale's DMO and, therefore, substituting for ω and \mathbf{k} back in (3.11) and (3.12) and differentiating with respect to ω_0 and

\mathbf{k}_0 , we end up with the following expression for H^{-1} :

$$H^{-1} = \frac{A_2^3}{2A_2^2 - 1}. \quad (3.21)$$

Therefore, the Beylkin determinant for Black/Zhang's DMO becomes

$$H = \frac{2A_2^2 - 1}{A_2^3} \quad (3.22)$$

which is the same as that for Hales's DMO.

Finally, by substituting back in (3.7) and accounting for the $1/2\pi$ factor in the spatial Fourier transform, we obtain an expression for the weights of an asymptotic inverse for Black/Zhang's DMO:

$$J_2 = \frac{1}{2\pi} \quad (3.23)$$

These weights have been also derived independently by Paul Fowler (personal communication).

Bleistein Born DMO and its inverse

Starting from a different argument, Bleistein (1990) proposed a DMO operator that he derived from a Born approximation for modeling wave propagation. This new operator, named Born DMO (BDMO), is kinematically equivalent to Hale's (1984) DMO and Zhang's (1988) DMO and only differs from each of them by a simple amplitude factor. This new Jacobian is defined as

$$J_1 = \frac{\partial(t_0, \mathbf{x}_0)}{\partial(t_2, \mathbf{x}_2)} = \frac{2A_2^2 - 1}{A_2}. \quad (3.24)$$

Similar to the previous analysis, and recognizing that this Born DMO is kinematically equivalent to Hale's DMO, the weights for its inverse are then,

$$J_2 = \frac{1}{2\pi A_2^2}. \quad (3.25)$$

Inverse DMO vs. Adjoint DMO

Figures 3.1 and 3.2 compare results of different inverse DMO operators. The left panel of Figure 3.1 is an in-line section from a common offset cube consisting of five unit-amplitude spikes. The offset is 800m and the CMP spacing is 20 m in both directions. I compare the output of each true inverse to the output of the adjoint (Ronen, 1987). The ideal output would be five spikes with unit amplitudes. The table below summarizes the output of each inverse DMO for increasingly deep spikes.

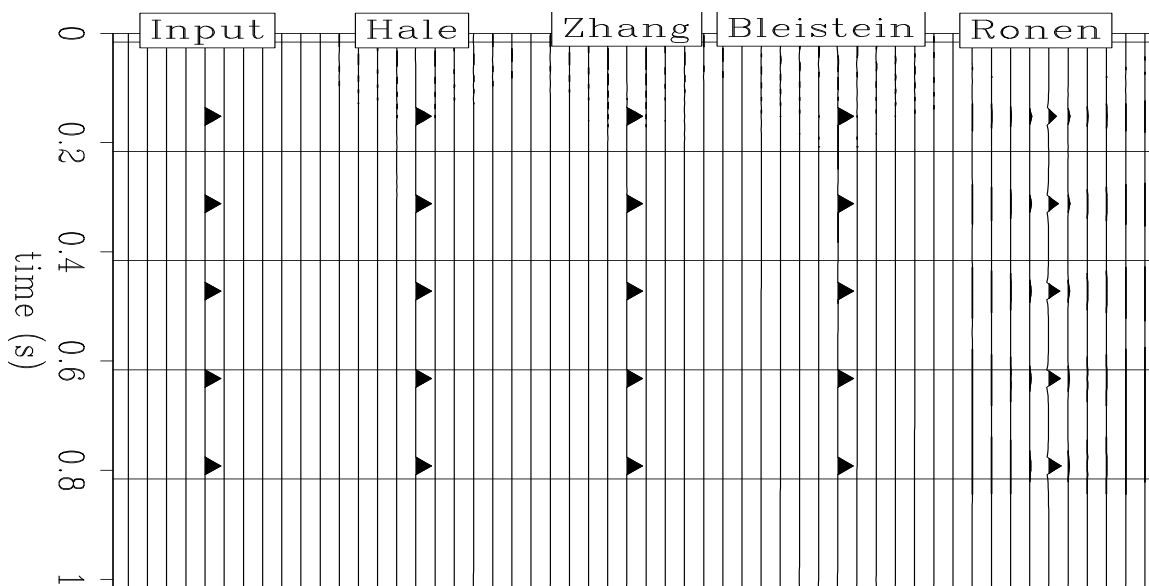


Figure 3.1: From left to right: input data, cascade of several DMO operators with their inverse.
 amp-Spike [ER]

IDEAL Amp.	Hale	Black/Zhang	Bleistein	Ronen
1.00	.76	.76	.76	.35
1.00	.95	.95	.95	.66
1.00	.97	.97	.97	.77
1.00	.97	.97	.97	.82
1.00	.98	.98	.98	.86

Figure 3.2 represents a similar test for a synthetic model consisting of a single bed dipping at 35 degrees angle. The input data is a constant-offset section recorded at an offset of 1600 m with CMP spacing of 25 m. Each DMO operator is applied to the input section to construct its zero-offset equivalent data. The zero-offset sections are then back projected to the original offset of 1600 m using the inverse DMO process. The plot of peak amplitudes from the cascade of each DMO with its asymptotic inverse coincides perfectly with the original amplitudes from the constant-offset input section. On the same graph I also display the peak amplitudes from the cascade of DMO with its adjoint. The results of the adjoint clearly fall below the theoretical values.

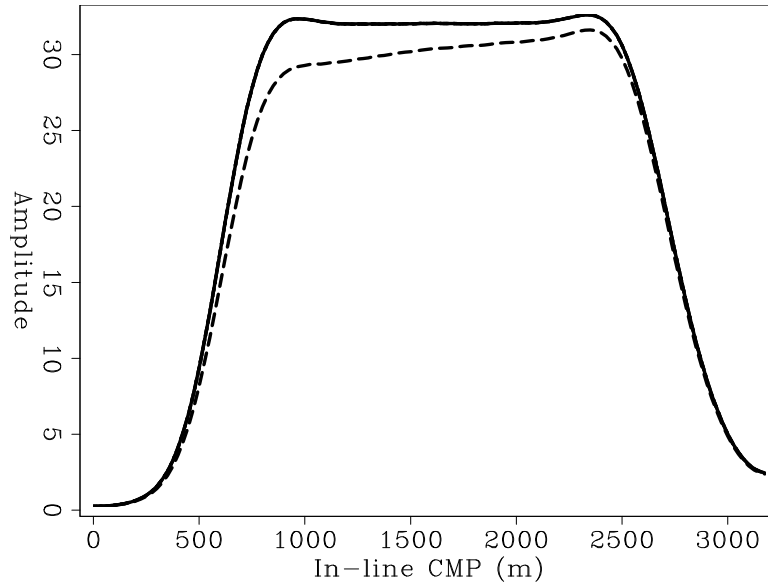


Figure 3.2: Peak amplitudes along a dipping event from the cascade of several DMO operators and their inverse. The solid curve is the result of the adjoint inverse. The results of the asymptotic inverse for Hale, Zhang, and Bleistein operators coincide with original input amplitudes `amp-inv-dmo` [CR]

TRUE-AMPLITUDE DMO

The goal is to define an amplitude-preserving AMO from a true amplitude DMO and its true amplitude inverse. To select a true-amplitude DMO, I test the amplitude preservation by the

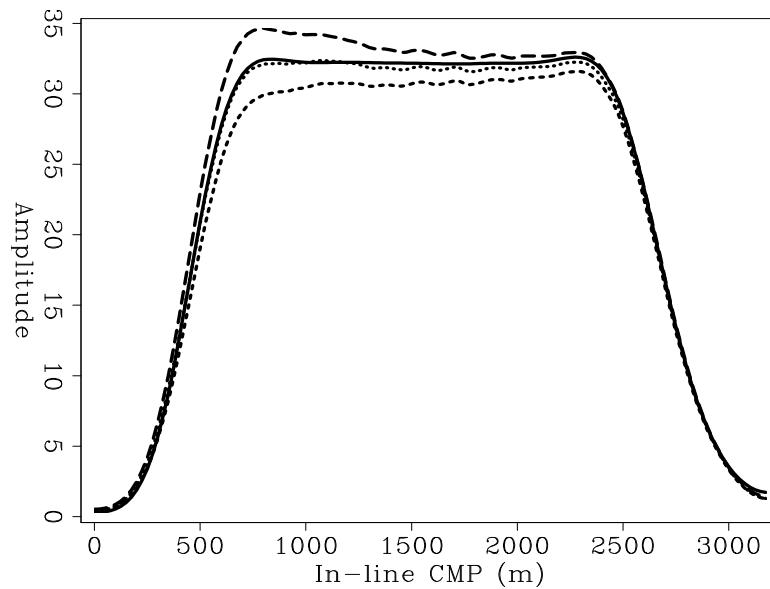


Figure 3.3: Peak amplitudes along a dipping event from a zero-offset section obtained by different DMO operators. The continuous curve is the the predicted result, the dashed curve is Hale's result, the dotted curve is Black/Zhang's output and the large dashed curve (top curve) is Bleistein's output `amp-dmo` [CR]

DMO transformation applied to the dipping bed in the previous experiment. The input was corrected for normal moveout and spherical divergence. Figure 3.3 shows the peak amplitudes from the forward DMO operators compared to the theoretical amplitude for zero-offset equivalent data generated by Kirchhoff modeling. The theoretical curve almost coincides with the amplitudes of Zhang's DMO. The amplitudes given by Hale's algorithm fall below the theoretical curve whereas the peak-amplitudes from Bleistein's DMO overshoot the correct amplitudes.

The difference between Bleistein's DMO and Black/Zhang's DMO results from a philosophical difference about the definition of "true-amplitude". While the goal in the synthetic tests was to preserve the peak amplitude of each reflection event, Bleistein's algorithm is based on preserving the spectral density of the image wavelet. A second difference results from the sequence in the processing flow surrounding DMO. A divergence correction must be applied to the input prior to applying Black/Zhang's DMO, whereas both input and output of Bleistein's DMO decay with spherical divergence factors of $\frac{1}{t_2}$ and $\frac{1}{t_0}$, respectively. These two

differences account for the A^2 factor between the two Jacobians leading to higher weights on Bleistein's DMO, which results in higher peak amplitudes than those on the predicted curve.

On the other hand, the difference between Black/Zhang's DMO and Hale's DMO results from the fact that the former algorithm accounts for the reflection point smear and, therefore, correctly positions input events at their true zero-offset locations. The two Jacobians differ by a factor of

$$\frac{B_Z}{B_H} = \frac{2A^2 - 1}{A^2} \quad (3.26)$$

Because this ratio being always larger than 1, it leads to lower weights on Hale's operator, which explains the lower peak amplitudes measured along the dipping event from Hale's DMO.

Consequently, to be consistent with the original definition of preserving the peak amplitudes of reflection events, I define the amplitude function of AMO in terms of Black/Zhang's DMO and its asymptotic inverse.

AMPLITUDE-PRESERVING AMO

This section examines the amplitude behavior of AMO through numerical experiments on a dipping bed model. In each AMO reconstruction, the output amplitudes are compared to the theoretical amplitudes predicted by synthetic modeling. The three experiments consisted of applying AMO for azimuth rotation, absolute-offset continuation and vector-offset transformation. The input data simulate a constant-offset section recorded at an offset of 1600 meters and azimuth of 5 degrees, measured from the dip direction (the in-line direction). Figure 3.4 compares the AMO reconstructed amplitudes to the theoretical amplitudes for each experiment.

Figure 3.4a shows the results of applying AMO to rotate the geometry by 40 degrees while keeping the offset constant. The peak amplitudes extracted from the AMO result at the new azimuth of 45 degrees are almost identical to the theoretical amplitudes predicted by modeling. Similar to 3.4a, Figure 3.4b compares the results of AMO applied for an offset continuation of 800 meters. The transformation is a 2D operation since the azimuth is held constant. The peak

amplitudes from the 800 meter offset-section follow the theoretical amplitudes very closely with an error of less than a few percent. Finally, figure 3.4c shows the amplitude preservation by AMO when applied as a full 3D operator to rotate the azimuth by 40 degrees and change the offset by 800 meters. The AMO transformation again correctly reconstructed the peak amplitudes at the new geometry. The amplitude curves match very closely and the differences are mainly attributed to cumulative errors in the processing sequence surrounding AMO, which includes spherical divergence and NMO corrections prior to AMO and inverse NMO after AMO.

CONCLUSIONS

I presented an amplitude-preserving function for the AMO operator that enables accurate implementation of an AMO algorithm on regularly sampled data. The derivation of the amplitude is consistent with the definition of most interpreters for preserving peak amplitudes of reflection events. Numerical experiments showed that an AMO operator based on Zhang's DMO cascaded with its true inverse best reconstructs data amplitudes. The new amplitude function defines an amplitude-preserving azimuth moveout.

ACKNOWLEDGMENTS

I thank Norman Bleistein, Paul Fowler, Chris Liner and Mihai Popovici for useful discussions on DMO and inverse DMO.

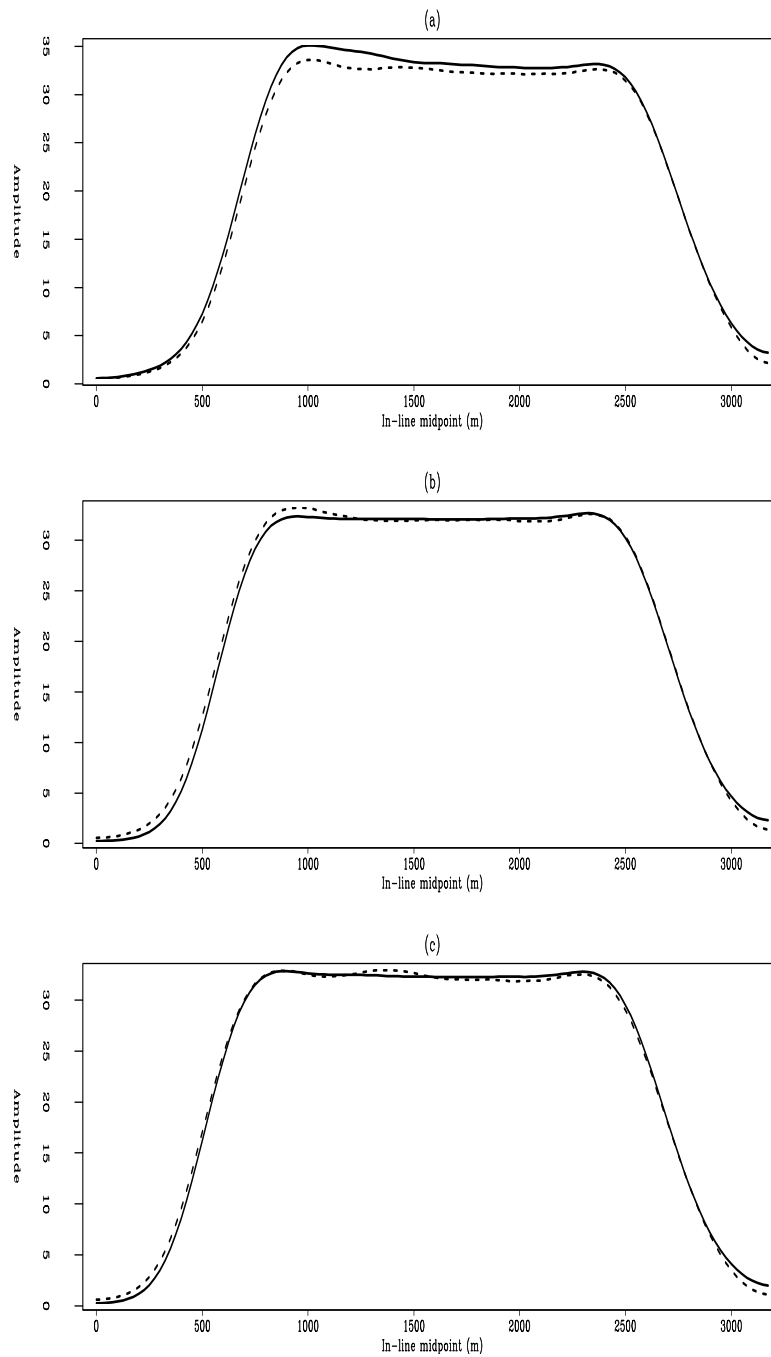


Figure 3.4: Amplitude preservation by AMO: the dashed curve are the peak amplitudes from the AMO result. The solid curve represents the predicted amplitudes by Kirchhoff modeling. (a) azimuth rotation by 45 degrees; (b) offset continuation by 800 meters; (c) azimuth rotation and offset continuation. `amp-comp-amo` [CR]

Chapter 4

True-amplitude Kirchhoff imaging

OVERVIEW

In this chapter I present a new approach for the Kirchhoff imaging of irregularly sampled 3D data. First, I discuss the discrete representation of integral operators as matrix-vector multiplication where each row of the matrix corresponds to a summation surface and each column corresponds to an impulse response. Due to irregularities in seismic coverage, the columns and rows are generally badly scaled. Therefore I apply a diagonal transformation to balance the rows of pull (sum) operators and the columns of push (spray) operators. The diagonal weighting is essentially a normalization by the response of a flat event. It calibrates the image for the effects of irregular coverage of the survey and varying illumination in the subsurface. Next, in the context of common azimuth processing I introduce a new “true-amplitude” sequence for processing wide-azimuth 3D surveys. The method employs the AMO operator to regularize the coverage of the survey and reduce the size of the prestack data by partial stacking. The AMO transformation organizes the data as common-azimuth (CA) and common-offset (CO) cubes and potentially enables reliable analysis of AVO-AZ (amplitude versus offset and azimuth) on the migrated data. Finally, in the last section of the chapter, I present the results of applying the imaging sequence to a 3D land survey from the Canadian Shorncliff region. I show the effectiveness of AMO in regularizing the geometry of the data, and the application of the normalization technique to reduce the effects of fold variations.

DISCRETE KIRCHHOFF IMPLEMENTATIONS

Kirchhoff operators represent a class of linear transformations based on integral solutions to the wave equation. The implementation of integrals as discrete summation reduces to a matrix-vector multiplication where we hardly ever write down the matrices. The linear operation transforms a space to another space (e.g., a data space \mathbf{d} to a model space \mathbf{m}). These spaces are simply represented by vectors whose components are packed with numbers. The relation between data and model is then given by the linear system of equations:

$$\mathbf{d} = \mathbf{L}\mathbf{m}. \quad (4.1)$$

Equation (4.1) represents a forward modeling relation, where the goal of imaging is to perform the inverse of these calculations, i.e., to find models from the data. Mathematically, this is equivalent to estimating the inverse of \mathbf{L} .

True-amplitude imaging

The derivation of the forward-modeling operator provides insight into the form of the inversion operator. In generating the seismic model, each trace is modeled as a weighted sum of image sources on a reflector. Therefore, Kirchhoff imaging of seismic data involves a weighted sum of filtered surface-recorded traces where the weights are deduced from inversion theory. The resulting algorithms are then applied to the discrete seismic data through the linear transformation

$$\mathbf{m} = \mathbf{F}\mathbf{d}. \quad (4.2)$$

True amplitude imaging aims at deriving the proper weights along the summation surfaces or impulse responses of \mathbf{F} . In the previous chapter, I presented detailed derivations for true-amplitude weights for the azimuth moveout operator. Using a similar approach, Jaramillo and Bleistein (1997) derived amplitude-preserving weights for migration and demigration based on the Kirchhoff modeling formula. Then using the superposition principle they derived two alternative operators to perform migration as isochron superposition and demigration as diffraction superposition. I find the two approaches rather easier to understand using Claerbout's

terminology for push and pull operators defined below.

Push and Pull operators

Jon Claerbout (1999) writes: “*The simplest and most fundamental linear operators arise when a matrix operator reduces to a simple row or column.*” A row is a summation operation and a column is an impulse response. If the inner loop of a matrix-multiply ranges within a *row*, the operator is called *sum* or *pull*. If the inner loop ranges within a *column*, the operator is called *spray* or *push*.

NORMALIZATION OF KIRCHHOFF OPERATORS

For ideal acquisition geometries, the previous analysis ensures amplitude-preserving operators defined by well-behaved, full-rank matrices. Problems arise in 3D because of the the irregular coverage of seismic surveys which results in an abundance of seismic traces in some bins and missing data in others.

Considering an imaging operator \mathbf{F} (for instance $\mathbf{F} = \mathbf{L}^{-1}$), each row of \mathbf{F} corresponds to an output bin and each column corresponds to a data trace. Due to the irregular coverage, the columns and rows of \mathbf{F} are not balanced and the matrix is ill-conditioned. To improve its condition, I propose two formulations for row and column scaling which I refer to as *image normalization* and *data normalization*. They involve pre- and post-multiplying the operator \mathbf{F} by a diagonal matrix whose diagonal entries are the inverse of the sum of the rows or columns of \mathbf{F} . The sum is always positive since Kirchhoff operators are associated with matrices that contain no negative elements.

Row scaling: model normalization

Since each row corresponds to a summation surface, I apply the row normalization to imaging operators implemented as (sum) pull operators, and solve the normalized system:

$$\mathbf{m} = \mathbf{R}^{-1} \mathbf{F} \mathbf{d} \quad (4.3)$$

where the sum of the elements of each row is along the diagonal of \mathbf{R} .

The solution in (4.3) is equivalent to applying the imaging operator \mathbf{F} followed by a diagonal transformation \mathbf{R}^{-1} . Therefore, I refer to this normalization as *model* or *image normalization*. Given that each row of \mathbf{F} corresponds to an output bin, \mathbf{R}^{-1} represents a normalization by the coverage after imaging. This coverage is the *imaging fold*, e.g. AMO fold, DMO fold ... etc.

Column scaling: data normalization

Recall that each column of \mathbf{F} corresponds to an impulse response. I therefore apply column scaling to imaging operators implemented as push operators and solve the system

$$\mathbf{m} = \mathbf{F} \mathbf{C}^{-1} \mathbf{d}, \quad (4.4)$$

where the sum of the elements of each column are on the diagonal of \mathbf{C} .

In equation (4.4) the imaging operator is applied after the data have been normalized by \mathbf{C}^{-1} and, consequently, I will refer to this normalization as *data normalization*. Similar to the imaging fold, \mathbf{C}^{-1} is normalization by the coverage of the modeling operator \mathbf{L} (where $\mathbf{F} = \mathbf{L}^{-1}$).

Normalizing vs scaling of the adjoint

Imaging is often derived as the adjoint of modeling, where in the absence of explicit formulation for \mathbf{F} we seek an approximate inverse for \mathbf{L} . Mathematically, this means that we

approximate an inverse of a matrix of very high order by the transpose (Hilbert adjoint) of \mathbf{L} . Claerbout (1999) points out that unless \mathbf{L} has no physical units, the units of the transpose solution $\mathbf{m}_t = \mathbf{L}^T \mathbf{d}$ do not match those of $\mathbf{m}_t = \mathbf{F} \mathbf{d}$. Given the theoretical (least squares) solution $\mathbf{m}_{lsq} = (\mathbf{L}\mathbf{L}^T)^{-1} \mathbf{F}^T \mathbf{d}$, Claerbout suggests that the scaling units should be those of $(\mathbf{L}\mathbf{L}^T)^{-1}$. He proposes a diagonal weighting function suggested by Bill Symes (private communication) that makes the image $\mathbf{m}_t = \mathbf{W}^2 \mathbf{L}^T \mathbf{d}$, where the weighting function is

$$\mathbf{W}^2 = \text{diag} \left(\frac{\mathbf{L}^T \mathbf{d}}{\mathbf{L}^T \mathbf{L} \mathbf{L}^T \mathbf{d}} \right), \quad (4.5)$$

which obviously has the correct physical units.

In contrast to the scaled adjoint, the normalized solution is unitless. It therefore avoids the ambiguity of guessing approximate weights. The model represents a ratio of two images where the reference image is the output of an input vector with all components being equal to one. This is equivalent to a calibration by the response of a flat event. Similar approaches might exist in practice, often derived in heuristic ways, e.g., the DMO fold (Slawson et al., 1995).

TRUE-AMPLITUDE KIRCHHOFF SEQUENCE

In this section I present a new processing sequence designed mainly for 3D wide-azimuth land surveys. However, after organization of land data as common azimuths, land and marine processing should be similar and the techniques described are applicable to either environment. The basic processing flow in Figure 4.1 outlines the major steps for amplitude preserving-processing. Although the focus is on the imaging step, a good deal of care is required in the preprocessing stage to restore amplitudes and to suppress the noise.

The sequence features two wave-equation processes, namely AMO and prestack migration where both algorithms preserve the angle-dependent reflectivity. Given the scope of this work, I only developed a depth-dependent prestack depth migration for better control of amplitude weights. A band-pass time filter, whose maximum frequency is determined by the local slope of the operator, is applied to avoid the aliasing of the Kirchhoff operator along its

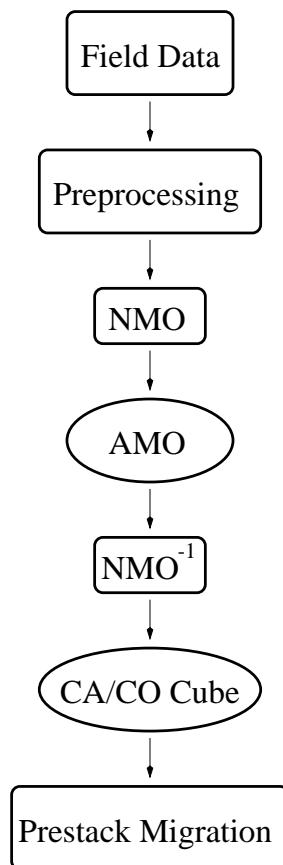


Figure 4.1: Processing flow chart proposed for amplitude-preserving processing of wide-azimuth surveys [kirch-flow](#) [NR]

steep traveltimes slopes.

The data is organized as common-azimuth and common-offset cubes using the AMO transformation. To account for the fold variations of the data and the time-space variability of the operator aperture, AMO is calibrated by the response of a flat event. Finally, prestack migration is applied to the regularized data to determine the location and extent of the anomalies. At this stage any efficient migration algorithm which requires regular grid can be applied to the regularized subset. I chose Kirchhoff migration for consistency in comparing the results of imaging before and after regularization.

APPLICATION TO 3D LAND SURVEY

This section presents the results of applying the true-amplitude sequence to a land data set recorded in the Shorncliff region of Alberta, Canada. The quality of the data is very high as shown in Figure 4.2 which represents an NMO-Stack of the 3D survey. The dominant geology of the area is flat. The objective target is quite shallow (approximately .71 seconds), where some channels cross the section in the in-line direction. Previous studies of the dataset focused on time imaging techniques i.e, DMO processing and inversion to zero offset (Ronen and Goodway, 1998). This chapter addresses the problems related to prestack depth imaging and the effects of irregular sampling on the image quality. The data set is a valuable test case because of the shallow depth of the target zone which makes it sensitive to acquisition geometries.

The survey was designed with the aim of obtaining a high fold coverage for a good quality final stack. The full-stack image can then be used to assess the quality of partial stacks, or, to compare with images obtained by simulating more economic acquisition geometries. The data were acquired using a cross-spread geometry, which provides a wide range of azimuths at near offsets but a narrower range at far offsets (Figure 4.3). The full survey consisted of 1.4 million tramping with maximum offset of 3 km. The shot and receiver spacing is 70 meters for a nominal CMP-spacing of 35 meters in both in-line and cross-line directions.

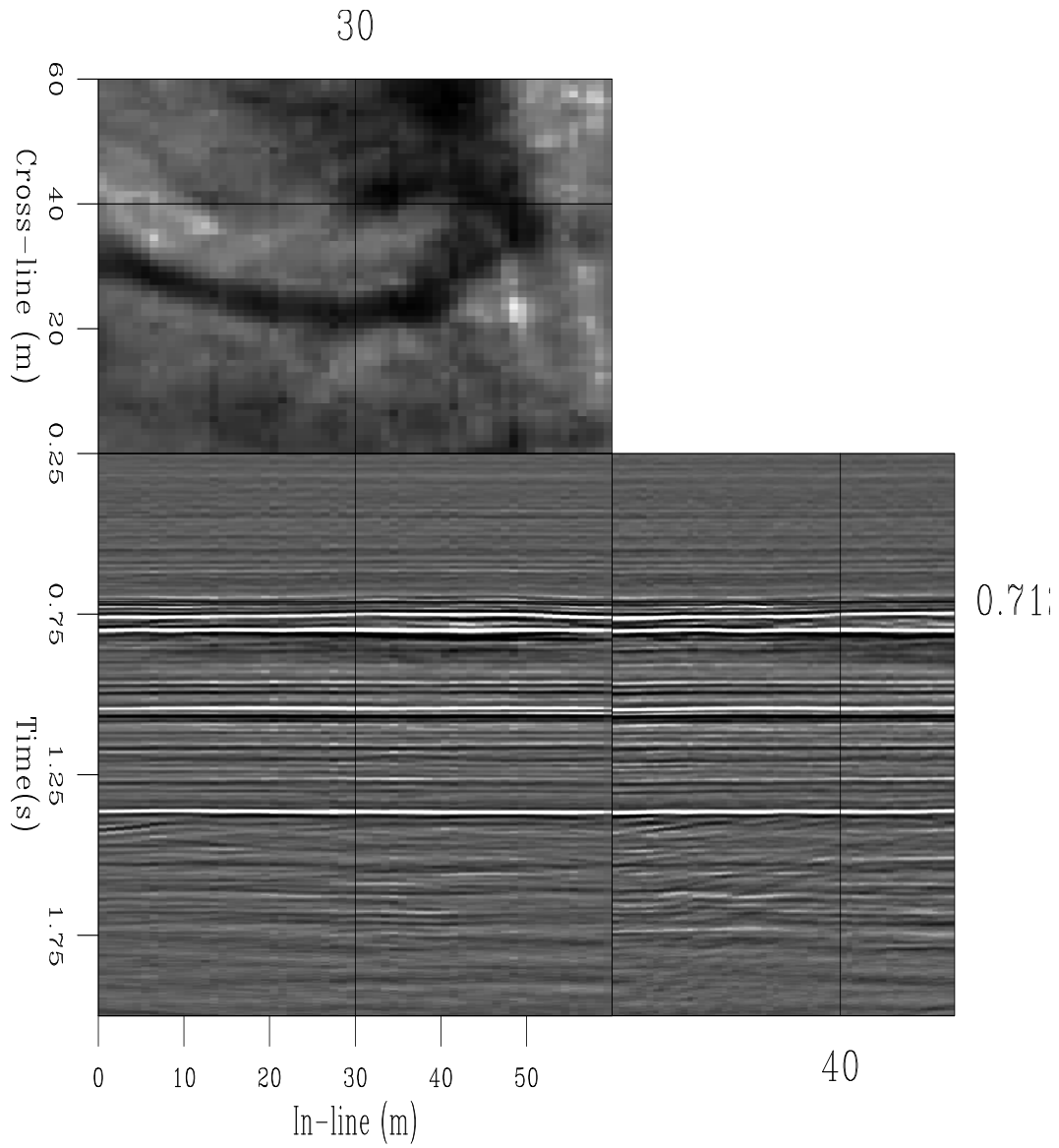


Figure 4.2: NMO-stack of the full over-sampled full survey. `kirch-stack` [CR]

Decimating the field survey

The original dataset is considered oversampled. Therefore I decimated the survey to simulate a realistic acquisition geometry. The shot lines from the original survey were spaced at 140 meters, whereas in the decimated experiment they alternate between 140 and 280 m for an average spacing of 210 m. I also extracted every third receiver line to simulate a line spacing of 210 meters instead of the original 70 meter spacing. Figure 4.4 shows the layout of the source and receiver lines for the 210 meter grid.

To make the data handling and processing quicker, I only considered the central part of the survey which included the river channels. The model is 2.1 km long and 2.1 km wide sampled at 17.5 meter. I extracted a subset of 20,000 traces whose source-receiver offset is between 600 and 1,000 meters and azimuth between -45° and 45° . Figure 4.5 shows the fold distribution for the 3D subset binned at the nominal CMP spacing, whereas Figure 4.6 represents a fold chart for the same offset and azimuth range from the original survey. There is a fundamental problem with the the sub-sampled subset; variations in fold between different bins vary substantially from 0 to a maximum of 10. If not properly accounted for, they can distort the quality of the final image.

Calibration by a flat event

Given the dominantly flat geology of the survey area, the normalization of the image by the response of a flat event is expected to largely reduce the effects of varying illumination of the image. Figure 4.7 shows a time slice of the AMO fold at 0.71 seconds. The high amplitudes are mostly distributed along horizontal stripes in the in-line direction (zero-azimuth) and show direct correlation with the binning fold of the data. Figure 4.8 shows the migration fold at a depth of 920 m that corresponds roughly to 0.71 seconds on the time section. Due to the large aperture of the migration operator compared to the small size of the survey area, the fold is insensitive to the irregular coverage of the survey. It simply displays the distribution of the weights along the migration impulse response. Figures 4.9 and 4.10 show the impulse response of AMO and migration at different time and depth levels. While the aperture of AMO is very compact and decreases with time, the migration aperture is quite large and increases with

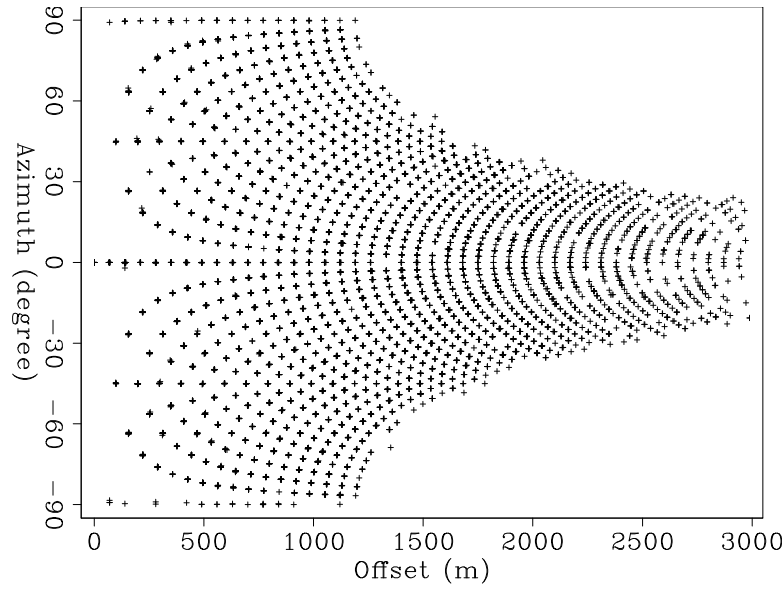


Figure 4.3: Azimuth and offset distribution of the cross-spread survey. `kirch-azim-offset` [CR]

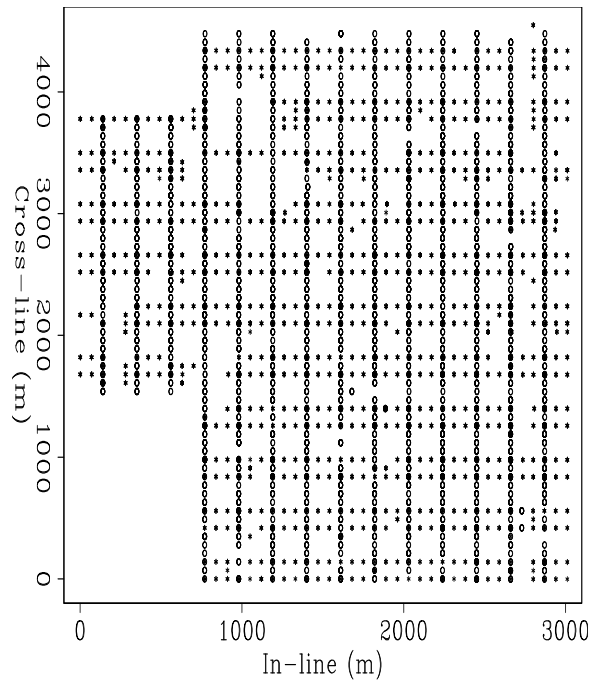


Figure 4.4: Cross-spread acquisition geometry with grid spacing of 210 m. The stars and circles indicate the source and receiver locations respectively. `kirch-survey210` [CR]

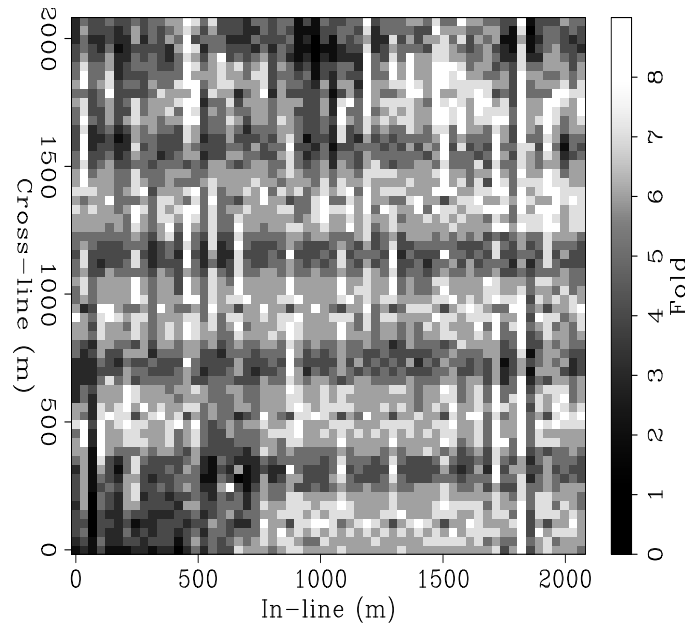


Figure 4.5: Fold diagram for the 3-D subset from the decimated survey. `kirch-fold` [CR]

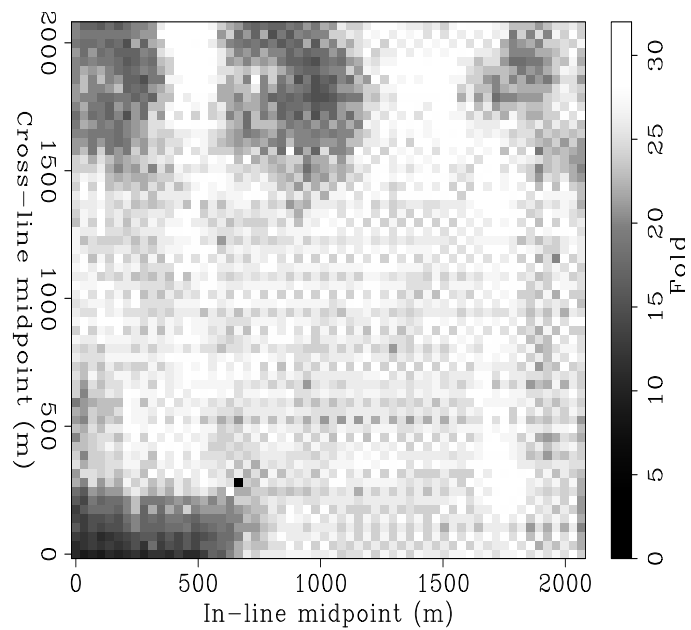


Figure 4.6: Fold diagram for the 3-D subset from the over-sampled survey `kirch-fold-full` [CR]

depth. At 1.5 km deep it is roughly the size of the entire survey area. Therefore, normalizing the migrated image tends to simply compensate for the limited aperture near the edges of the survey rather than correct for the irregular sampling. Consequently, I only migrated the first 1.5 km of the data. For consistency in comparing the results, all images are displayed without any normalization applied to them.

Figure 4.11 compares the time slices at .71 seconds, obtained by un-normalized AMO (Figure 4.11a) and normalized AMO (Figure 4.11b). The difference section (Figure 4.11c) clearly displays trends of the AMO fold that were superimposed on the image. The normalized partial stack, however, shows that few trends of high amplitude were not correctly accounted for by the normalization process. The most evident anomalies tend to occur in zones that originally had low fold coverage and therefore low signal to noise ratio. By normalizing the AMO stack, amplitudes in these areas were boosted up too high in comparison to nice coverage areas. A simple solution to avoid weighting bad signal higher than good data is to normalize by a different function of the fold that provides good trade-off between multiplicity and signal to noise ratio. For instance one can normalize by the square root of the AMO fold (Figure 4.12). Results showed that weighting by some power of the fold between .5 and 1 yields a smooth image with balanced amplitudes.

Figure 4.13 displays a window of an in-line section, located at 1 km along the cross-line axis. Figure 4.13a shows the section obtained by AMO-stacking, while Figure 4.13b shows the section obtained by normalizing the AMO-stack. As expected, the addition of the diagonal scaling to the partial stacking enhances the continuity of the events and balances the amplitudes along the flat reflections. The improvements are better observed along the cross-line dimension as shown in Figure 4.14. This observation is consistent with the fact that the fold coverage varies mostly along the cross-line axis.

Migration after regularization

To test the effects of fold variations on the quality of the migrated image, I applied three distinct imaging schemes to the data. The first consisted of prestack depth migration (PSDM) of the irregularly sampled input. The second applies NMO-stacking followed by inverse NMO

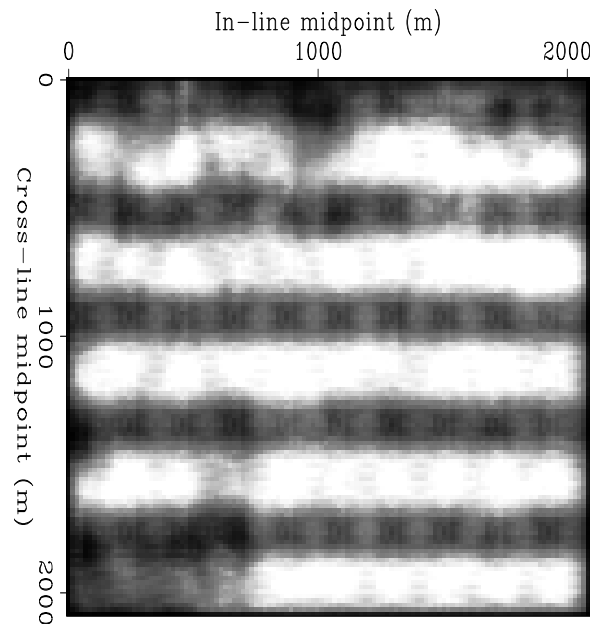


Figure 4.7: AMO fold at 0.71 seconds `kirch-slice-amo-fold` [CR]

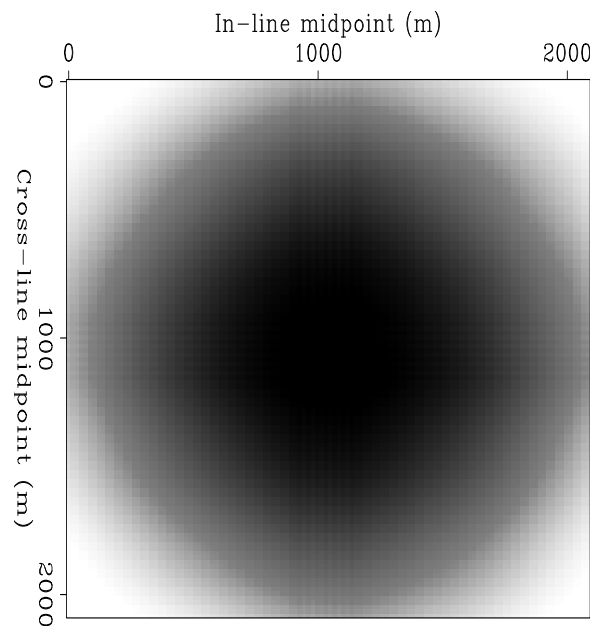


Figure 4.8: Migration fold at 920 m depth `kirch-slice-mig-fold` [CR]

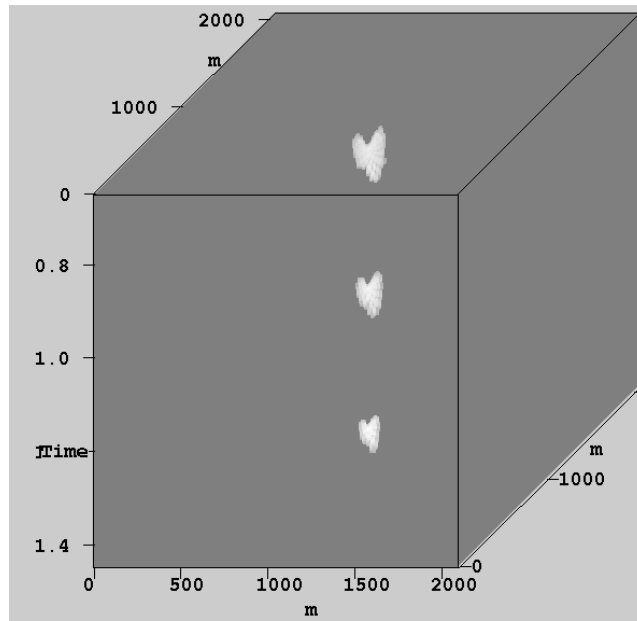


Figure 4.9: AMO impulse response at different time levels for 150m offset continuation and 25 degrees rotation. `kirch-amo-impulse` [NR]

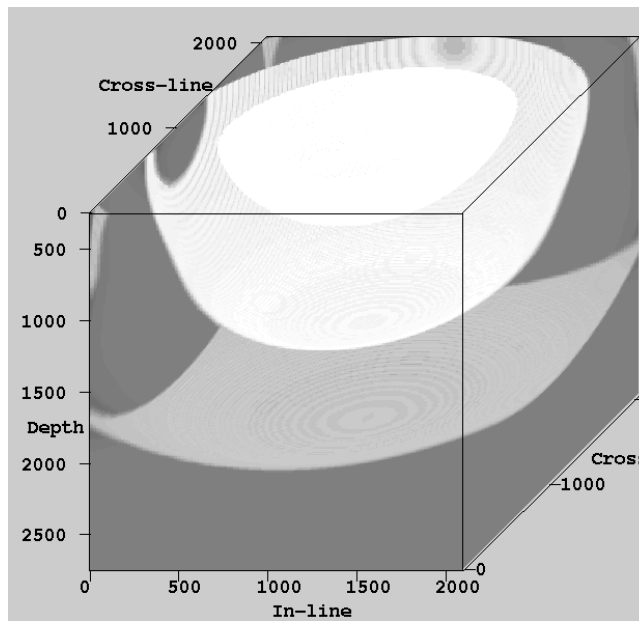


Figure 4.10: Migration impulse response at depth levels corresponding to the time levels on the figure above. `kirch-mig-impulse` [NR]

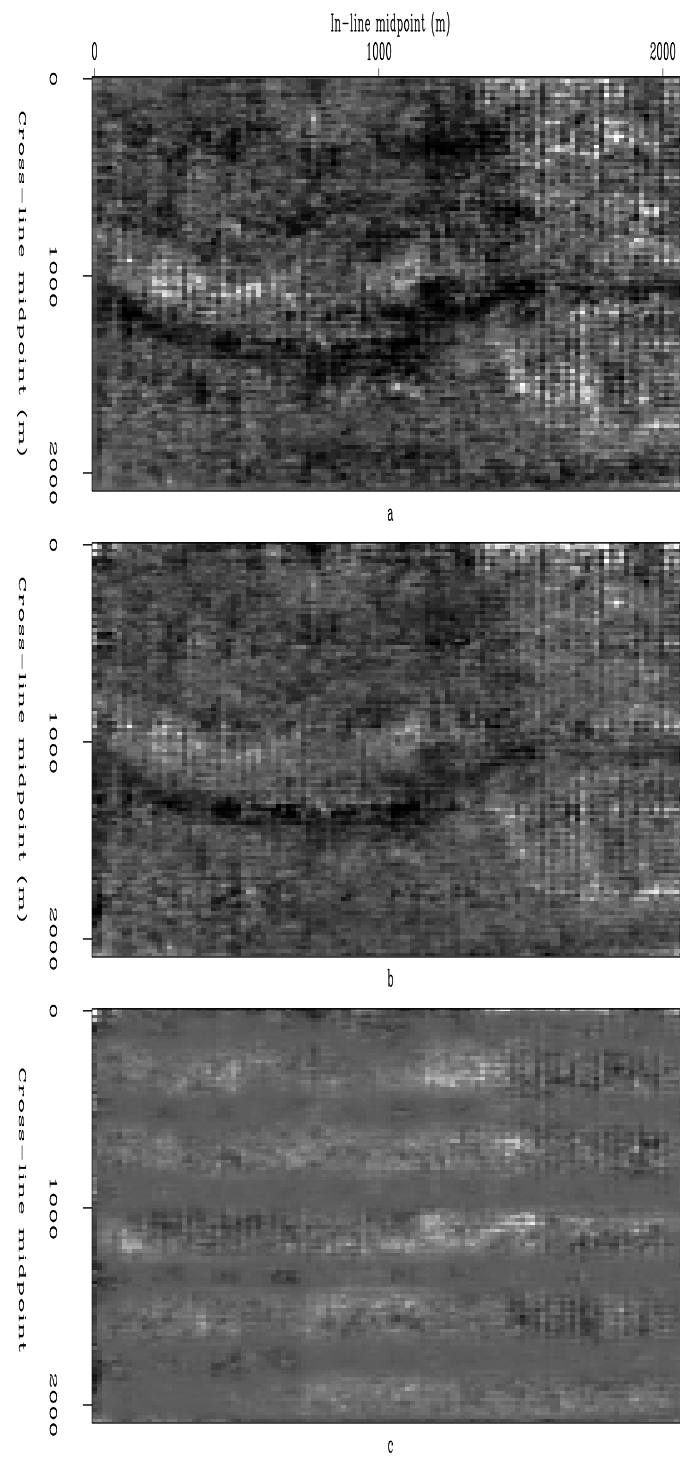


Figure 4.11: Normalizing by the AMO fold: a) un-normalized AMO, b) normalized AMO, c) difference between a) and b) `kirch-slice-amo1` [CR]

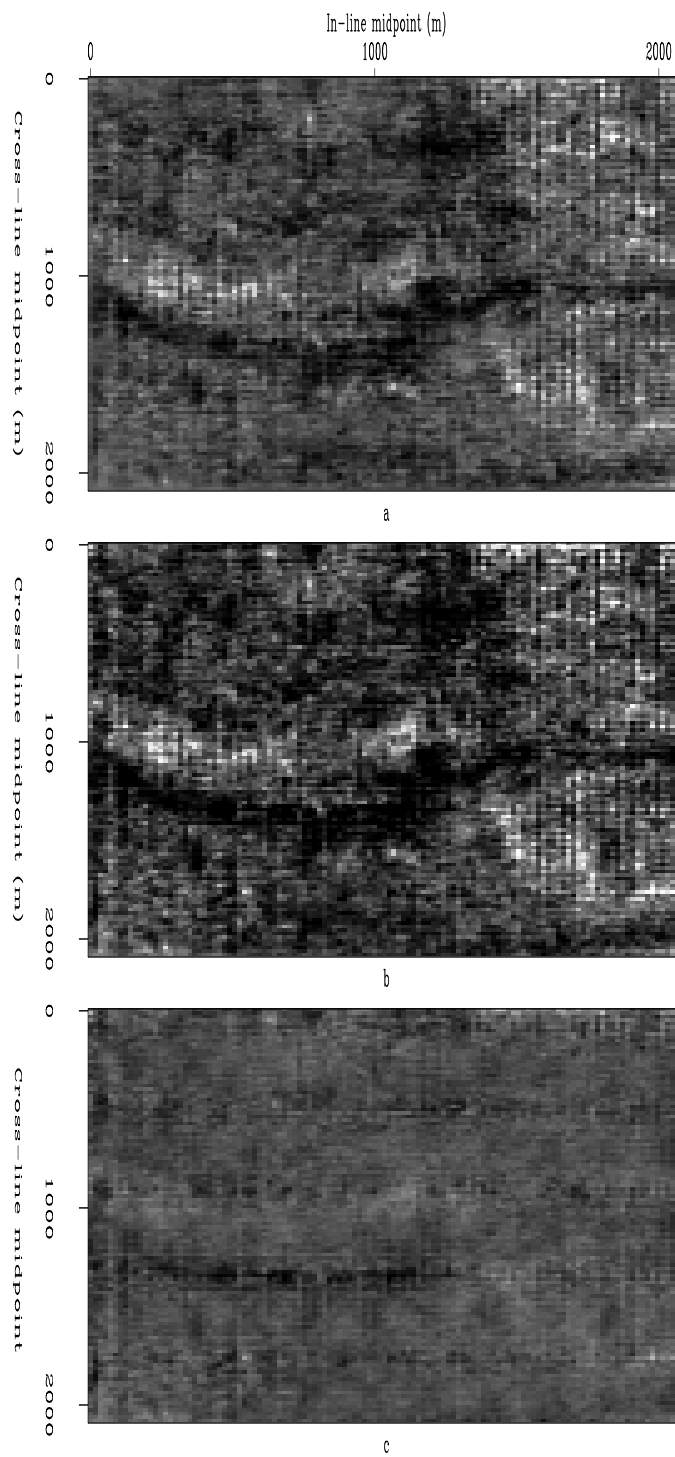


Figure 4.12: Normalizing by the AMO fold to a power of 0.5: a) un-normalized AMO, b) normalized AMO, c) difference between a) and b) `kirch-slice-amo05` [CR]

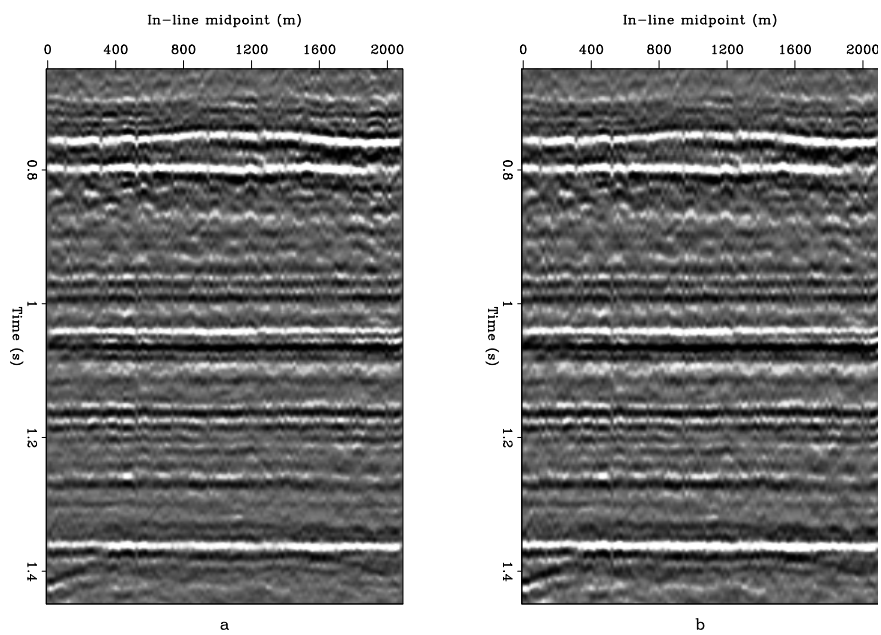


Figure 4.13: In-line section at 1.km; a) unnormalized AMO, b) normalized AMO
`kirch-amo-inline` [CR]

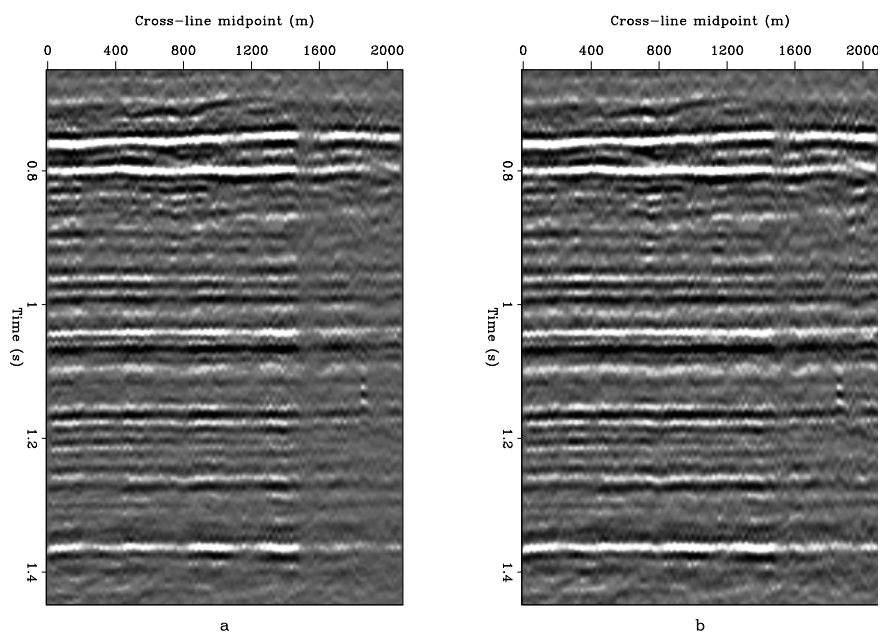


Figure 4.14: Cross-line section at 1.km; a) unnormalized AMO, b) normalized AMO
`kirch-amo-crossline` [CR]

and prestack migration. The third uses AMO to organize the data as a zero-azimuth cube with 800 meter effective offset, then applies prestack migration to the regularly sampled partial stack. The results from the different processing flows are compared to the image obtained by migrating an over-sampled subset with the same azimuth and offset ranges. To make the comparison as fair as possible to the conventional methodology of simple NMO-Stacking, the traces after NMO were laterally interpolated before they were stacked for common-offset migration. The traces were also binned at the same resolution used for AMO stacking, that is, half the nominal CMP spacing. A single depth-varying velocity function (4.16) was used for the depth migration of the subset.

Figure 4.17 compares the results of migrating the 3D subset using different imaging flows. The Figure represents a depth slice at 910 m. The migration of the oversampled survey shows the presence of a complex morphology of a meandering river system marked by ramification of the major channel. The result of migrating the NMO-stack shows a poor resolution image that makes the interpretation of the channels difficult. Applying AMO to the data preserved the sharp features of the fluvial deposit system. The result of migration after AMO is smoother than the output of migrating the irregularly sampled data. This is due to the fact that the effect of fold variations were effectively reduced by the calibration of AMO.

Given the dominantly flat geology of the survey, it was expected that migration after NMO should provide a good image. Such result can be observed on the 920m depth slice which marks the floor of the river channel 4.16. The explanation for this phenomenon is that the morphology of the river system becomes more complex towards the top of the deposition sequence. This results into diffractions from the edges of levees and from possible barrier islands. While these diffractions were preserved by AMO, they were destroyed during stacking by NMO.

CONCLUSIONS

I have presented a new technique for processing irregularly sampled wide-azimuth surveys that accurately images 3-D seismic data and preserves its relative amplitudes. The method applies AMO to regularize the data as common-azimuth (CA) and common-offset (CO) cubes. It

addresses both issues of algorithmic accuracy and proper handling of irregular geometry and therefore allows for reliable amplitude analysis on migrated data.

AMO is applied as an integral operator in the time-space domain. Its implementation as discrete summation on irregularly sampled data is improved by diagonal scaling. The diagonal transformation reduces the effects of irregular coverage at the surface and varying illumination at depth. The partial stack is normalized by a reference model that is the AMO response to an input vector with all components equal to one (flat event). The advantage of including AMO in the processing flow is threefold: (1) reduction of the size of prestack data subsets (2) interpolation to a regular grid before imaging (3) common-azimuth common-offset processing of the 3D survey.

The next chapter poses partial stacking by AMO as an optimization process to regularize the geometry of 3D surveys in presence of spatial aliasing. The limited small aperture of AMO enables inexpensive implementation of the inversion algorithm. Beyond the fold normalization, the diagonal transformation is used as a preconditioner to accelerate the convergence of the iterative solution.

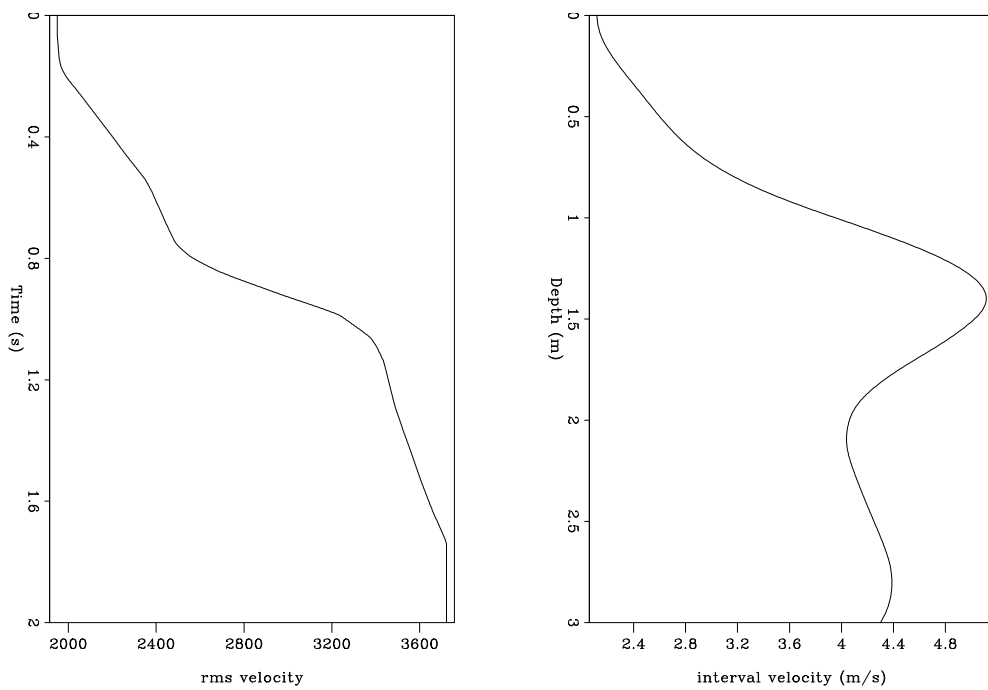


Figure 4.15: One-dimensional RMS and interval velocity functions of the survey
`kirch-velocity` [CR]

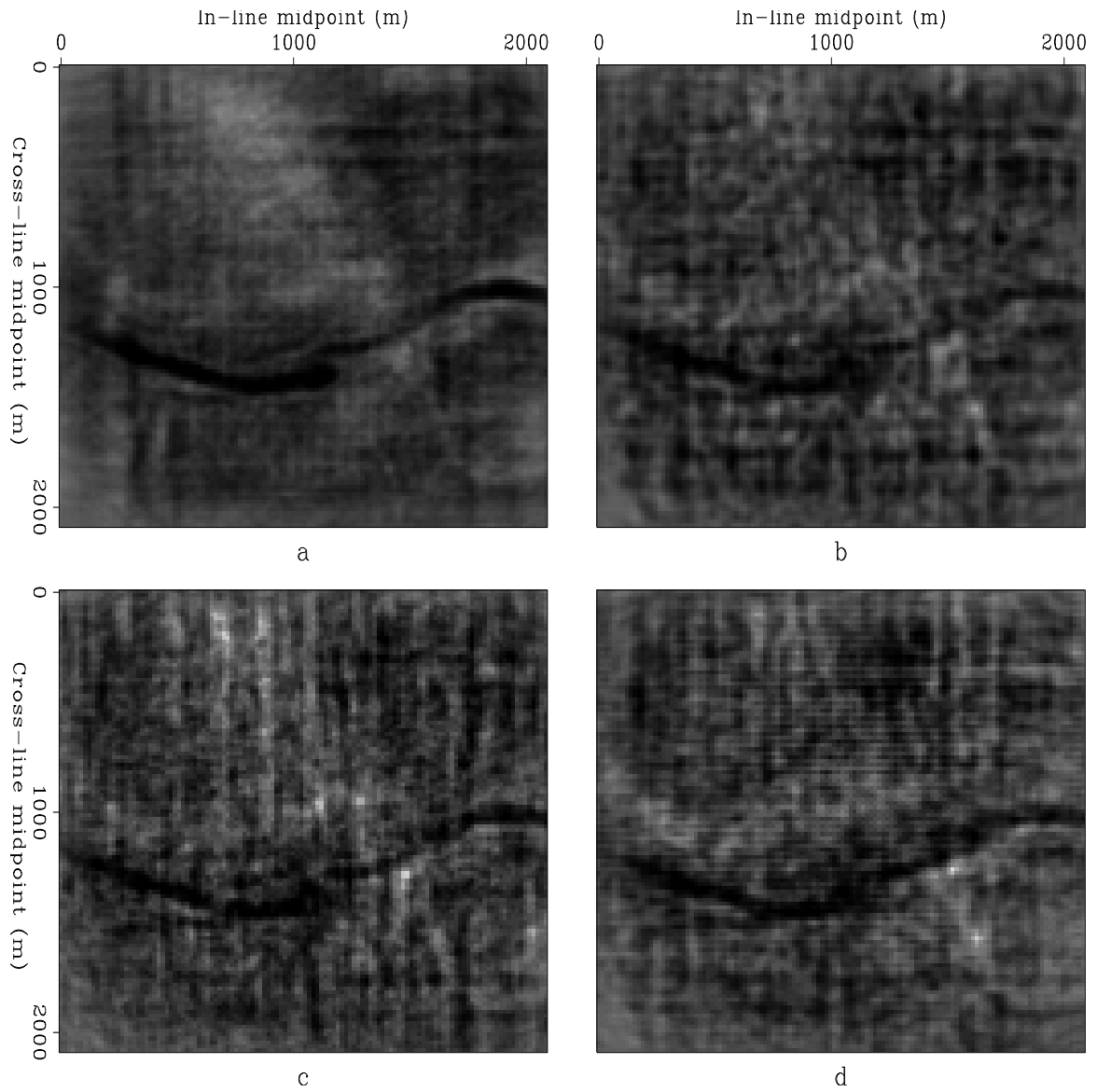


Figure 4.16: Depth slices at 920 m obtained by different imaging flows a) Migration of over-sampled subset, b) migration after AMO, c) migration of irregular subset, d) migration after binning `kirch-migration920` [CR]

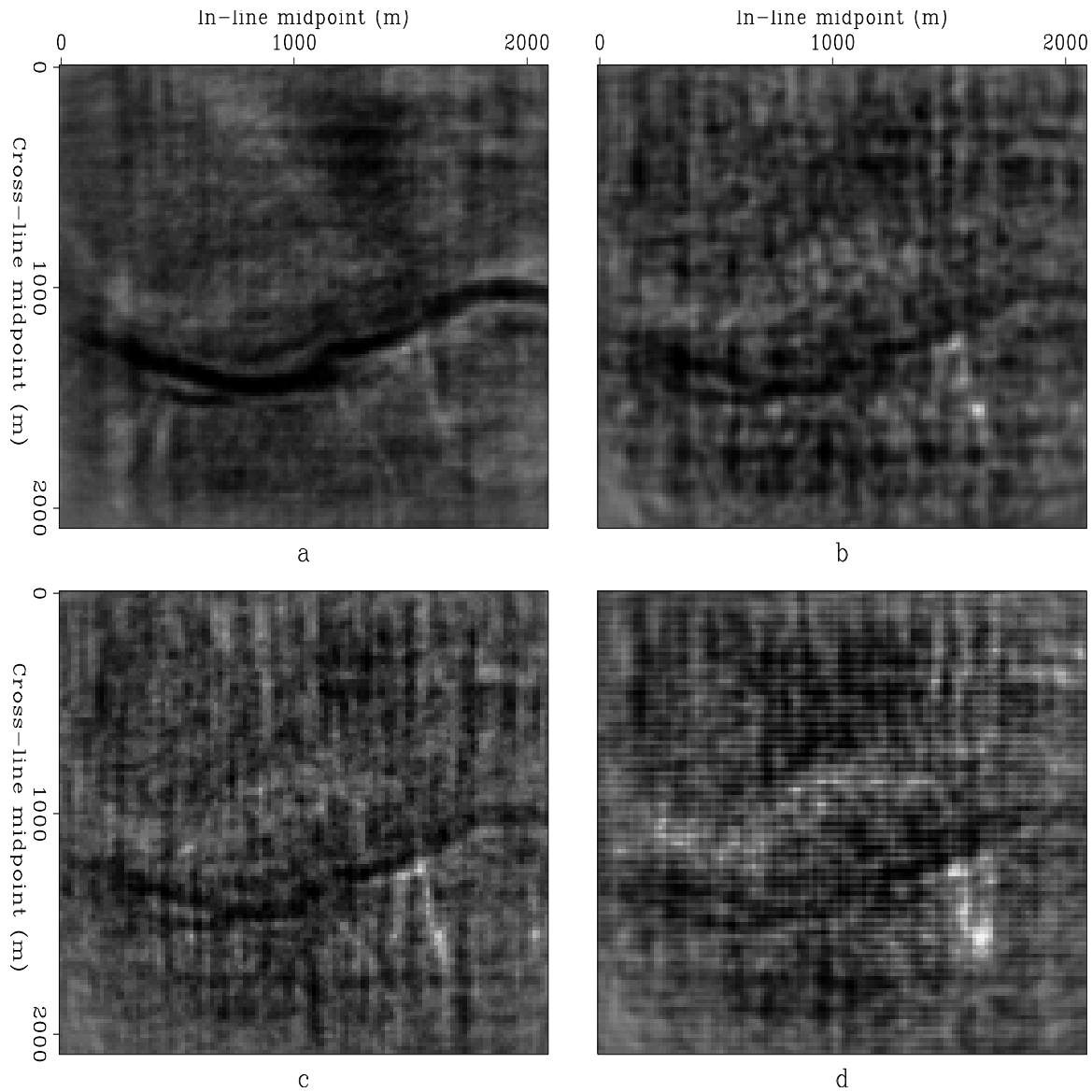


Figure 4.17: Depth slices at 910 m obtained by different imaging flows a) Migration of over-sampled subset, b) migration after AMO, c) migration of irregular subset, d) migration after binning `kirch-migration910` [CR]

Chapter 5

Inversion to common offset

OVERVIEW

In the previous chapter, I showed that in presence of adequate sampling one can use an asymptotic “true-inverse” or a properly scaled adjoint to get a useful image. Problems arise in 3D reflection seismology where, driven by economic constraints, 3D surveys typically have sparse geometry that results in spatial aliasing.

In this chapter, I introduce a new dealiasing technique named “inversion to common offset” (ICO) that takes advantage of the abundance of seismic traces in multi-fold 3D data to interpolate beyond aliasing. The matrix that relates the data to the model is the AMO operator where the model simulates a regular common-offset experiment. The technique can be viewed as a generalization of the inversion to zero offset (IZO) discussed by Ronen (1985). The main advantage of ICO, is that the modeling operator, AMO, is very compact and consequently cheaper to apply than other wave-equation processes. The new inversion also enables prestack analysis of the reflectivity function since the output models are partial stacks at non-zero offset. The partial models can be migrated separately and, either stacked together to form the final image, or, individually analyzed for amplitude and velocity variations.

I developed ICO for the application of regularizing the geometries of 3D surveys before imaging. After regularization, 3D data become handy for prestack migration using any wave

extrapolation methods including finite-differencing and wave-number domain techniques. Another promising application demonstrated in this chapter is to reduce acquisition costs by collecting seismic data with fewer offsets. Posing partial imaging as an optimization process, one would use AMO as a modeling operator to generate data with a range of azimuth and offsets, compare them to the field data, and iteratively use the differences to improve the partial image.

The first section of the chapter presents the theory and the formulation of the least-squares solution for multichannel seismic data. Since the inversion of irregularly sampled data is an ill-conditioned problem, the second section discusses two formulations for a pseudo-inverse which I refer to as data-space and model-space inverse. The third section addresses practical issues of the implementation of the inversion, mainly cost efficiency in the log-stretch Fourier domain, proper preconditioning, and regularization of the iterative solution. Finally, the last section of the chapter demonstrates the application of the inversion to reduce the costs of 3D acquisition. It illustrates an example of applying ICO to regularize the coverage of a real 3D land survey and improve the quality of the image by regularizing the data before migration.

THEORY

Posing processing as the inverse of modeling irregular data from a regularly sampled model (Ronen, 1987), the relation between data and the model can be formulated with the simple system of linear equations:

$$\mathbf{d} = \mathbf{Lm} \quad (5.1)$$

where the vector \mathbf{d} represents the irregular input data, \mathbf{m} represents a regularly sampled model and \mathbf{L} , in general, is any full or partial modeling operator.

Given the nature of multi-channel recording and the design of 3D surveys, it is expected that the number of data traces is different from the number of model traces. Most commonly, the number of observations is larger than the model parameters. One way to solve such a system of inconsistent equations is to look for a solution that minimizes the average error in the set of equations. This minimization can be done in a least-squares sense where the norm $\|\mathbf{Lm} - \mathbf{d}\|_2$ is minimized. The choice of \mathbf{m} that makes this error a minimum gives the

least-squares solution which can be expressed for the over-determined case as

$$\mathbf{m} = (\mathbf{L}^T \mathbf{L})^{-1} \mathbf{L}^T \mathbf{d} \quad (5.2)$$

for which \mathbf{m} represents a minimum length solution. When solving the under-determined problem, this solution takes a different expression:

$$\mathbf{m} = \mathbf{L}^T (\mathbf{L} \mathbf{L}^T)^{-1} \mathbf{d} \quad (5.3)$$

where \mathbf{m} is the minimum energy model that satisfies the linear equations.

These solutions define a least square inverse or pseudo-inverse for the operator \mathbf{L} . From equation (5.2), we write this inverse in terms of \mathbf{L} and its adjoint \mathbf{L}^T as:

$$\mathbf{L}_m^\dagger = (\mathbf{L}^T \mathbf{L})^{-1} \mathbf{L}^T \quad (5.4)$$

whereas in (5.3) the inverse for the under-determined problem is:

$$\mathbf{L}_d^\dagger = \mathbf{L}^T (\mathbf{L} \mathbf{L}^T)^{-1} \quad (5.5)$$

Applying the pseudo-inverse of (5.4) is equivalent to applying the adjoint operator \mathbf{L}^T followed by a spatial filtering of the model space by the inverse of $\mathbf{L}^T \mathbf{L}$. Therefore, I refer to this inverse as model-space inverse.

In equation (5.5) the adjoint operator is applied after the data have been filtered with the inverse of $\mathbf{L} \mathbf{L}^T$ and, consequently, I refer to this inverse as data-space inverse.

MULTICHANNEL INVERSION

Multichannel recording results in an abundance of seismic traces at every CMP bin, whereas the goal of imaging is to invert for a reflectivity model using the entire prestack volume. The model is regularly sampled at the nominal CMP spacing. Therefore, considering multiple

records at every CMP bin to present redundant information, the inversion for a reflectivity model from multi-offset seismic data is generally an over-determined problem. However, in many geophysical applications the size of the model space is not fixed but rather determined according to a desired resolution, computational costs and anti-aliasing criteria. Moreover, whenever gaps in seismic coverage occur, the inversion problem becomes locally under-determined. Therefore, the problem is never genuinely over-determined as often perceived. At best, the least-squares solutions for the seismic inverse problem can be distinguished by the space where the filtering is applied. Consequently for the remaining of the chapter I simply refer to the solution in equations (5.4) and (5.5) as data-space and model-space inverse.

The most important question one may ask, is when should we use one solution or the other. An important factor to take into account is the characteristics of \mathbf{LL}^T and $\mathbf{L}^T\mathbf{L}$, and in particular how difficult it is to compute their inverses. In most of the practical cases, both \mathbf{LL}^T and $\mathbf{L}^T\mathbf{L}$ are singular and care must be taken when approximating their inverse.

The data-space inverse

To estimate the data-space inverse we need to approximate an inverse for the cross product matrix LL^T . This inverse acts as a filter for the data space. Each element \mathbf{D}_{ij} of $(\mathbf{LL}^T)^{-1}$ measures the correlation between a data element \mathbf{d}_i and another data element \mathbf{d}_j . The computation of each element \mathbf{D}_{ij} requires the evaluation of an inner product in the model space. Since the model space is regularly sampled, the inner products can then be computed analytically (pending available representation of the chained operator, \mathbf{LL}^T).

Considering an irregularly sampled input of n seismic traces, the cross-product operator LL^T can be expressed in matrix notations as:

$$\mathbf{L}\mathbf{L}^T = \begin{bmatrix} \left[L_{(m,d_1)} L_{(m,d_1)}^T \right] & \left[L_{(m,d_1)} L_{(m,d_2)}^T \right] & \dots & \left[L_{(m,d_1)} L_{(m,d_n)}^T \right] \\ \left[L_{(m,d_2)} L_{(m,d_1)}^T \right] & \left[L_{(m,d_2)} L_{(m,d_2)}^T \right] & \dots & \left[L_{(m,d_2)} L_{(m,d_n)}^T \right] \\ \cdot & \cdot & \cdot & \cdot \\ \cdot & \cdot & \cdot & \cdot \\ \left[L_{(m,d_n)} L_{(m,d_1)}^T \right] & \left[L_{(m,d_n)} L_{(m,d_2)}^T \right] & \dots & \left[L_{(m,d_n)} L_{(m,d_n)}^T \right] \end{bmatrix} \quad (5.6)$$

Each inner product $\left[L_{(m,d_i)} L_{(m,d_j)}^T \right]$ is a reconstruction of a data trace with offset \mathbf{h}_i to a new trace with offset \mathbf{h}_j . Therefore the mapping is an AMO transformation, and \mathbf{D} can be written as

$$\mathbf{D} = \begin{bmatrix} I & D_{(h_1,h_2)} & D_{(h_1,h_3)} & \dots & D_{(h_1,h_n)} \\ D_{(h_2,h_1)} & I & D_{(h_2,h_3)} & \dots & D_{(h_2,h_n)} \\ D_{(h_3,h_1)} & D_{(h_3,h_2)} & I & \dots & D_{(h_3,h_n)} \\ \cdot & \cdot & \cdot & \cdot & \cdot \\ \cdot & \cdot & \cdot & \cdot & \cdot \\ \cdot & \cdot & \cdot & \cdot & \cdot \\ D_{(h_n,h_1)} & D_{(h_n,h_2)} & D_{(h_n,h_3)} & \dots & I \end{bmatrix} \quad (5.7)$$

where $\mathbf{D}_{(\mathbf{h}_i,\mathbf{h}_j)}$ is AMO from input offset \mathbf{h}_i to output offset \mathbf{h}_j and, \mathbf{I} is the identity operator (mapping from \mathbf{h}_i to \mathbf{h}_i). Conforming to the definition of AMO, $\mathbf{D}_{(\mathbf{h}_i,\mathbf{h}_j)}$ is the adjoint of $\mathbf{D}_{(\mathbf{h}_j,\mathbf{h}_i)}$; therefore, the filter \mathbf{D} is Hermitian with diagonal elements being the identity and off-diagonal elements being trace to trace AMO transforms. This is a fundamental definition of \mathbf{D} that will allow a fast and efficient numerical approximation of its inverse.

The data-space inverse can then be expressed as a two-step solution where the data is first filtered with the inverse of the operator \mathbf{D} then the adjoint is applied to the filtered data to solve for a model. The solution for \mathbf{m} from equation (5.3) can be written in terms of \mathbf{D} as:

$$\mathbf{m} = \mathbf{L}^T \mathbf{D}^{-1} \mathbf{d} \quad (5.8)$$

Now, changing the problem formulation variable \mathbf{d} to $\hat{\mathbf{d}}$, where

$$\hat{\mathbf{d}} = \mathbf{D}^{-1} \mathbf{d} \quad (5.9)$$

and recasting the problem as

$$\mathbf{m} = \mathbf{L}^T \hat{\mathbf{d}} \quad (5.10)$$

we need now to solve for $\hat{\mathbf{d}}$ by computing the inverse of \mathbf{D} from the system of equations:

$$\mathbf{d} = \mathbf{D} \hat{\mathbf{d}} \quad (5.11)$$

Once the inverse of \mathbf{D} is estimated to yield the filtered data $\hat{\mathbf{d}}$, we merely solve for the initial model $\mathbf{m} = \mathbf{L}^T \hat{\mathbf{d}}$. Notice that after filtering, we can apply any imaging operator \mathbf{L}^T to invert for \mathbf{m} .

The model-space inverse

Similarly to the data-space filter, computing the model-space inverse reduces to estimating an inverse for a cross-product matrix $\mathbf{L}^T \mathbf{L}$. This inverse acts as a filter for the model space. Each element \mathbf{M}_{ij} of $(\mathbf{L}^T \mathbf{L})^{-1}$ measures the correlation between a model element \mathbf{m}_i and another model element \mathbf{m}_j . The computation of each element \mathbf{M}_{ij} requires the evaluation of an inner product in the data space. Since that the data-space is irregularly sampled, the computation must be carried numerically.

The size of $\mathbf{L}^T \mathbf{L}$ is the square of the size of the model. Given that the adjoint operator, \mathbf{L}^T , is AMO-Stacking then the size of the model is generally much smaller than the data. This leads to a more affordable computation of $\mathbf{M} = (\mathbf{L}^T \mathbf{L})^{-1}$ compared to the costs of computing

the data-space filter.

PRACTICAL IMPLEMENTATION OF ICO

The inversion of 3D multichannel seismic data using wave-equation techniques is generally a cost prohibitive solution. The main reason for the high cost is the size of the prestack data and the time-variability of wave equation processes. The breakthrough with ICO is that the modeling operator, AMO, is very compact and therefore considerably cheaper to apply than other wave equation operators such as DMO or migration. Also, ICO is velocity independent since it is applied to normal-moveout corrected data. The iterative solution is therefore less sensitive to the velocity field such as the case for least-squares migration.

The following sections discuss several implementation tricks and robust techniques from inverse theory that enable cost effective implementation of ICO on 3D data.

Log-stretch Fourier transform

A time-space implementation of AMO as a time-variant operator is still not practical for 3D data because of its computing costs. Several authors (Bolondi et al., 1984; Biondi and Ronen, 1986; Bale and Jakubowicz, 1987; Notfors and Godfrey, 1987) have described a logarithmic stretching of the time axis that can convert a non-Fourier transform implementation to a Fourier transform combined with a phase shift.

The log-stretch transform makes AMO a time-invariant operator, which means it only depends on the difference between the input and output time. A transformation of the log-stretched data to the Fourier domain is then a convenient way to process the data in the $\Omega - X$ space. Furthermore, since each frequency inversion is completely independent, one needs to solve many small systems instead of solving one huge system of equations. The inversions can be done in parallel by as many processing units as number of frequencies. In practice, several frequency bands from a useful bandwidth of the data are carried in parallel.

Iterative solution for the pseudo-inverse

For each frequency component (or bandwidth) the systems of linear equations to be solved is still very large and one has to resort to iterative methods. This solves a huge set of simultaneous equations without the need to write down the matrix of coefficients. I use an iterative scheme based on the conjugate gradient solver, which produces a good result at a reasonable cost. Experience has shown that a satisfactory solution is achieved in less than 10 iterations. The conjugate gradient algorithm generates a sequence of approximate solutions whose computations each involve the application of the adjoint followed by the forward operator. The inner-products are essentially AMO transformations and their computation is therefore reasonably cheap.

Diagonal weighting preconditioning

The convergence rate of the conjugate gradient algorithm depends on the condition number of the matrix to be inverted. For ill-conditioned matrices a preconditioner is often necessary. The design of a good preconditioner depends directly on the structure of the matrix. In the inversion relation (5.1), the number of equations is the number of traces in the input data and the number of unknowns is the number of output traces or bins. Due to irregular sampling, the rows and columns of \mathbf{L} are badly scaled. Since \mathbf{L} is essentially a Kirchhoff-type matrix, its condition can be improved by the diagonal weighting described in the previous chapter. This implies pre- and post-multiplying the operator \mathbf{L} by a diagonal matrix whose diagonal entries are the inverse of the sum of the rows or columns of \mathbf{L} . Similar approaches for diagonal scaling are discussed in the mathematical literature using different norms of the rows and columns. They are often referred to as left and right preconditioners; I prefer to call them *data-space* and *model-space* preconditioners. The rationale in the terminology is based on the fact that the scaled adjoint is the first step of the inversion. For left preconditioning, the adjoint operator is applied after the data have been normalized by the diagonal operator. I therefore refer to this weighting as *data-space* preconditioning. Right preconditioning is equivalent to applying the adjoint operator \mathbf{L}^T followed by a scaling of the model by the diagonal operator. Consequently, I refer to this weighting as *model-space* preconditioning.

Data-space preconditioning

This is equivalent to pre-multiplying the matrix \mathbf{L} and the data vector \mathbf{d} by a diagonal matrix \mathbf{R}^{-1} and solving the system:

$$\mathbf{R}^{-1}\mathbf{d} = \mathbf{R}^{-1}\mathbf{L}\mathbf{m} \quad (5.12)$$

where the sums of the elements from each row of \mathbf{L} are along the diagonal of \mathbf{R} .

Since each row corresponds to a summation surface (impulse response of \mathbf{L}^T), then \mathbf{R}^{-1} is normalization by the coverage before AMO.

Model-space preconditioning

This approach is based on a post-multiplication of the matrix \mathbf{L} by a diagonal matrix \mathbf{C}^{-1} where the sums of the elements from each column of \mathbf{L} are along the diagonal of \mathbf{C} . The preconditioning operator introduces a new model \mathbf{x} given by

$$\mathbf{x} = \mathbf{C}\mathbf{m} \quad (5.13)$$

By the preconditioning transformation, we have recast the original inversion relation (5.1) into

$$\mathbf{d} = \mathbf{L}\mathbf{C}^{-1}\mathbf{x}. \quad (5.14)$$

After solving for \mathbf{x} we easily compute $\mathbf{m} = \mathbf{C}^{-1}\mathbf{x}$.

Given that each column of \mathbf{L} corresponds to an output bin, \mathbf{C}^{-1} is normalization by the coverage after AMO.

Data and Model preconditioning

Proper balancing of the matrix \mathbf{L} can be achieved by scaling in both data space and model space. However, applying either diagonal transformation ensures common magnitude of the

elements of \mathbf{L} . The diagonal operators \mathbf{R}^{-1} and \mathbf{C}^{-1} have physical units inverse to \mathbf{L} . Therefore applying both of them can only result into an ill-conditioned system where the matrix \mathbf{L} has the inverse of its original units.

I propose a new formulation for balancing the matrix \mathbf{L} by scaling both its rows and columns. The new formulation introduces a new parameter n , and solves the system

$$\mathbf{R}^{-n} \mathbf{d} = \mathbf{R}^{-n} \mathbf{L} \mathbf{C}^{n-1} \mathbf{x}. \quad (5.15)$$

where $0 \leq n \leq 1$.

For $n = 0$, the system (5.15) reduces to the case of column scaling, whereas for $n = 1$ it reduces to applying row scaling in the data space. As Figure 5.1 shows, the diagonal transformation has proved to be a suitable preconditioner for the linear system. A good solution was obtained after 5 to 8 iterations of conjugate gradient solver. The column scaling improved the convergence of the iterative solution and resulted into faster convergence than the row scaling. A better convergence was achieved by applying a scaling to both the data space and model space for a value of $n = 1/2$. An optimal value of n should probably depend on whether the system to be solved is mostly over-determined or under-determined. This should remain an interesting subject of investigation.

Regularization of the inversion

In order to compute stable solutions to ill-conditioned systems it is often necessary to apply regularization methods. Claerbout (1997) writes: “In geophysical fitting we generally have two goals, the first being data “fitting” and the second being the “damping” or regularization goal”. One way to achieve such objective is to augment the problem with a second regression that adds assumptions about the model (e.g. roughness, smoothness, curvature, energy in one dip, etc...).

For the data-space inverse, one now solves the problem:

$$0 \approx \mathbf{r}_d = \mathbf{A} \hat{\mathbf{d}} - \mathbf{d} \quad (5.16)$$

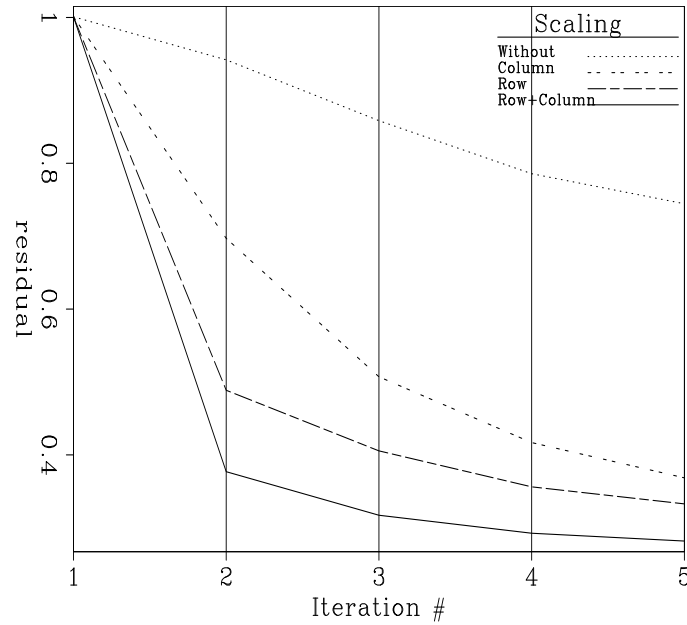


Figure 5.1: Convergence of the model-space solution for one frequency inversion using different preconditioners. `ico-residual` [NR]

$$0 \approx \mathbf{r}_{\hat{\mathbf{d}}} = \lambda \mathbf{P} \hat{\mathbf{d}}$$

The solution $\hat{\mathbf{d}}$ represents an equalized data vector that is unevenly sampled. I chose the penalty operator, \mathbf{P} , to be the identity matrix. This is the standard Tikhonov regularization where the solution $\hat{\mathbf{d}}_{\lambda}$ solves the problem:

$$\hat{\mathbf{d}}_{\lambda} = \mathbf{L}^T (\mathbf{L}\mathbf{L}^T + \lambda^2 \mathbf{I})^{-1} \mathbf{d} \quad (5.17)$$

In the solution above, \mathbf{I} is the identity operator and the damping parameter λ is an estimate of the smallest resolved singular value of \mathbf{L} .

Similar to the data-space solution, to regularize the model-space inverse one seeks a solution to the system of regressions:

$$0 \approx \mathbf{r}_d = \mathbf{L} \mathbf{m} - \mathbf{d} \quad (5.18)$$

$$0 \approx \mathbf{r}_m = \lambda \mathbf{P} \mathbf{m} \quad (5.19)$$

Since the model \mathbf{m} is regularly sampled, I chose \mathbf{P} to be the Laplacian operator, which represents differentiation in the midpoint-space. The parameter λ controls the smoothness of the solution and is again an estimate of the smallest resolved singular value of \mathbf{L} . At the time of writing the dissertation, I didn't investigate a robust strategy for estimating λ . However, by processing a single frequency (e.g the dominant frequency of the survey), I was able to iteratively guess a good estimate for λ . Ideally, one might assume a different value for λ should be used for each frequency inversion. Results showed that a single good estimate of λ produced a reasonably smooth solution while still preserving the high frequency components of the reflectivity function.

APPLICATION TO 3D REAL DATA

This section presents the results of applying ICO to the shorncliff 3D land survey presented in the last chapter. The original dataset is now further decimated to simulate a sparse geometry that results into aliasing problems. The shot lines from the over-sampled survey were spaced at 140 meters, whereas in the decimated experiment they alternate between 280 and 420m for an average spacing of 350m. I also extracted every fifth receiver line to simulate a cross-spread geometry with 350m line-spacing as shown in Figure 5.2.

The 3D subset used in the simulations consisted of 8600 traces whose source-receiver azimuth is between -60° and 60° with an absolute-offset range from 500 to 900 meters. Figure 5.4 shows the fold distribution for the subset binned at the survey's nominal CMP spacing of 35 m. The variations in coverage between different bins vary substantially from 0 to a maximum of 6. Figure 5.3 represents a fold chart for the same offset and azimuth range from the original survey. The densely-sampled subset is 13 times larger than the decimated survey.

Data regularization

To equalize the coverage of the irregularly sampled subset I applied three different regularization methods: conventional binning after NMO, partial stacking by calibrated AMO, and inversion to common offset (ICO). The model is a common offset section with zero effective

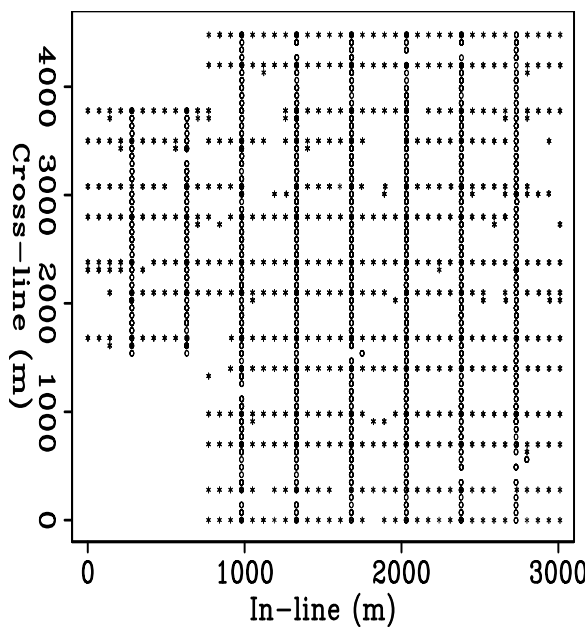


Figure 5.2: Source receiver layout for a decimated survey with cross-spread spacing of 350 m. The stars and circles indicate the source and receiver locations respectively. `ico-survey350` [CR]

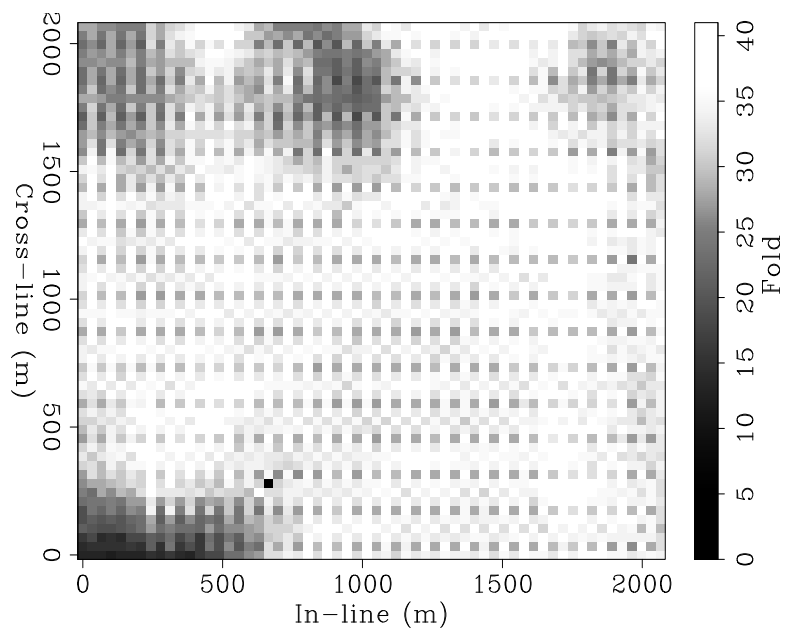


Figure 5.3: Fold distribution of the oversampled survey for the 3D subset `ico-full-fold` [CR]

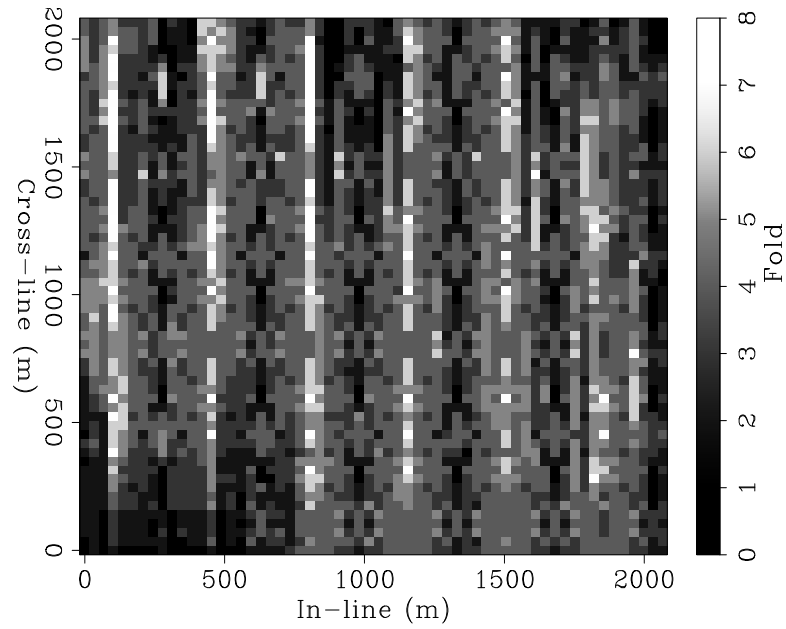


Figure 5.4: Fold distribution for the decimated subset binned at the nominal CMP spacing.
[ico-fold35](#) [CR]

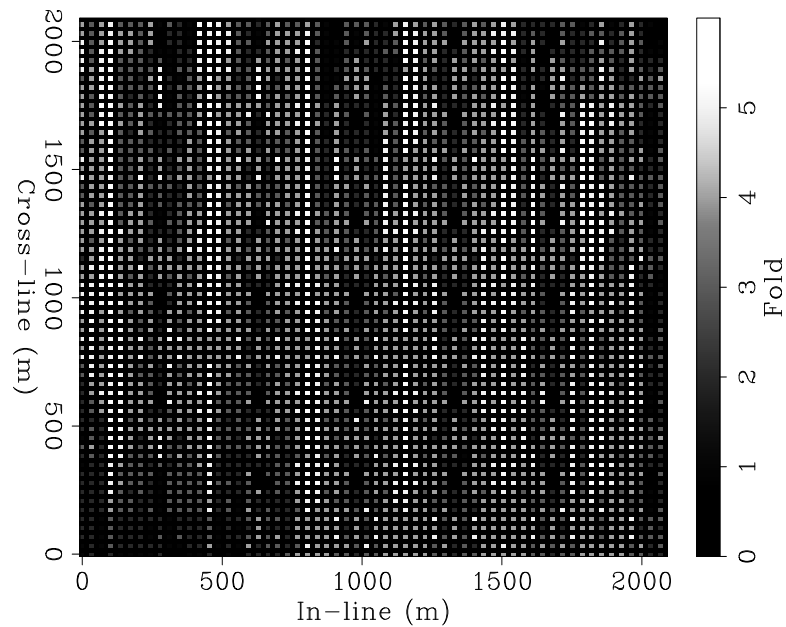


Figure 5.5: Fold distribution for the decimated subset binned at the model resolution.
[ico-fold17](#) [CR]

azimuth, 800m nominal offset and regular CMP spacing of 17.5 m. Figure 5.5 shows the fold distribution for the subset binned at the model resolution. In addition to the original areas of missing coverage, most of the bins are now empty. This is a perfect test case for ICO using both formulations for data-space and model-space inverse.

The results of regularizing the data by partial stacking using NMO, AMO, normalized AMO, data-space ICO and model-space ICO are shown in Figures 5.6-5.8. As expected, NMO nicely preserved the continuity of flat event. However, the NMO action didn't interpolate for missing gaps. Also, due to the low fold of the decimated subset and the fast varying coverage between CMP bins, the signal to noise ratio changes rapidly across the section as shown on the time slice, which displays low resolution image of the channel. With un-normalized AMO, amplitudes of flat events are very distorted and aliasing noise dominates the seismic sections along the in-line and cross-line axes. The time slice shows strong acquisition footprint where the high and low amplitude anomalies are purely fold related. AMO normalization significantly improved the results. The amplitudes along the flat events are better handled as shown on the time slice. However, there is a travel-time error in the filled gaps and aliasing artifacts remain in the sections. The results of regularized ICO with row and column scaling, after 8 iterations, are better than the normalized AMO result. Amplitudes along the flat reflectors are better equalized and aliasing related noise is largely reduced. The result of model-space ICO is better than the data-space result because of better regularization of the model-space solution. A good regularizing operator that can be applied to an irregularly sampled model should improve the quality of the data-space solution.

Migration after regularization

The next step after regularizing the coverage of the 3D subset is to apply 3D migration to the partial stack. Although at this stage any wave-extrapolation technique can be applied to the regularly sampled subset, I chose Kirchhoff migration for consistency in comparing the results of imaging before and after regularization.

Figure 5.10 compares the results of migrating the 3D subset using different imaging flows. The Figure represents a depth slice (910 m) where differences are most noticeable between

the results. The migration of the oversampled survey indicates a complex morphology of a meandering river system marked by ramification of the major channel. The output of migrating the irregularly sampled subset is very noisy and distorted by strong artifacts that make the interpretation of the channels difficult. The result of migrating the NMO-stack is smoother but displays poor resolution and the channels are also unresolved. Applying AMO to the sparsely sampled data produced aliasing noise in the partial stack and therefore degraded the quality of the migration. The result of migration after data-space ICO also failed to produce a good image of the river channel. In contrast, migration after regularization with model-space ICO unveiled much of the details in the image and resolved the different branches of the channel. Given the dominantly flat geology of the survey, it was expected that migration after NMO should provide a good image. Such result can be observed on the 920m depth slice which marks the floor of the river channel 5.9. A plausible explanation for this phenomenon is that the morphology of the river system becomes more complex towards the top of the deposition sequence. This results into diffractions from the edges of levees and from possible barrier islands. While these diffractions were nicely preserved by ICO, they were destroyed during stacking by NMO.

CONCLUSIONS

I have presented a new approach for imaging irregularly sampled 3D prestack data. The method poses partial stacking with AMO as an optimization process to reduce the size of prestack data and regularize its coverage before migration. The new inversion, named ICO is applied to normal-moveout corrected data. It enables prestack analysis of the reflectivity function since the output models are partial stacks at non-zero offset. The partial stacks can be migrated separately and, either stacked together to form the final image, or, individually analyzed for amplitude and velocity variations.

I have presented a cost effective implementation of ICO in the Log-stretch Fourier domain with proper preconditioning and regularization of the inversion for iterative solvers. Results of applying ICO to a land 3D survey showed that regularizing the coverage before imaging

helps preserve the amplitude information and the high frequency components of the reflectivity function. Furthermore, ICO provides a promising approach for reducing the costs of 3D acquisition.

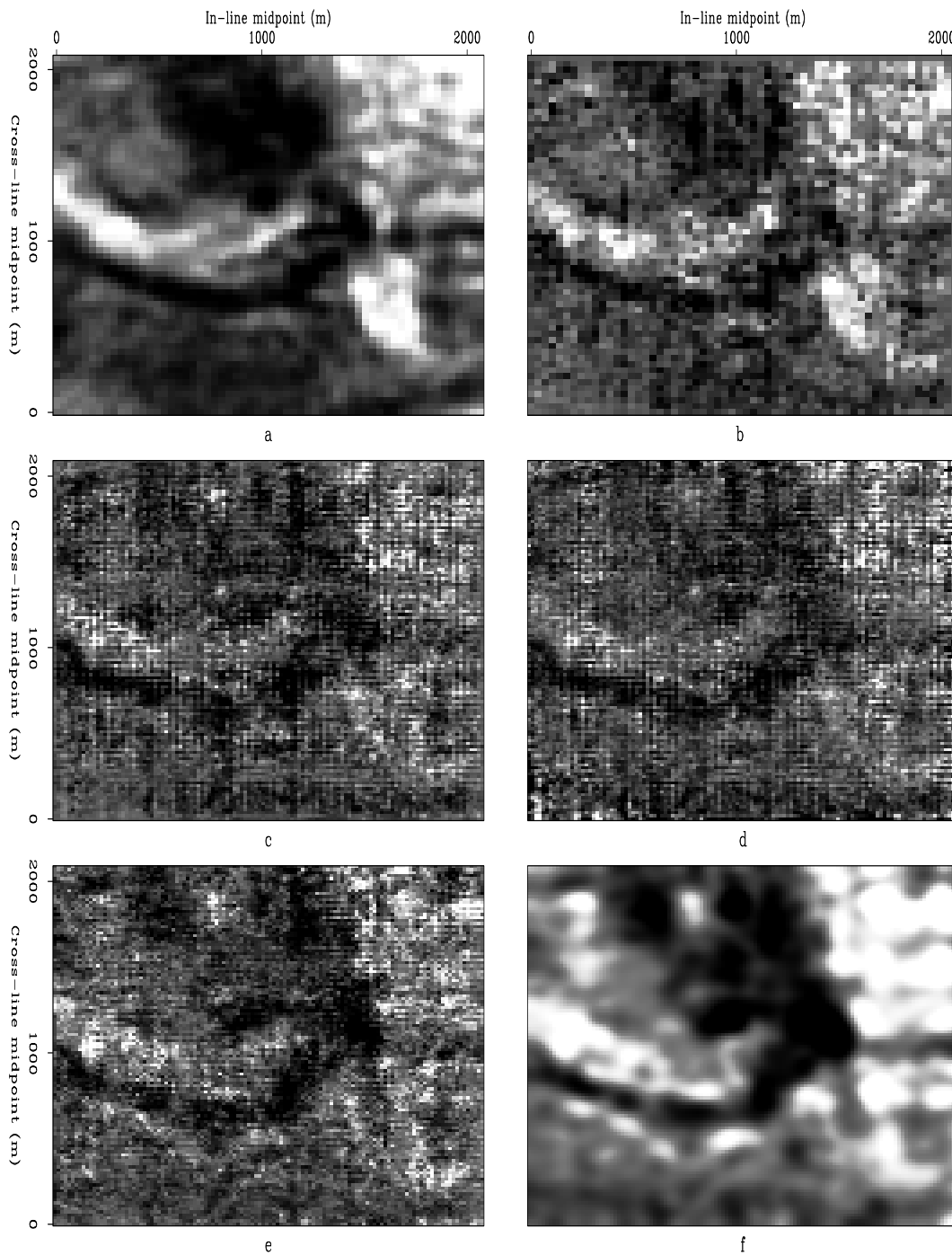


Figure 5.6: Time slices (0.71 s) obtained by: a) NMO-Stack of over-sampled subset, b) NMO-Stack of decimated subset, c) Un-normlized AMO-Stack, d) Normalized AMO-Stack, e) ICO partial stack using the data-space inverse, f) ICO partial stack using the model-space inverse. `ico-time-slice` [CR]

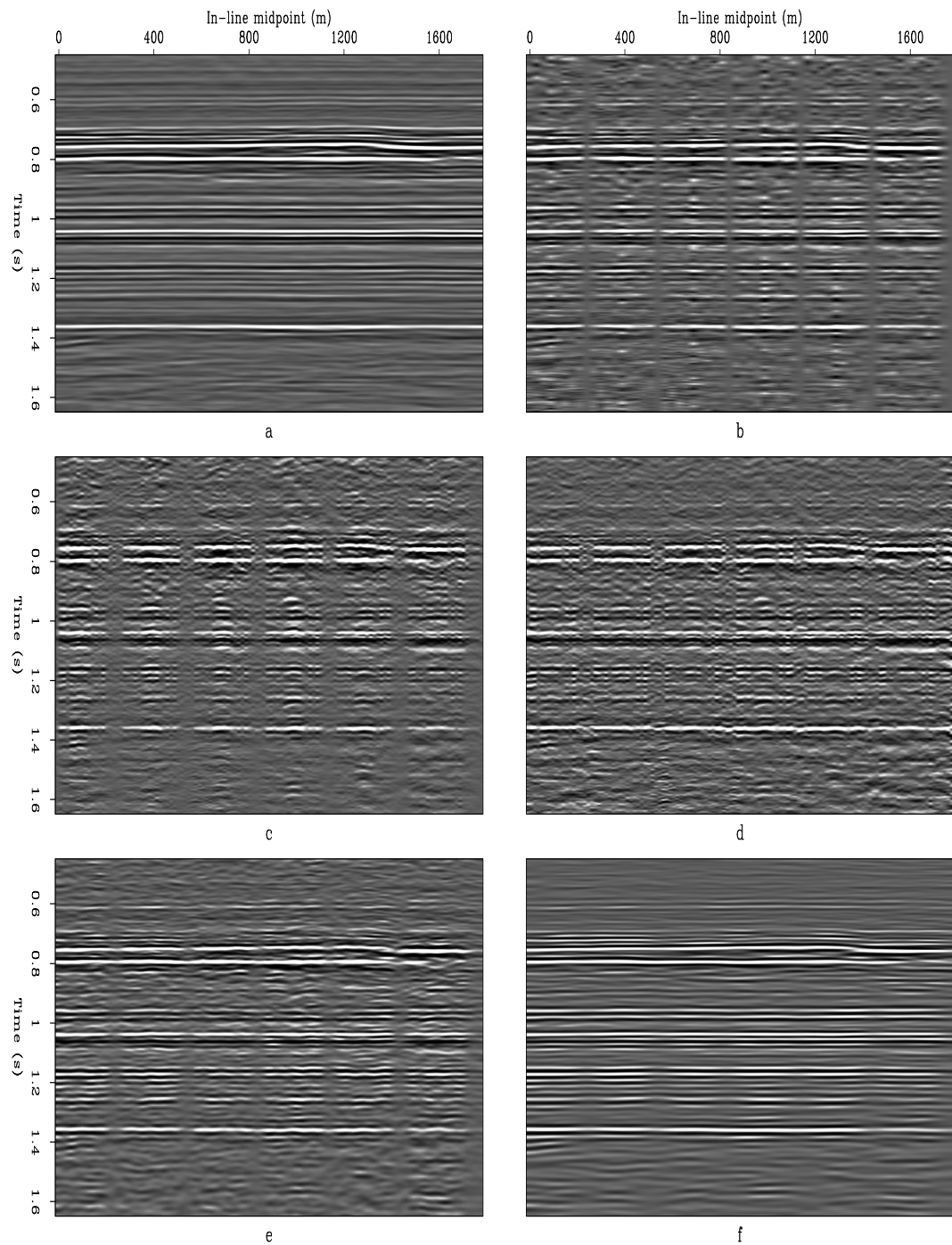


Figure 5.7: In-line sections at 1 km obtained by: a) NMO-Stack of over-sampled subset, b) NMO-Stack of decimated subset, c) Un-normlized AMO-Stack, d) Normalized AMO-Stack, e) ICO partial stack using the data-space inverse, f) ICO partial stack using the model-space inverse. `ico-comp-inline` [CR]

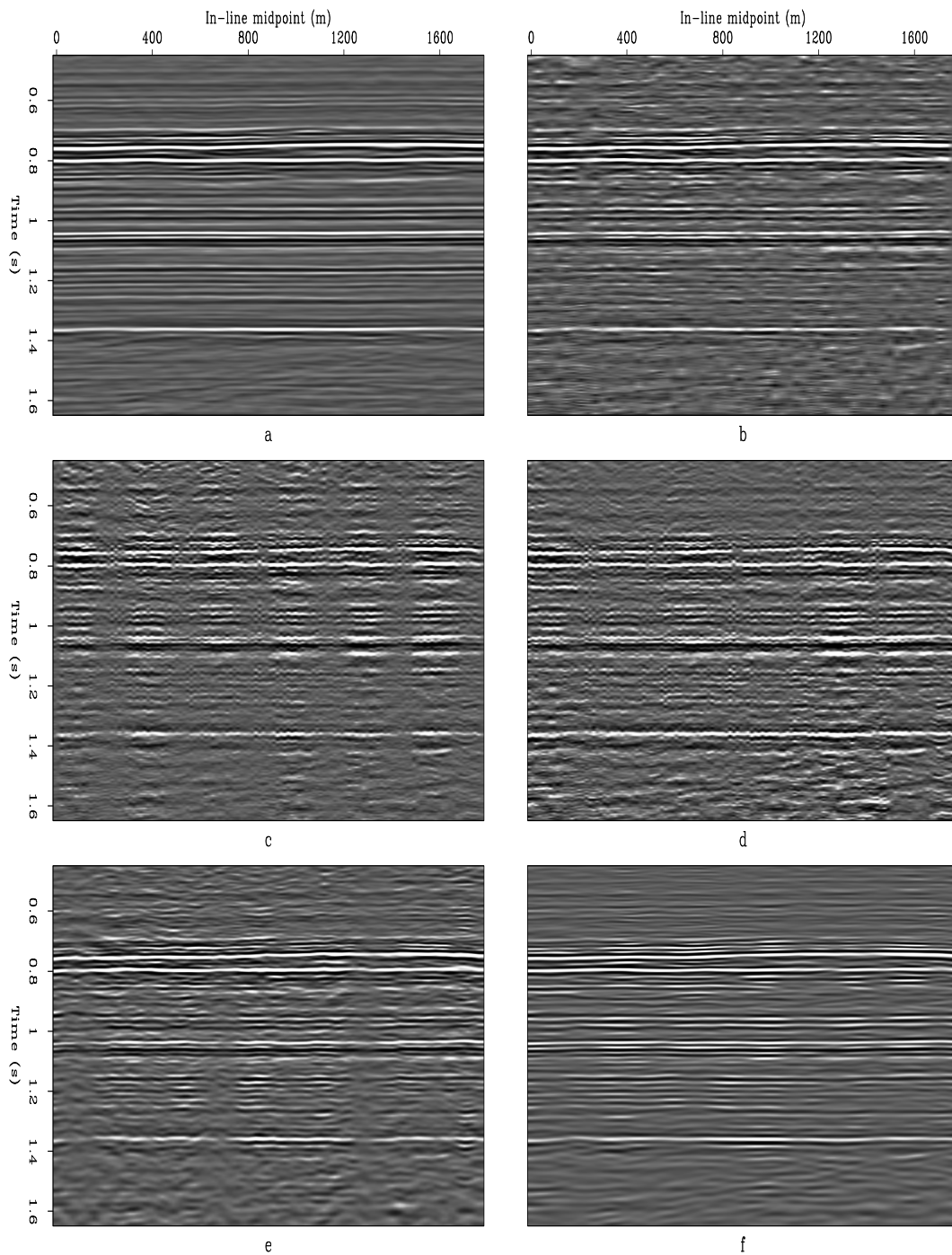


Figure 5.8: Cross-line sections at 1 km obtained by: a) NMO-Stack of over-sampled subset, b) NMO-Stack of decimated subset, c) Un-normlized AMO-Stack, d) Normalized AMO-Stack, e) ICO partial stack using the data-space inverse, f) ICO partial stack using the model-space inverse. `ico-comp-crossline` [CR]

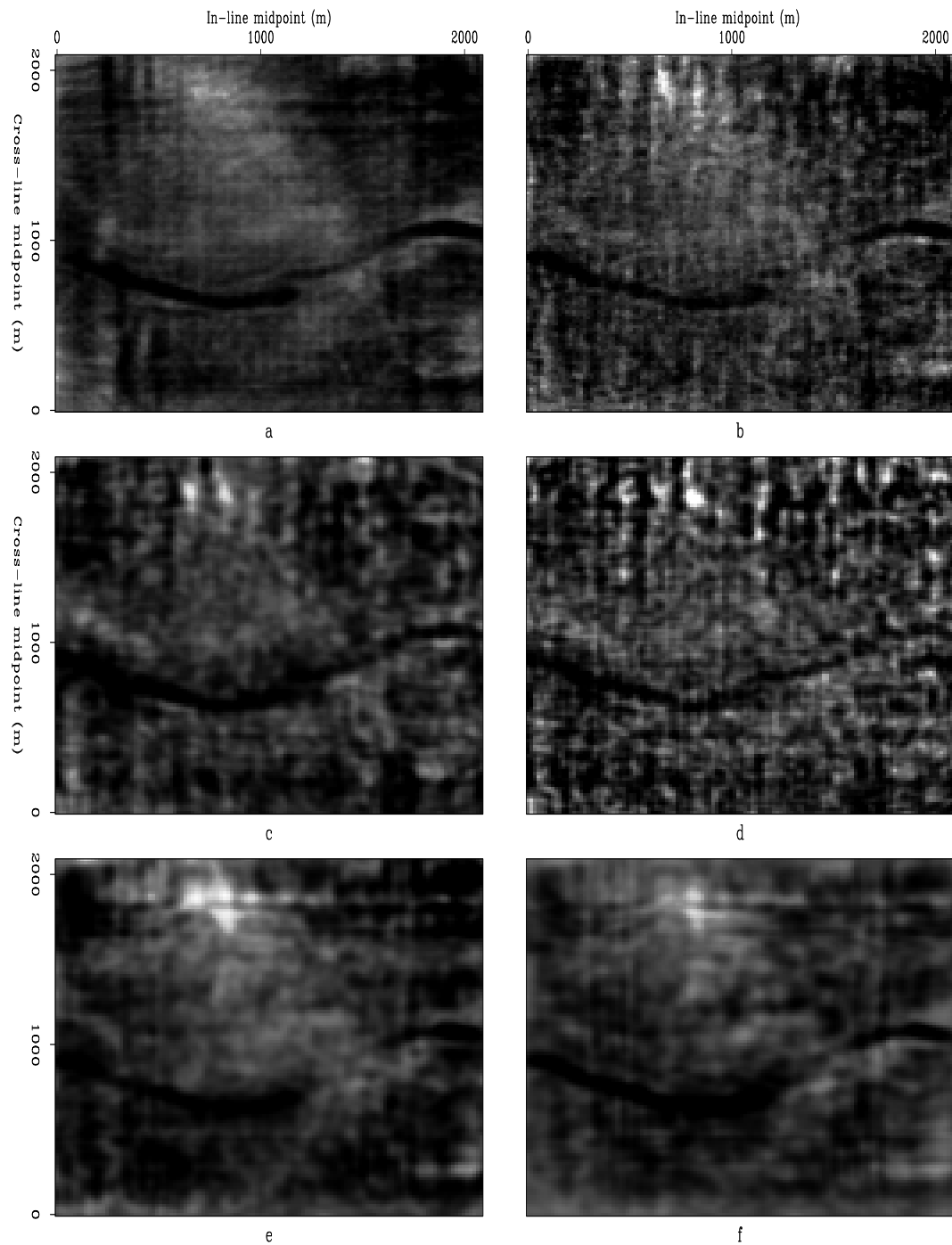


Figure 5.9: Depth slices at 920 m obtained by different imaging flows a) Migration of over-sampled subset, b) Migration of decimated subset, c) Migration after binning, d) Migration after normalized AMO, e) Migration after ICO using data-space inverse `ico-mig920` [CR]

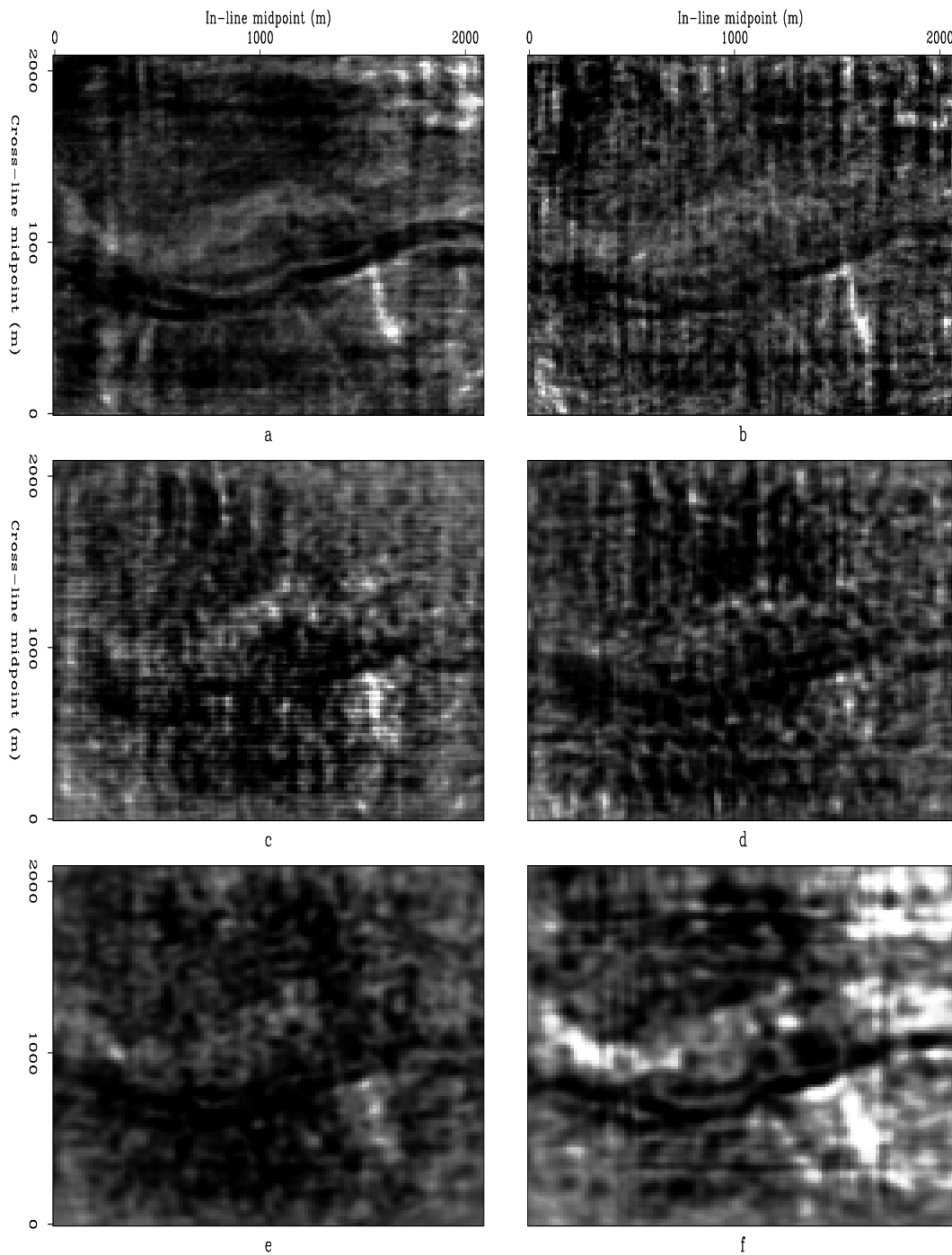


Figure 5.10: Depth slices at 910 m obtained by different imaging flows a) Migration of over-sampled subset, b) Migration of decimated subset, c) Migration after binning, d) Migration after normalized AMO, e) Migration after ICO using data-space inverse, f) Migration after ICO using model-space inverse `ico-mig910` [CR]

Appendix A

Derivation of integral AMO

The derivation of the AMO operator starts from the Fourier-domain formulation of DMO (Hale, 1984) and “inverse” DMO (Ronen, 1987; Liner, 1990). However, because 3D prestack data is often irregularly sampled, AMO is applied as an integral operator in the time-space domain. The transformation is thoroughly defined in the midpoint-offset domain by the kinematics, the amplitude weights and the spatial extent (aperture) of the AMO impulse response.

AMO IMPULSE RESPONSE

To derive a time-space representation of the AMO impulse response from its frequency-wavenumber representation, we evaluate the stationary-phase approximation of the inverse Fourier transform along the midpoint coordinates.

The DMO operator and its inverse, DMO^{-1} , can be defined in the zero-offset frequency ω_0 and the midpoint wavenumber \mathbf{k} as

$$DMO = \int dt_1 J_1 e^{-i\omega_0 t_1 \sqrt{1 + \left(\frac{\mathbf{k} \cdot \mathbf{h}_1}{\omega_0 t_1}\right)^2}} \quad (\text{A.1})$$

$$DMO^{-1} = \int d\omega_o J_2 e^{+i\omega_o t_2 \sqrt{1 + \left(\frac{\mathbf{k} \cdot \mathbf{h}_2}{\omega_o t_2}\right)^2}}. \quad (\text{A.2})$$

The *AMO* operator is given by the cascades of *DMO* and DMO^{-1} and its impulse response can be written as,

$$AMO = \frac{1}{4\pi^2} \int d\mathbf{k} e^{-i\mathbf{k}\cdot\mathbf{m}} \int dt_1 \int d\omega_o J_1 J_2 e^{-i\omega_o \left(t_1 \sqrt{1 + \left(\frac{\mathbf{k}\cdot\mathbf{h}_1}{\omega_o t_1} \right)^2} - t_2 \sqrt{1 + \left(\frac{\mathbf{k}\cdot\mathbf{h}_2}{\omega_o t_2} \right)^2} \right)}. \quad (\text{A.3})$$

The derivation of the stationary-phase approximation of the integral in $d\mathbf{k}$ is similar to the one presented in (Black et al., 1993b) for deriving a time-space formulation for the conventional DMO impulse response. We begin by changing the order of the integrals and rewriting (A.3) as

$$AMO = \frac{1}{4\pi^2} \int dt_1 \int d\omega_o \int d\mathbf{k} J_1 J_2 e^{i[\omega_o(t_1\eta_1 - t_2\eta_2) - \mathbf{k}\cdot\Delta\mathbf{m}]}. \quad (\text{A.4})$$

The phase of this integral is,

$$\Phi \equiv \omega_o(t_1\eta_1 - t_2\eta_2) - \mathbf{k}\cdot\Delta\mathbf{m}, \quad (\text{A.5})$$

where,

$$\eta_1 = \sqrt{1 + \left(\frac{\mathbf{k}\cdot\mathbf{h}_1}{\omega_o t_1} \right)^2} \quad \text{and} \quad \eta_2 = \sqrt{1 + \left(\frac{\mathbf{k}\cdot\mathbf{h}_2}{\omega_o t_2} \right)^2}. \quad (\text{A.6})$$

Next we make the following change of variables and let

$$\beta_1 = \frac{\mathbf{h}_1\cdot\mathbf{k}}{\omega_o t_1} \quad \text{and} \quad \beta_2 = \frac{\mathbf{h}_2\cdot\mathbf{k}}{\omega_o t_2}. \quad (\text{A.7})$$

Therefore, η_1 and η_2 become

$$\eta_1 = \sqrt{1 + \beta_1^2} \quad \text{and} \quad \eta_2 = \sqrt{1 + \beta_2^2}. \quad (\text{A.8})$$

The derivatives of η_1 and η_2 with respect to the in-line component of the wavenumber k_x and

the cross-line component k_y can be written as

$$\begin{aligned} \frac{\partial \eta_1}{\partial k_x} &= \frac{h_{1x}}{\omega_o t_1} \frac{\beta_1}{\sqrt{1 + \beta_1^2}} & \text{and} & & \frac{\partial \eta_2}{\partial k_x} &= \frac{h_{2x}}{\omega_o t_1} \frac{\beta_2}{\sqrt{1 + \beta_2^2}} \\ \frac{\partial \eta_1}{\partial k_y} &= \frac{h_{1y}}{\omega_o t_1} \frac{\beta_1}{\sqrt{1 + \beta_1^2}} & \text{and} & & \frac{\partial \eta_2}{\partial k_y} &= \frac{h_{2y}}{\omega_o t_1} \frac{\beta_2}{\sqrt{1 + \beta_2^2}}. \end{aligned} \quad (\text{A.9})$$

Making one more change of variables, we let

$$v_1 = \frac{\beta_1}{\sqrt{1 + \beta_1^2}} \quad \text{and} \quad v_2 = \frac{\beta_2}{\sqrt{1 + \beta_2^2}}. \quad (\text{A.10})$$

Setting the derivative of the phase Φ to zero yields the system of equations:

$$\begin{cases} h_{1x} v_1 - h_{2x} v_2 = \Delta m_x \\ h_{1y} v_1 - h_{2y} v_2 = \Delta m_y \end{cases} \quad (\text{A.11})$$

which we solve for v_1 and v_2 (i.e., η_1 and η_2) at the stationary path \mathbf{k}_0 . The determinant of the system is given by

$$\Delta = h_{2x} h_{1y} - h_{1x} h_{2y} = h_1 h_2 \sin \Delta \theta, \quad (\text{A.12})$$

and the solutions for v_1 and v_2 are

$$v_{01} = \frac{\Delta m \sin(\theta_2 - \Delta \varphi)}{h_1 \sin \Delta \theta}, \quad (\text{A.13})$$

and

$$v_{02} = \frac{\Delta m \sin(\theta_1 - \Delta \varphi)}{h_2 \sin \Delta \theta}. \quad (\text{A.14})$$

Now we need to evaluate the phase function Φ along the stationary path \mathbf{k}_0 . By respectively multiplying the equations in (A.11) by k_{0x} and k_{0y} and summing them together we obtain,

$$\mathbf{k}_0 \cdot \Delta \mathbf{m} = \frac{\omega_o t_1 \beta_{01}^2}{\sqrt{1 + \beta_{01}^2}} - \frac{\omega_o t_2 \beta_{02}^2}{\sqrt{1 + \beta_{02}^2}}. \quad (\text{A.15})$$

Substituting this relationship into the expression of the phase function [equation (A.5)] we

obtain

$$\Phi_0 = \omega_o \left(\frac{t_1}{\sqrt{1 + \beta_{01}^2}} - \frac{t_2}{\sqrt{1 + \beta_{02}^2}} \right) = \omega_o \left(\frac{t_1}{\eta_{01}} - \frac{t_2}{\eta_{02}} \right). \quad (\text{A.16})$$

The phase function along the stationary path is thus peaked for

$$t_2 = t_1 \frac{\eta_{02}}{\eta_{01}} = t_1 \frac{\sqrt{1 - v_{01}^2}}{\sqrt{1 - v_{02}^2}} \quad (\text{A.17})$$

Substituting equations (A.13) and (A.14) into (A.17) we obtain (2.1) of the main text:

$$t_2 = t_1 \frac{h_2}{h_1} \sqrt{\frac{h_1^2 \sin^2 \Delta\theta - \Delta m^2 \sin^2(\theta_2 - \Delta\varphi)}{h_2^2 \sin^2 \Delta\theta - \Delta m^2 \sin^2(\theta_1 - \Delta\varphi)}}. \quad (\text{A.18})$$

AMO AMPLITUDES

To derive an expression for the amplitudes of the AMO impulse response, we start from the general expression for the stationary-phase approximation of the \mathbf{k} integral in equation (A.3) as in (Bleistein and Handelsman, 1975),

$$A \approx \frac{2\pi J_1 J_2}{|\det(\mathfrak{C})|^{1/2}} e^{i\Phi + \text{sig}(\mathfrak{C})\frac{\pi}{4}}. \quad (\text{A.19})$$

Therefore we need to evaluate the determinant and the signature of the curvature matrix \mathfrak{C} , which is defined as

$$\mathfrak{C} = \begin{vmatrix} \frac{\partial^2 \Phi}{\partial k_x^2} & \frac{\partial^2 \Phi}{\partial k_x \partial k_y} \\ \frac{\partial^2 \Phi}{\partial k_x \partial k_y} & \frac{\partial^2 \Phi}{\partial k_y^2} \end{vmatrix}. \quad (\text{A.20})$$

Taking the second-order partial derivatives of Φ with respect to k_x and k_y and using the definitions of β_1 and β_2 yields the following expressions for $\frac{\partial^2 \Phi}{\partial k_x^2}$, $\frac{\partial^2 \Phi}{\partial k_y^2}$ and $\frac{\partial^2 \Phi}{\partial k_x \partial k_y}$:

$$\frac{\partial^2 \Phi}{\partial k_x^2} = \frac{h_{1x}^2}{\omega_o t_1} (1 - v_{01}^2)^{3/2} - \frac{h_{2x}^2}{\omega_o t_2} (1 - v_{02}^2)^{3/2} \quad (\text{A.21})$$

$$\frac{\partial^2 \Phi}{\partial k_y^2} = \frac{h_{1y}^2}{\omega_o t_1} (1 - v_{01}^2)^{3/2} - \frac{h_{2y}^2}{\omega_o t_2} (1 - v_{02}^2)^{3/2} \quad (\text{A.22})$$

$$\frac{\partial^2 \Phi}{\partial k_x \partial k_y} = \frac{h_{1x} h_{1y}}{\omega_o t_1} (1 - v_{01}^2)^{3/2} - \frac{h_{2x} h_{2y}}{\omega_o t_2} (1 - v_{02}^2)^{3/2}. \quad (\text{A.23})$$

With a little algebra, one may verify that the determinant of the curvature matrix is

$$\begin{aligned} \det(C) &= -\frac{\Delta^2}{|\omega_o|^2 t_1 t_2} (1 - v_{01}^2)^{3/2} (1 - v_{02}^2)^{3/2} \\ &= -\frac{\Delta^2}{|\omega_o|^2 t_0^2} (1 - v_{01}^2)^2 (1 - v_{02}^2)^2. \end{aligned} \quad (\text{A.24})$$

Notice that the determinant of \mathfrak{C} , which is the product of the two eigenvalues of \mathfrak{C} , is always negative. This means the two eigenvalues have opposite signs and consequently the signature of \mathfrak{C} , defined as the number of positive eigenvalues minus the number of negative eigenvalues, is always null. Therefore, the second term of the phase shift in equation (A.19) vanishes.

To obtain expressions for the AMO amplitude, we need to substitute equation (A.24) in equation (A.19), together with the corresponding expressions for J_1 and J_2 . Given a forward DMO with a Jacobian term J_1 , I showed in Chapter 3 of the main text that an asymptotic inverse provides a better representation for the inverse DMO operator than the approximate adjoint. Also, by restricting the definition of “true-amplitude” to preserving the peak amplitude of reflection events, I also showed that an amplitude-preserving function for AMO can be defined by cascading Zhang and Black (1988) DMO with its asymptotic “true-inverse”; therefore given

$$J_1 = \frac{(1 + v_{01}^2)}{\sqrt{1 - v_{01}^2}}, \quad J_2 = 1. \quad (\text{A.25})$$

after taking into account the Jacobian of the transformation from t_1 to t_0 ($dt_1 = dt_0 \sqrt{1 - v_{01}^2}$) in the first integral of equation (A.4), we can write the amplitude term for the AMO integral:

$$A \approx \frac{|\omega_o| t_0}{2\pi \Delta} \frac{(1 + v_{01}^2)}{(1 - v_{01}^2)(1 - v_{02}^2)} \quad (\text{A.26})$$

$$= \frac{|\omega_2| t_2}{2\pi \Delta} \frac{(1 + v_{01}^2)}{(1 - v_{01}^2)(1 - v_{02}^2)}. \quad (\text{A.27})$$

The last substitution, $|\omega_o| t_0 = |\omega_2| t_2$, enables us to apply the differentiation operator $|\omega_2|$ to the output data; it is correct because t_0 and t_2 are linked by the linear relationship $t_0 = t_2 \sqrt{1 - v_{02}^2}$.

The expression for the amplitudes presented in equation (2.4) of the main text follows by simple substitution of the expressions for Δ , v_{01} , and v_{02} , from equations (A.12), (A.13) and (A.14) into equation (A.27).

AMO APERTURE

Cascading DMO and inverse DMO allowed us to evaluate the summation path of AMO and the corresponding weighting function. However, this procedure is not sufficient for evaluating the third major component of the integral operator, that is, its aperture (range of integration). To solve this problem, Fomel and Biondi (1995c) applied an alternative approach by defining AMO as the cascade of 3D common-offset common-azimuth migration and 3D modeling at a different azimuth and offset. I briefly discuss their derivations in this appendix as part of a complete definition of integral AMO.

The impulse response of the common-offset common-azimuth migration is a symmetric ellipsoid with the center in the input midpoint and axis of symmetry along the input-offset direction. Such an ellipsoid is described by the general formula

$$z(\mathbf{m}) = \sqrt{R^2 - \Delta m^2 + \gamma \frac{(\Delta \mathbf{m} \cdot \mathbf{h}_1)^2}{h_1^2}}, \quad (\text{A.28})$$

where z stands for the depth coordinate, \mathbf{m} is the surface coordinate, $\Delta \mathbf{m} = \mathbf{m} - \mathbf{m}_1$, R is the small semi-axis of the ellipsoid, and γ is a nondimensional parameter describing the stretching of the ellipse ($\gamma < 1$). Deregowski and Rocca (1981) derived the following connections between the geometric properties of the reflector and the coordinates of the corresponding

impulse in the data:

$$R = \frac{v t_1}{2} ; \gamma = \frac{\frac{4h_1^2}{v^2}}{t_1^2 + \frac{4h_1^2}{v^2}}, \quad (\text{A.29})$$

where v is the propagation velocity.

The impulse response of the AMO operator corresponds kinematically to the reflections from the ellipsoid defined by equation (A.28) to a different azimuth and different offset. To constrain the AMO aperture, Fomel and Biondi (1995c) based their derivations on answering the following question: *For a given elliptic reflector defined by the input midpoint, offset, and time coordinates, what points on the surface can form a source-receiver pair valid for a reflection?* If a point in the output midpoint-offset space cannot be related to a reflection pattern, it should be excluded from the AMO aperture.

Fermat's principle provides a general method of solving the kinematic reflection problem (Goldin, 1986). The formal expression for the two-point reflection traveltime is given by

$$t_2 = \frac{\sqrt{(\mathbf{s}_2 - \mathbf{m})^2 + z^2(\mathbf{m})}}{v} + \frac{\sqrt{(\mathbf{r}_2 - \mathbf{m})^2 + z^2(\mathbf{m})}}{v}, \quad (\text{A.30})$$

where \mathbf{m} is the vertical projection of the reflection point to the surface, \mathbf{s}_2 is the source location, and \mathbf{r}_2 is the receiver location for the output trace. According to Fermat's principle, the reflection raypath between two fixed points must correspond to the extremum value of the traveltime. Hence, in the vicinity of a reflected ray,

$$\frac{\partial t_2}{\partial \mathbf{m}} = 0. \quad (\text{A.31})$$

Solving equation (A.31) for \mathbf{m} allows us to find the reflection raypath for a given source-receiver pair on the surface.

To find the solution of (A.31), it is convenient to decompose the reflection-point projection \mathbf{m} into three components: $\mathbf{m} = \mathbf{m}_1 + \mathbf{m}_\parallel + \mathbf{m}_\perp$, where \mathbf{m}_\parallel is parallel to the input offset vector \mathbf{h}_1 , and \mathbf{m}_\perp is perpendicular to \mathbf{h}_1 . The plane, drawn through the reflection point and the central line of ellipsoid (A.28), must contain the zero-offset (normally reflected) ray because of the cylindrical symmetry of the reflector. The fact that the zero-offset ray is normal to the

reflector gives us the following connection between the zero-offset midpoint \mathbf{m}_0 and the \mathbf{m}_{\parallel} component of the reflection point \mathbf{m} :

$$\mathbf{m}_0 = (\mathbf{m}_1 + \mathbf{m}_{\parallel}) + z (\mathbf{m}_1 + \mathbf{m}_{\parallel}) \frac{\partial z}{\partial (\mathbf{m}_1 + \mathbf{m}_{\parallel})} = \mathbf{m}_1 + \gamma \mathbf{m}_{\parallel}. \quad (\text{A.32})$$

Equation (A.32) evaluates \mathbf{m}_{\parallel} in terms of \mathbf{m}_0 , as follows:

$$\mathbf{m}_{\parallel} = \frac{\Delta \mathbf{m}_{10}}{\gamma}. \quad (\text{A.33})$$

where the length of the vector $\Delta \mathbf{m}_{10} = \mathbf{m}_0 - \mathbf{m}_1$ can be determined using the following geometric connection between any given input and output midpoints \mathbf{m}_1 and \mathbf{m}_2 , and azimuths θ_1 and θ_2

$$\left| \frac{\Delta m}{\sin \Delta \theta} \right| = \left| \frac{\Delta m_{10}}{\sin(\theta_2 - \Delta \varphi)} \right| = \left| \frac{\Delta m_{02}}{\sin(\theta_1 - \Delta \varphi)} \right|. \quad (\text{A.34})$$

To find the third component of the reflection point projection \mathbf{m}_{\perp} , we substitute expression (A.33) into (A.30). Choosing a convenient parameterization $\mathbf{s}_2 = \mathbf{m}_0 + \mathbf{h}_2^s$, $\mathbf{r}_2 = \mathbf{m}_0 + \mathbf{h}_2^r$, where $\mathbf{h}_2^r - \mathbf{h}_2^s = 2 \mathbf{h}_2$, and $\mathbf{h}_2^r + \mathbf{h}_2^s = 2 \Delta \mathbf{m}_{02} = 2 (\mathbf{m}_2 - \mathbf{m}_0)$, we can rewrite the two-point traveltime function from (A.30) in the form

$$t_2 = \frac{\sqrt{R^2 - \gamma(1-\gamma)m_{\parallel}^2 + (h_2^s)^2 - 2 \mathbf{h}_2^s \cdot (\mathbf{m}_{\perp} + (1-\gamma)\mathbf{m}_{\parallel})}}{v} + \frac{\sqrt{R^2 - \gamma(1-\gamma)m_{\parallel}^2 + (h_2^r)^2 - 2 \mathbf{h}_2^r \cdot (\mathbf{m}_{\perp} + (1-\gamma)\mathbf{m}_{\parallel})}}{v} \quad (\text{A.35})$$

Fermat's principle (A.31) leads to a simple linear equation for the length of \mathbf{m}_{\perp} , which has the explicit solution

$$m_{\perp} = (\gamma - 1)m_{\parallel} \cot(\theta_2 - \theta_1) - \frac{h_2 \left(R^2 - \gamma(1-\gamma)m_{\parallel}^2 \right)}{(h_2^2 - (\Delta m_{02})^2) \sin(\theta_2 - \theta_1)}, \quad (\text{A.36})$$

where m_{\parallel} is defined by (A.33), and Δm_{02} satisfies the relationship (A.34).

Because the reflection point is contained inside the ellipsoid, its projection obeys the evident inequality

$$z^2(\mathbf{m}) = R^2 - m_{\perp}^2 - (1 - \gamma)m_{\parallel}^2 \geq 0. \quad (\text{A.37})$$

It is inequality (A.37) that defines the aperture of the AMO operator. After transformation (2.5) and algebraic simplifications, it takes the form of inequality (2.10), which is convenient for an efficient implementation of AMO.

2D AMO OPERATOR

When the input offset h_1 is parallel to the output offset h_2 , the determinant of the system (A.11) is equal to zero. In this case, the 3D AMO operator degenerates to a 2D operator. The fact that the determinant of the system of equations is equal to zero means that the two equations are linearly dependent, and that we are left with only one equation. However, because the operator is two-dimensional, the number of components of the unknown \mathbf{k}_0 also reduces from two to one. Consequently, another stationary-phase approximation to the AMO integral need to be solved. The new equation is quartic and can be solved using Mathematica to get a solution for the kinematics of the operator. The resulting expression for the 2D AMO operator is presented in equation (2.3) of the main text.

Bibliography

- Bagaini, C., Spagnolini, U., and Paziienza, V., 1994, Velocity analysis and missing offset restoration by prestack continuation operators: 65th Ann. Internat. Meeting, Soc. Expl. Geophys., Expanded Abstracts, 1549–1552.
- Bale, R., and Jakubowicz, H., 1987, Post-stack prestack migration: Post-stack prestack migration: 57th Annual Internat. Mtg., Soc. Expl. Geophys., Expanded Abstracts, Session:S14.1.
- Beasley, C. J., and Klotz, R., 1992, Equalization of DMO for irregular spatial sampling: 62nd Annual Internat. Mtg., Soc. Expl. Geophys., Expanded Abstracts, 970–973.
- Beasley, C. J., and Mobley, E., 1988, Amplitude and antialiasing treatment in $(x - t)$ domain DMO: 58th Annual Internat. Mtg., Soc. Expl. Geophys., Expanded Abstracts, 1113–1116.
- Beasley, C. J., 1994, Acquisition geometry related amplitude artifacts: 64th Ann. Internat. Meeting, Proceedings of the SEG Post-convention Workshop, Prestack Amplitude Preservation.
- Beylkin, G., 1985, Imaging of Discontinuities in the Inverse Scattering Problem by Inversion of a Causal Generalized Radon Transform: J. Math. Phys., **26**, 99–108.
- Biondi, B., and Chemingui, N., 1994, Transformation of 3-D prestack data by Azimuth Move-out: 64th Ann. Internat. Meeting, Soc. Expl. Geophys., Expanded Abstracts, 1541–1544.
- Biondi, B., and Palacharla, G., 1996, 3-D prestack migration of common-azimuth data: Geophysics, Accepted for publication.

- Biondi, B., and Ronen, S., 1986, Shot profile dip moveout using log-stretch transform: Shot profile dip moveout using log-stretch transform:, 56th Annual Internat. Mtg., Soc. Expl. Geophys., Expanded Abstracts, Session:S7.3.
- Biondi, B., Fomel, S., and Chemingui, N., 1998, Azimuth moveout for 3-D prestack imaging: *Geophysics*, **63**, no. 2, 574–588.
- Black, J. L., and Schleicher, K., 1989, Effect of irregular sampling on prestack DMO: 59th Annual Internat. Mtg., Soc. Expl. Geophys., Expanded Abstracts, 1144.
- Black, J. L., Schleicher, K., and Zhang, L., 1993a, True-amplitude imaging and dip moveout: *Geophysics*, **58**, 47–66.
- Black, J. L., Schleicher, K., and Zhang, L., 1993b, True-amplitude imaging and dip moveout: *Geophysics*, **58**, 47–66.
- Bleistein, N., and Handelsman, R. A., 1975, *Asymptotic expansions of integrals*: Rinehart Winston.
- Bleistein, N., 1987, On the imaging of reflectors in the earth: *Geophysics*, **52**, no. 7, 931–942.
- Bleistein, N., 1990, Born dmo revisited: 60th Annual Internat. Mtg., Soc. Expl. Geophys., Expanded Abstracts, 1366–1369.
- Bolondi, G., Loinger, E., and Rocca, F., 1982, Offset continuation of seismic sections: *Geophys. Prosp.*, **30**, no. 6, 813–828.
- Bolondi, G., Loinger, E., and Rocca, F., 1984, Offset continuation in theory and practice: *Geophys. Prosp.*, **32**, no. 6, 1045–1073.
- Canning, A. J., and Gardner, G. H. F., 1995, Another look at the question of azimuth: *The Leading Edge*, submitted.
- Canning, A. J., and Gardner, G. H. F., 1996, A two-pass approximation to 3-D prestack migration: *Geophysics*, **61**, no. 2, 409–421.

- Chemingui, N., and Biondi, B., 1995, Amplitude-preserving azimuth moveout: Expanded Abstracts, 1453–1456.
- Claerbout, J., 1997, Preconditioning and scaling: SEP-**94**, 137–140.
- Claerbout, J., 1999, Geophysical estimation by example: Environmental soundings image enhancement: Stanford Exploration Project, <http://sepwww.stanford.edu/sep/prof/>.
- Cohen, J. K., and Hagin, F. G., 1985, Velocity inversion using a stratified reference: Geophysics, **50**, no. 11, 1689–1700.
- Deregowski, S. M., and Rocca, F., 1981, Geometrical optics and wave theory of constant offset sections in layered media: Geophys. Prosp., **29**, no. 3, 374–406.
- Fomel, S., and Biondi, B., 1995a, The time and space formulation of azimuth moveout: SEP-**84**, 25–38.
- Fomel, S., and Biondi, B. L., 1995b, Azimuth moveout: The operator parameterization and antialiasing: SEP-**89**, 89–108.
- Fomel, S. B., and Biondi, B. L., 1995c, The time and space formulation of azimuth moveout: The time and space formulation of azimuth moveout:, 65th Annual Internat. Mtg., Soc. Expl. Geophys., Expanded Abstracts, 1449–1452.
- Gardner, G. H. F., and Canning, A. J., 1994, Effects of irregular sampling on 3-D prestack migration: 64th Annual Internat. Mtg., Soc. Expl. Geophys., Expanded Abstracts, 1553–1556.
- Goldin, S. V., 1986, Seismic travelttime inversion: SEG, Tulsa.
- Goldin, S. V., 1994, Superposition and continuation of transformations used in seismic migration: Russian Geology and Geophysics, **35**, no. 9, 109–121.
- Hale, D., and Artley, C., 1993, Squeezing dip moveout for depth-variable velocity: Geophysics, **58**, 257–264.
- Hale, D., 1984, Dip-moveout by Fourier transform: Geophysics, **49**, no. 6, 741–757.

- Hubral, P., Schleicher, J., and Tygel, M., 1996, A unified approach to 3-d seismic reflection imaging, Part I: Basic concepts: *Geophysics*, **61**, no. 4, 742–758.
- Jaramillo, H. H., and Bleistein, N., 1997, Demigration and migration in isotropic inhomogeneous media: 67th Annual Internat. Mtg., Soc. Expl. Geophys., Expanded Abstracts, 1673–1676.
- Liner, C. L., and Cohen, J. K., 1988, An amplitude-preserving inverse of Hale's dmo: 58th Annual Internat. Mtg., Soc. Expl. Geophys., Expanded Abstracts, Session:S17.5.
- Liner, C. L., 1988, General Theory and Comparative Anatomy of Dip Moveout: Center for Wave Phenomena Research Report number CWP-073.
- Liner, C., 1990, General theory and comparative anatomy of dip moveout: *Geophysics*, **55**, no. 5, 595–607.
- Notfors, C. D., and Godfrey, R. J., 1987, Dip moveout in the frequency-wavenumber domain (short note): *Geophysics*, **52**, no. 12, 1718–1721.
- Ronen, S., and Goodway, W., 1998, Coverage and binning issues for marine seismic surveys: Coverage and binning issues for marine seismic surveys:, Soc. Expl. Geophys., The Leading Edge, 1600–1605.
- Ronen, J., and Liner, C., 1987, Theory of spatial antialiasing of log-stretched multichannel reflection data: 57th Annual Internat. Mtg., Soc. Expl. Geophys., Expanded Abstracts, Session:S14.5.
- Ronen, S., Nichols, D., Bale, R., and Ferber, R., 1995, Dealiasing DMO: Good-pass, bad-pass, and unconstrained: 65th Ann. Internat. Meeting, Soc. Expl. Geophys., Expanded Abstracts, 743–746.
- Ronen, J., 1985, Multichannel inversion in reflection seismology: Ph.D. thesis, Stanford University.
- Ronen, J., 1987, Wave-equation trace interpolation: *Geophysics*, **52**, no. 7, 973–984.

- Schleicher, J. M., T., and Hubral, P., 1993, 3-D true-amplitude finite-offset migration: *Geophysics*, **58**, no. 8, 1112–1126.
- Slawson, S. E., Monk, D. J., and Sudhakar, V., 1995, DMO implications for 3-D survey design: 65th Annual Internat. Mtg., Soc. Expl. Geophys., Expanded Abstracts, 935–938.
- Stovas, A. M., and Fomel, S. B., 1996, Kinematically equivalent integral DMO operators: *Russian Geology and Geophysics*, **37**, no. 2.
- Sullivan, M. F., and Cohen, J. K., 1987, Prestack Kirchhoff inversion of common-offset data: *Geophysics*, **52**, no. 6, 745–754.
- Zhang, L., 1988, A new Jacobian for dip moveout: *SEP*–**59**, 201–208.